國立交通大學

機械工程學系

博士論文

火焰在有限長度PMMA燃料及伴隨熱輻射效應下傳播情形之數值模擬研究

Numerical Study For Downward Flame Spread Over A Finite-Length PMMA With Radiation Effect

研　究　生：張文奎

指導教授：陳俊勳　教授

中華民國九十六年六月

火焰在有限長度 PMMA 燃料及伴隨熱輻射效應下傳播情形之數值模擬研究

Numerical Study For Downward Flame Spread Over A Finite-Length PMMA With Radiation Effect

研究生：張文奎　　Student：Wen-Kuei Chang
指導教授：陳俊勳教授　　Advisor：Prof. Chiun-Hsun Chen

國立交通大學
機械工程學系
博士論文

A Dissertation
Submitted to Department of Mechanical Engineering
College of Engineering
National Chiao Tung University
in Partial Fulfillment of the Requirements
for the Degree of
Doctor of Philosophy
in Mechanical Engineering
July 2006
Hsinchu, Taiwan, Republic of China

中華民國九十六年六月

火焰在有限長度 PMMA 燃料及伴隨熱輻射效應下傳播情形之數值模擬研究

學生：張文奎　　　　　　　　　　指導教授：陳俊勳

國立交通大學機械工程研究所

摘要

本論文係以暫態燃燒模式來模擬在風洞中逆向傳播火焰在有限長度PMMA燃料及考慮熱輻射效應時，火焰由引燃至穩定燃燒傳播的一連續過程。論文內容可分為三部分。在第一部分中主要的研究參數包括逆向進氣速度、逆向進氣溫度以及燃料厚度等。模擬結果則是主要包括火焰引燃時間以及火焰傳播速率。在不同參數的改變之下對於火焰引燃時間及火焰傳播速率的影響將在本部分中詳細分析與討論。另外本研究各項所得的模擬結果也會與相關的實驗數據（潘英杰，1999）以及數值模擬（吳國光等人，2003）互相比較，經由比較的結果發現本研究的模擬結果會比先前吳國光等人所模擬的結果更接近實驗所量測的數據，其原因是在本研究當中多加考慮了幾項因素包括密閉空間效應、有限長度的燃料以及氣相和固相的熱輻射等。

第二部分主要是研究逆向進氣速度對於火焰傳播行為的影響。在此部分中所模擬的逆向進氣速度範圍為0~100公分/秒，而在先前的研究包括潘英杰(1999)，吳國光等人(2003)以及本論文第一部分所模擬的逆向進氣速度範圍則是 40~100 公分/秒。由氣相與固態燃料溫度、固態燃料預熱長度以及熱通量等模擬結果來探討火焰引燃及傳播等行為。由模擬結果得知火焰

引燃時間隨著逆向進氣速度的增加而增加。但是火焰傳播速率可由逆向進氣速度分為兩個區域。首先火焰傳播速率隨逆向進氣速度增加，當逆向進氣速度到達 32 公分/秒時，火焰傳播速率達到最大值，接著隨著逆向進氣速度的增加而減小。當逆向進氣速度小於 32 公分/秒時，火焰主要是受氧氣傳輸效應的影響。當逆向進氣速度大於 32 公分/秒時，火焰主要則是受拉伸效應的影響。除此之外，本研究顯示熱輻射效應增加火焰引燃時間並且減小火焰強度與傳播速率。逆向進氣溫度與固態燃料溫度對於火焰傳播行為的影響也在本部分中被探討，另外模擬結果顯示當逆向進氣速度增加時，則逆向進氣速度效應將會大於逆向進氣溫度效應。

第三部分主要是利用三維燃燒模式來探討在風洞中逆向傳播火焰在有限長度 PMMA 燃料上傳播之情形。此部分主要是探討三維效應對於火焰傳播的影響。逆向進氣速度為主要之模擬參數。火焰由引燃至傳播的過程將會在此部分中詳細討論。火焰引燃時間會隨著逆向進氣速度的增加而增加，但在三維模擬中火焰引燃時間大於二維模擬所得結果而且隨著逆向進氣速度的增加，二維與三維之間火焰引燃時間的差異會變小。由模擬結果顯示火焰傳播速率隨著逆向進氣速度的增加而減少而由火焰傳至風洞壁面的熱損失則會使火焰強度變弱。而本模擬結果與相關實驗如潘英杰(1999)與數值模擬如吳國光等人(2003)與本論文第一部分的結果做比較。其比較結果發現在較低的逆向進氣速度之下，本模擬結果會與實驗所得之數據更為接近。

Numerical Study For Downward Flame Spread Over A Finite-Length PMMA With Radiation Effect

Student : Wen-Kuei Chang Advisor : Chiun-Hsun Chen

Department of Mechanical Engineering

National Chiao Tung University

Abstract

This study utilizes an unsteady combustion model to investigate the ignition delay and subsequent downward flame spread over a finite-length PMMA slab under an opposed flow with the effect of radiation included in a two-dimensional wind tunnel. This study consists of three parts. In the first part, the variable parameters studied are the opposed flow temperature and velocity and the solid fuel thickness, respectively. The major simulated results include the ignition delay time and the flame spread rate. The influences of the variable parameters on the ignition delay time and the flame spread rate are discussed in detail in this section. Additionally, the predictions of the present model are compared with the corresponding experimental measurement of Pan (1999) and the simulation of Wu et al. (2003). The comparison shows that the simulated results of the present model are more similar to the experimental values because the several factors, such as enclosure, finite-length fuel plate and both gas and solid phase radiations are considered in the present combustion model.

In the second part, the opposed flow velocity is used as a parameter to study the flame spread behavior. The opposed flow velocities simulated herein are

varied from 0 to 100cm/s, whereas the ones used by Pan (1999), Wu et al. (2003) and the first part of present dissertation are varied from 40 to 100cm/s. The gas and solid phase temperatures, preheat length and heat flux are considered in order to examine the flame ignition and spread characteristics. The numerical results reveal that the ignition delay time increases with the opposed flow velocity. However, the flame spread rate varies with the opposed flow velocity in a non-monotonic manner that can be identified as two distinct regimes with a peak value in between. The flame spread rate reaches a maximum at $\bar{u}_\infty = 32cm/s$, and then falls, regardless of whether the flow velocity is increasing or decreasing. For $\bar{u}_\infty < 32cm/s$, the flame behaviors are dominated by oxygen transport. For $\bar{u}_\infty > 32cm/s$, the flame stretch effect controls the flame behavior. Additionally, this work demonstrates that the effect of radiation delays the flame ignition and reduces both the flame strength and the corresponding spread rate. The effects of the opposed flow temperature and thickness of the solid fuel are also investigated. The predicted results indicate that a higher opposed flow temperature or a thinner solid fuel facilitates the ignition and accelerates flame spread. The effect of opposed flow velocity eventually overcomes that of opposed flow temperature as the flow speed is further increased.

In the third part, the three-dimensional unsteady combustion model is utilized to investigate the downward flame spread over a finite-length PMMA slab under an opposed flow in the wind tunnel. The aim of this section is to examine the 3D effect on the flame spread over the solid fuel surface. The opposed flow velocity is used as parameter and the ambient oxygen concentration is at 0.233. The entire process from ignition to subsequent flame spread over the solid fuel surface is demonstrated in detail. The ignition delay time increases with an increase of opposed flow velocity. However, the ignition delay times of 3D problem are greater than ones of 2D problem and the discrepancies of ignition

delay time between the 2D and 3D problems are decrease with an increase of opposed flow velocity. The simulated results indicate that the flame spread rate decreases with an increase of opposed flow velocity and the flame intensity becomes weaker due to the heat loss from the flame to the lateral walls of wind tunnel. Additionally, the simulated results of the present model are compared with the corresponding experimental measurement of Pan (1999) and the predictions of Wu et al. (2003) and the first part of present dissertation. The comparison shows that the simulated flame spread rates of the present model are similar to the experimental values, especially in the lower speed flow regime.

誌謝

感謝恩師陳俊勳教授悉心教導

感謝我須要感謝的每一個人

謝謝你們

將本論文獻給我最敬愛的母親與在天堂的父親

Contents

List of tables

List of figures

Nomenclature

$\overline{a}$	Absorption coefficient, 1/cm
$\overline{A}$	Pre-exponential factor for fuel pyrolysis, 1/s
$\overline{B}$	Pre-exponential factor for gas phase reaction, cm^3/mols
$\overline{E}$	Activation energy, J/mol
C	The specific heat ratio of the gas mixture to solid fuel, $\overline{C}_p / \overline{C}_s$
$\overline{C}_p$	Specific heat for gas mixture, J/gK
$\overline{C}_s$	Specific heat for solid fuel, J/gK
$\overline{D}$	Specific diffusivity, cm^2/s
Da	Damköhler number, $\overline{B}\,\overline{\rho^*}\,\overline{\delta}/\overline{V_r}$
E	Non-dimensional activation energy, $\overline{E}/\overline{R}\,\overline{T_\infty}$
f	Stoichiometric oxidizer/fuel mass ratio
g	Non-dimensional gravitational acceleration, $\overline{g}/\overline{g_e}$
$\overline{g}_e$	Earth normal gravity, cm/s^2
Gr	Grashof number, $\overline{g}(\overline{\rho_\infty}-\overline{\rho_f})\overline{\delta}^3 / \overline{\rho^*}\,\overline{\nu^*}^2$
I_0	Zeroth moment of intensity
$\overline{k}$	Conductivity, W/cmK
L	Non-dimensional latent heat, $\overline{L}/\overline{C_s}\,\overline{T_\infty}$
$\overline{L}$	Latent heat, J/g
Le	Lewis number, $\overline{\alpha}/\overline{D}$
m''_s	Non-dimensional mass flux, $\overline{m''_s}\,\overline{\alpha^*}/\overline{\rho_{s\infty}}\,\overline{V_r}^2\,\overline{\tau}$
N_∞	Conduction-radiation parameter based on $\overline{T_\infty}$, $\overline{k^*}\,\overline{V_r}/\overline{\sigma}\,\overline{T_\infty}^3\,\overline{\alpha^*}$
P	Non-dimensional pressure, $(\overline{P}-\overline{P_\infty}) / \overline{\rho^*}\,\overline{V_r}^2$

Pr	Prandtl number, $\bar{\nu}/\bar{\alpha}$
$\bar{q}$	Heat of combustion per unit mass of fuel, J/g
$\bar{q}_c$	Conductive heat flux, W/cm^2
$\bar{q}_{ex}$	External heat flux, W/cm^2
$\bar{q}_{gr}$	Gas phase radiation heat flux, W/cm^2
$\bar{q}_{sr}$	Solid phase radiation heat flux, W/cm^2
$\bar{q}_{net}$	Net heat flux, W/cm^2
R	Non-dimensional density
$R\mathrm{e}$	Reynolds number, $\overline{\rho^*}\,\overline{\alpha^*}\big/\overline{\mu^*}$
$\bar{t}$	Time, s
$\bar{T}$	Gas phase temperature, K
$\bar{T}_s$	Solid phase temperature, K
$\bar{T}_i$	Incoming flow temperature, K
$\bar{u}$	Velocity parallel to the fuel surface, cm/s
$\bar{u}_\infty$	Opposed flow velocity, cm/s
$\bar{v}$	Velocity normal to the fuel surface, cm/s
$\overline{V_f}$	Flame spread rate, cm/s
$\overline{V_r}$	Reference velocity, cm/s
$\bar{x}$	Coordinate parallel to the fuel surface, cm
$\bar{y}$	Coordinate normal to the fuel surface, cm
Y_F	Fuel mass fraction
Y_O	Oxygen mass fraction

Greek Symbols

$\bar{\alpha}$	Thermal diffusivity, cm^2/s

γ	Temperature ratio, $\overline{T^*}/\overline{T_\infty}$
$\overline{\delta}$	Reference length, cm
$\overline{\rho}$	Density of gas phase, g/cm^3
$\overline{\rho}_s$	Density of solid fuel, g/cm^3
$\overline{\tau}$	Solid fuel thickness, cm
$\overline{\sigma}$	Stefan-Boltzmann constant, J/K^{4}cm^{2}s
λ	Wavelength, μm
ε	Surface emissivity
μ	Non-dimensional dynamic viscosity, $\overline{\mu}/\overline{\mu^*}$
$\overline{\nu}$	Kinematic viscosity, cm^2/s
$\dot{\omega}_F$	Non-dimensional gas phase reaction rate

Overhead

$-$	Dimensional quantities

Superscript

*	Reference state
"	Flux

Subscript

ex	External
i	Incoming flow
max	Maximum
min	Minimum
o	Oxizider
s	Solid phase
∞	Ambient condition

Chapter 1

Introduction

1.1 Background

This work investigates flame ignition and the characteristics of the subsequent flame spread over a finite-length PMMA slab in an opposed convection environment in a wind tunnel, using an unsteady combustion model that incorporates both gas and solid phase radiations. The corresponding experimental test channel is 70 cm long with a rectangular cross section of 10*10 cm^2. The specimens are mounted on the groove of the test section and the sides of the groove are covered with asbestos plates. Thermocouples and a laser holographic interferometer are used to measure the temperatures of the solid fuel surface and the gas, respectively. This study is motivated by an earlier study of Wu et al. (2003), which only considered the ignition and the subsequent flame spread over a fuel plate of infinite-length in an open atmosphere without both gas and solid phase radiations. In that investigation, the differences between the predicted flame spread rates and the corresponding experimental measurements were attributed to the effects such as the enclosure, the fuel length, the gas and solid phase radiations and the 3D effect. Hence, this work makes an intensive modification according to the aspects mentioned above. The serial parameters studies are performed to investigate the influences of these effects on ignition and flame spread behavior and attempt to mitigate the discrepancies between results of the numerical predictions and the experimental measurements.

1.2 Literature survey

Pan (1999) and Chen (1999) investigated the steady flame spread characteristics over PMMA in an opposed forced convection environment in a wind tunnel. The variable parameters were the velocity and the temperature of the opposed flow and the thickness of solid fuel. They found that the flame spread rate increases with an increase flow temperature, a drop in the flow velocity or the fuel thickness. Their image results further showed that the thermal boundary layer becomes thicker as the opposed flow temperature increases at a fixed flow velocity or the opposed flow velocity declines at a constant flow temperature. Wu et al. (2003) developed an unsteady combustion model with mixed convection to explore the flame spread behaviors of a thick PMMA slab of infinite length in an environment with opposed flow. The simulated flame spread rates were compared with the measurements made by Pan (1999). The results were highly consistent except in the low-speed flow regime. The discrepancies can be attributed to the radiation, fuel size and the three dimensional effect are not under the consideration in the model. Fujita et al. (2000) experimentally studied the radiative ignition on paper sheet in microgravity. The results showed that the gas phase temperature becomes higher than that of the solid surface before ignition, and the main mechanism of radiative solid ignition here is due to the gas phase reaction. Furthermore, the ignition delay time strongly depends on the oxygen concentration and ambient pressure. It decreases with a higher oxygen concentration or ambient pressure. Fujita et al. (2002) experimentally investigated the effect of external flow on flame spread over polyethylene wires in microgravity. The results revealed that the flame spread rate is controlled mainly by preheat length, standoff distance and flame temperature. The flame spread phenomenon can be divided into three regimes based on flow velocity. These are an oxygen transport control regime, a geometrical effect regime and a chemical-kinetics controlled regime.

Wichman (1983) developed a theoretical model to estimate the rate of flame spread under conditions of heat transfer control with account taken of the fact that the gas velocity was not uniform. The results indicated that the functional dependence of the spread rate on the external gas velocity is modified from the one obtained in the classical study of DeRis (1968). Thereafter, Wichman (1992) explained two mechanisms for the extinguishment of spreading flames. In the first, the particle residence time in the reaction zone is reduced by the increased flow velocity, giving a blow off extinction. In the second, flow velocity decreases toward flame spread rate and extinction again occurs eventually. Takahashi et al. (2002) analytically and experimentally studied flame spread over a thin PMMA sheet in microgravity. They concluded that reducing the relative flow velocity enlarges the size of preheat zone, increasing radiant loss, and that radiant heat loss reduces the flame spread rate and may also cause extinction. Olson et al. (2001) experimentally investigated the radiative ignition and subsequent three dimensional flame spread over thin cellulose fuels. They found that gas phase residence time over the heated spot is a critical parameter in ignition delay. After ignition, the flame in a fan shaped pattern spreads from the central ignition spot and is toward upstream. The flame spread angle increases with increasing external air flow and oxygen concentration. They also found that due to the oxygen shadow effect, the upstream and downstream flame spread over the fuel plate is not observed simultaneously. The downstream flame only starts to spread after upstream flame spread is complete and extinguished. Ito et al. (2005) experimentally investigated the propagation and extinction mechanisms of opposed-flow flame spread along a thick slab of PMMA. They showed that as the opposed-flow rate increases or the ambient oxygen concentration decreases, the Damkohler number decreases. When the Da falls below a critical value, extinction or no flame spreading may occur. The radiative heat loss has very little effect on the extinction because it is small compared with the other heat transfer rates. The results also demonstrated that the steady flame spread rate is proportional to the net total heat transfer rate to the preheat zone. However, no matter what the enough heat feedback to the preheat zone or not, the flame spread rate decreases rapidly when nearing the extinction limit.

West et al. (1994) studied the surface radiation effects on flame spread over thermally thick fuels in an opposed flow. They concluded that the fuel surface radiation is important for thermally thick fuel at all flow levels, however, and it is important for thermally thin fuel only at low velocity level. Bhattacharjee and Altenkirch (1991) developed a numerical model to study the effect of surface radiation on flame spread in a quiescent microgravity environment by using the oxygen concentration and solid surface emittance as parameters. They found that the flame spread rate and temperature decrease as solid surface emittance increases in any oxygen level, and the flame shrinks in size while moving closer to the surface. In the other hand, the rate of decrease in flame spread rate being more severe at higher values of solid surface emittance and lower oxygen levels. Bhattachariee et al. (2000) experimentally, computationally, and analytically investigated the downward flame spread over a polymethylmethacrylate plate in an oxygen/nitrogen environment at normal gravity. They presented that the flame spread rates in the thermal regime as the fuel thickness was changed from the thin- to the thick-limit. A simple formula for the transition thickness between the thin and thick fuel regimes was proposed, and it seemed to agree well with experimental measurements. From the computational results, they also concluded that the radiative effects seem not to influence the flame spread rate except at very high ambient pressures. Rhatigan et al. (1998) examined the effects of gas phase radiation on the burning and extinction of a solid fuel. They plotted the heat fluxes, flame temperature and burning rate as functions of the flow stretch rate. The computed results demonstrated that the gas phase radiative effects are stronger at lower stretch rates. Fernandez-Pello and Hirano (1982) experimentally studied the controlling mechanism of flame spread over the surface of combustible solids. The heat transfer and gas phase chemical kinetic aspects of the flame spread process were addressed respectively for the flame spread in oxidizing flow. They indicated that chemical kinetics of gas phase plays a critical role and it must be considered when flame spread in opposed gas flow occurs at near extinction or non-propagating conditions. Son and Ronney (2002) experimentally studied flame spread over thermally thick fuels. They found that the radiative preheating and reabsorption effect are less important in normal gravity, because a substantial flow velocity is caused by buoyancy, reducing the thickness of the flame and thereby reducing the volume of radiating gas. Takahashi et al. (2000) and Ayani et al. (2006) examined flame spread rates over PMMA sheets in normal gravity and in microgravity. They found that the flame spread rate over a thermally thin fuel is inversely proportional to the thickness of the fuel, whereas that over a thermally thick fuel is proportional to the opposed flow velocity, in complete agreement with analyzed research by DiRis (1969). Other investigations, such as Wichman and Williams (1983a), Wichman and Williams (1983b) and Delichatsios (1986), have developed formulas that show identical proportionalities. Tizon et al. (1999) analyzed the wind-aided flame spread process along a solid fuel rod under oblique forced flow. Their results indicated that the effects of gas-phase chemical kinetics were important for large strain rates and the spread rate depended strongly on the strain rate. They also found that the effects of radiation from the gas phase are negligible because the heat transfer by convection typically dominates at large Reynolds numbers of the transverse velocity. Zhu and Gore (2005) studied the opposed-flow laminar methane/air diffusion flames by the numerical simulations. They indicated that the peak flame temperature and the soot volume fraction increase with increasing pressure or decreasing injection velocity for all radiation conditions. The soot and gas radiation effects are stronger at the higher pressures or lower velocities. The simulated results also showed that the peak soot volume fraction and soot emission index decrease by 85 and 97% with an increase in injection velocity from 10 to 100 and 200 cm/s, separately.

Kumar et al. (2003a) used a two dimensional flame spread model with flame radiation to compare the extinction limits and spreading rates in opposed and concurrent spreading flames over thin solids. The varying parameters were oxygen percentage, free stream velocity, and flow entrance length. Numerical results showed that at low free stream velocities with shorter entrance length, the flame spread rates are higher and have a lower oxygen extinction limit, whereas in high free stream velocities, the flame spread rates are lower and have a higher oxygen extinction limit. The flame spread rate in opposed flow varies with free stream velocity in a non-monotonic manner, with a peak rate at an intermediate free stream velocity. The flame spread rate in concurrent flow increases linearly with free stream velocity. Kumar et al. (2003b) also presented a numerical study on flame-surface radiation interaction in flame spread over thin solid fuels in quiescent microgravity and in normal gravity environments. It was observed that the flame in microgravity is very sensitive to the surface radiation properties. The fuel with high solid absorptivity can absorb substantial flame radiation and flame spreads faster than the corresponding adiabatic case irrespective of value of solid emissivity. Lin and Chen (1999) investigated how the gas-phase radiation, whose model included both the cross-stream and stream-wise gas phase radiation coupled with solid phase one, affected the spreading flame. By comparing the results with the predicted ones of Chen and Cheng (1994), which only considered the radiation effect in cross-stream direction. They concluded that the stream-wise radiation contributes to reinforce the forward heat transfer rate subsequently increasing the flame spread rate.

Di Blasi (1995a) examined, by numerical simulation, the effects of the thickness on the concurrent spread of flames over thin and thick fuels under forced convection. Three main flame spread regimes were identified. In the kinetic region, the flame spread rate increases with the solid fuel thickness below 0.008 cm. In the thermally thin region, the flame spread rate falls as the solid fuel thickness increases in the range from 0.008 cm to 0.5 cm. Finally, in the thermally thick region, the flame spread rate becomes almost constant when the solid fuel thickness exceeds 0.5 cm. Di Blasi (1995b) also investigated the opposed flame spread over cellulosic fuels in a microgravity environment, using the forced gas flow and the solid thickness as the varied parameters. For very thin fuels, flame spread rate increases with the solid thickness and the solid radiative heat loss controls the flame spread rate. As the fuel thickness becomes thicker, the flame spread rate decreases with the solid thickness and the flame radiative heat transfer playas role of increasing importance. For the thick fuels, flame radiation is reduced whereas surface radiative heat loss is again at a high level. Suzuki et al. (1994) studied the downward flame spread over paper sheets of thickness between 0.4 and 10mm to investigate the mechanisms by which flames spread. They identified four flame spreading behaviors under the conditions in the four regions. The flame spread is stable at the limiting thickness of the paper sheets. They also derived an energy equation for the heat flux through the pyrolytic region and the solid surface in front of the leading edge.

Nakabe et al. (1994) investigated the ignition and transition to flame spread over a thermally thin fuel in a microgravity environment. A comparison was made between the axis-symmetric configuration and a two-dimensional configuration. The results indicated that ignition is earlier in two-dimensional configuration and the difference between the two configurations is roughly 25% in the same boundary conditions. Jiang and Fan (1995) made the predictions of flame spread in slow forced flow under gravitational acceleration normal to the fuel surface and flame spread in a quiescent environment in an enclosed chamber under gravitational acceleration parallel to the fuel surface. The results indicated that the effect of oxygen transport on flame spread is greater than that of heat transfer in a microgravity environment. In addition, the microgravity level has a significant effect on the flame spread over a vertical wall in an enclosed chamber under gravitational acceleration parallel to the fuel surface. Mell and Kashiwagi (2000) numerically studied the effects of finite sample width on transition and flame spread in microgravity. They found that the finite width effects are insignificant when the ambient wind is relatively large and the influence of thermal expansion on the net incoming oxygen supply decreased as the ambient wind speed increased. Thus, the flame spread behavior of the three-dimensional flame tended to that of the two-dimensional flame with increasing ambient wind speed.

Nakamura et al. (2002) numerically studied the enclosure effect on the spread of the flame over solid fuel under microgravity. Because the confinement of the flow field and the thermal expansion initiated by heat and mass addition in the chamber, the flame spread rate for the case with enclosure is faster than the one without any enclosure. The predictions also showed that the enclosure effect is stronger at lower flow velocity.

Shih and T'ien (1997) theoretically studied the concurrent flow flame spread over a thin solid in a low speed flow tunnel. They found that the flow is accelerated in the downstream as the tunnel height is decreased. The flame is pressed to the solid fuel and the heat conduction rate to the solid; the flame length and the spread rate are also increased. However, the conductive heat loss to the wall becomes great which reversed the trend and decreases the flame length as the tunnel height becomes too small. Shih and T'ien (2000) numerically investigated the concurrent spread of flames over a thin solid in a low-speed flow tunnel in microgravity. The simulated results demonstrated two distinctive flame behaviors. With a high oxygen content or fast flow, the flame was long and far from the quenching limit. With a low oxygen content or slow speed, the flame was short and in the region near the quenching limit. They also found that the three dimensional effect on flame spreading was stronger in the low-speed flow regime. Shih and T'ien (2003) numerically studied the concurrent flame spread over a thin solid in a low-speed flow tunnel in microgravity by using three-dimensional combustion model. Several 3D effects due to the presence of the tunnel walls are examined. The walls change the velocity profiles and accelerate the flow in a direction parallel to the fuel. The cold walls conduct heat away from the flame, which produces heat loss and a quenched layer. Moreover, the oxygen side diffusion enhances the combustion reaction at the base region and pushes the flame base closer to the solid surface, increasing the flame spread rate. They also concluded that 3D effects are dominated by the heat loss to the side walls in the downstream portion of the flame and the flame spread rate increases with fuel width in higher speed flows.

1.3 Scope of the present study

The structure of this study is illustrated in the Figure 1.1. This work investigates the flame ignition and subsequent flame spread characteristics over a finite-length PMMA slab under mixed convection conditions using an unsteady combustion model that incorporates both gas and solid phase radiations in a wind tunnel. This study consists of three topics. The first topic modifies several aspects of the original combustion model of Wu et al. (2003), such as the enclosure, the finite-length fuel plate and the gas and solid phase radiations. The varying parameters, such as opposed flow velocity and temperature and the solid fuel thickness, are in the same ranges as those used in the Pan's experiment (1999). The entire process, from ignition to subsequent flame spread, is examined in detail. Additionally, the influences of the opposed velocity and temperature, the solid fuel thickness and length and the gas and solid phase radiations on the flame spread behavior are studied as well. The simulated results are compared with the corresponding experimental measurement of Pan (1999) and the prediction of Wu et al. (2003).

The second topic studies the flame spread in the lower flow velocity regime to investigate the influence of radiation on the flame spread behavior. The aforementioned series of studies, such as those of Pan (1999), Wu et al. (2003) and the part 1 of present dissertation, concluded that the influence of opposed flow velocity on the flame spread behavior exceeds that of opposed flow temperature as flow velocity is increased further, and that the discrepancies between the predicted and measured results, especially in the low flow speed regime are due to the radiation effect. Moreover, numerous investigations, such as those of West et al. (1994), Rhatigan et al. (1998), Tizon et al. (1999) and Zhu and Gore (2005), demonstrated that the radiation effect becomes stronger as the flow speed declines. Therefore, this work systematically investigates the effect of opposed flow velocity on the flame spread characteristics considering the radiation effect over a finite-length PMMA slab in a two-dimensional wind tunnel. The opposed flow velocities simulated herein are varied from 0 to 100cm/s, whereas the ones used by Pan (1999), Wu et al. (2003) and the part 1 of present dissertation are varied from 40 to 100cm/s. The effects of opposed flow temperature, solid fuel thickness and radiation heat loss at various flow velocities are also discussed.

In the third topic, the three-dimensional unsteady combustion model is basically developed from the original two-dimensional one of part 1 of present work to investigate the influences of 3D effect on the flame spread behavior over a finite-length PMMA slab. The earlier investigations demonstrated that the effect of opposed flow velocity on the flame spread behavior is greater than one of opposed flow temperature. Furthermore, numerous studies, such as those of Mell and Kashiwagi (2000), Nakamura et al. (2002) and Shih and T'ien (2003), indicated that the 3D effect is dominated by the flow velocity. Therefore, the parametric study in this part utilizes the opposed flow velocity as parameter to investigate the influence of 3D effect on ignition and subsequence flame spread behavior. The opposed flow temperature and the solid fuel thickness are fixed at 313K and 0.82cm, respectively. The entire process from ignition to subsequent flame spread is examined in detail and the simulated results are also compared with the corresponding experimental data of Pan (1999) and the predictions of Wu et al. (2003) and the part 1 of present dissertation. Finally, possible extensions of this work are suggested.

The writing sequence of present dissertation is: the mathematical model as well as the corresponding governing equations, initial and boundary conditions and solution methodology are presented in the chapter 2. A detailed discussion in simulated results is given in the chapter 3. Finally the conclusions are presented in the chapter 4.

Chapter 2

Mathematical model

2.1 Description

Figure 2.1 presents the physical configuration of two-dimensional ignition over a vertically oriented PMMA slab in a mixed convective environment. The test section of the wind tunnel is 70 cm long and 10 cm high. The solid fuel plates used in the simulation are 30 cm long and 0.82 cm and 1.74 cm thick. The solid fuel is assumed to be homogeneous, meaning that its composition is uniform. At $t<0$, a steady flow in the wind tunnel builds up over the entire test section. In the channel flow the surface velocity gradient is given by $a=4V_g/H$, where V_g is the centerline flow velocity and H is the height of the wind tunnel. At $t\geq 0$, an external heat flux with a Gaussian distribution with a width of 0.5 cm and a peak value of 5 W/cm^2, is imposed on the solid fuel surface and centered at x=0, where the top end of the solid fuel is connected to an adiabatic plate. Restated, only half of the incident radiation energy is used to heat the PMMA fuel. The solid fuel absorbs the external heat flux to raise its temperature gradually. Then, the solid fuel begins to pyrolyze and generate fuel vapors, which mix with air to form the flammable mixture adjacent to the surface of the fuel. Ignition occurs when the gas phase temperature is high enough to promote the chemical reaction. Subsequently, the flame begins to propagate, eventually reaching a steady rate of flame spread.

2.2 Governing equations in dimensional form

The unsteady combustion model and radiation model are basically modified from those developed by Lin and Chen (2000) and Wu and Chen (2004). However, Wu and Chen (2004) applied the P1 radiation model, in which the semi-gray scheme is adopted to define the effective absorption coefficient. Since the gas phase radiative properties depend strongly on the temperature and mixture concentrations, the simple assumptions used in these prior simulations are unrealistic and unsuitable for determining the radiative properties. Therefore, this work modifies the model of Wu and Chen (2004) by using the narrow band model instead of the P1 model to calculate the gas phase absorption coefficient and the radiation intensity. In this problem, the mathematical model consists of both gas and solid phase equations, which are coupled at the interface. This study makes the following assumptions for gas and solid phase.

In the gas phase, the following assumptions are made.

1. The flow field is two-dimensional.
2. The average molecular weight is constant.
3. The mixture is assumed to be an ideal gas with a constant and equal specific heat, equal binary diffusion coefficient, constant Prandtl and Lewis numbers and a constant value of $\bar{\rho}\bar{\mu}$.
4. Viscous dissipation and compressive work are neglected.
5. The Soret and Duffour effects as well as the pressure gradient diffusion are neglected.
6. The gas phase chemistry is described using a one-step overall chemical reaction.
7. The reaction rate is described by a second-order Arrhenius law kinetics.

In the solid phase, the assumptions are made.

1. The solid fuel is assumed to be homogeneous that its compositions are uniform.
2. The specific heat and thermal conductivity are assumed constant.

3. An Arrhenius-typed pyrolysis law is used to describe the fuel gasification.
4. The solid thickness is remained constant by assuming the flame spreads relatively fast enough that the fuel surface near the flame base remains approximately flat.
5. A burnout is defined when the solid fuel density becomes 7 percent of its virginal value and the char is removed simultaneously.

The assumptions regarding radiation in gas and solid phases are as follows:

1. Gas phase radiation is 2D. The narrow band model is employed to determine the radiation heat flux.
2. The gas is optically thin and the scattering effect is neglected because the production of soot is not considered in the gas phase chemical reaction.
3. The participating media are CO_2 and H_2O.
4. Soot radiation and surface reflectivity are neglected.
5. The fuel surface is opaque and diffuse.

The gas and solid phases governing equations in dimensional form are listed as follows:

Gas phase governing equations:

Continuity equation:

$$\frac{\partial \bar{\rho}}{\partial \bar{t}} + \frac{\partial (\bar{\rho}\bar{u})}{\partial \bar{x}} + \frac{\partial (\bar{\rho}\bar{v})}{\partial \bar{y}} = 0 \tag{2.1}$$

X-momentum equation:

$$\begin{aligned} &\bar{\rho}\frac{\partial \bar{u}}{\partial \bar{t}} + \bar{\rho}\bar{u}\frac{\partial \bar{u}}{\partial \bar{x}} + \bar{\rho}\bar{v}\frac{\partial \bar{u}}{\partial \bar{y}} = -\frac{\partial \bar{P}}{\partial \bar{x}} + \frac{\partial}{\partial \bar{x}}\left[2\bar{\mu}\frac{\partial \bar{u}}{\partial \bar{x}} - \frac{2\bar{\mu}}{3}\left[\frac{\partial \bar{u}}{\partial \bar{x}} + \frac{\partial \bar{v}}{\partial \bar{y}}\right]\right] + \\ &\frac{\partial}{\partial \bar{y}}\left[\bar{\mu}\left[\frac{\partial \bar{u}}{\partial \bar{y}} + \frac{\partial \bar{v}}{\partial \bar{x}}\right]\right] + \bar{g}\left(\bar{\rho}_\infty - \bar{\rho}\right) \end{aligned} \tag{2.2}$$

Y-momentum equation:

$$\bar\rho \frac{\partial \bar v}{\partial \bar t} + \overline{\rho u}\frac{\partial \bar v}{\partial \bar x} + \overline{\rho v}\frac{\partial \bar v}{\partial \bar y} = -\frac{\partial \bar P}{\partial \bar y} + \frac{\partial}{\partial \bar y}\left[2\bar\mu \frac{\partial \bar v}{\partial \bar y} - \frac{2\bar\mu}{3}\left[\frac{\partial \bar u}{\partial \bar x}+\frac{\partial \bar v}{\partial \bar y}\right]\right] + \frac{\partial}{\partial \bar x}\left[\bar\mu\left[\frac{\partial \bar u}{\partial \bar y}+\frac{\partial \bar v}{\partial \bar x}\right]\right] \qquad (2.3)$$

Energy equation:

$$\overline{\rho C_p}\frac{\partial \bar T}{\partial \bar t} + \overline{\rho C_p u}\frac{\partial \bar T}{\partial \bar x} + \overline{\rho C_p v}\frac{\partial \bar T}{\partial \bar y} = \frac{\partial}{\partial \bar x}\left[\bar k\frac{\partial \bar T}{\partial \bar x}\right] + \frac{\partial}{\partial \bar y}\left[\bar k\frac{\partial \bar T}{\partial \bar y}\right] - \overline{q\dot\omega_F} - \nabla\cdot\bar q^r \qquad (2.4)$$

where $\nabla\cdot\bar q^r = \frac{\partial \bar q_x^r}{\partial \bar x}+\frac{\partial \bar q_y^r}{\partial \bar y}$ is the gas phase radiation term.

Fuel species equation:

$$\bar\rho\frac{\partial Y_F}{\partial \bar t}+\overline{\rho u}\frac{\partial Y_F}{\partial \bar x}+\overline{\rho v}\frac{\partial Y_F}{\partial \bar y}=\frac{\partial}{\partial \bar x}\left[\overline{\rho D}\frac{\partial Y_F}{\partial \bar x}\right]+\frac{\partial}{\partial \bar y}\left[\overline{\rho D}\frac{\partial Y_F}{\partial \bar y}\right]+\overline{\dot\omega_F} \qquad (2.5)$$

Other species equation:

$$\bar\rho\frac{\partial Y_i}{\partial \bar t}+\overline{\rho u}\frac{\partial Y_i}{\partial \bar x}+\overline{\rho v}\frac{\partial Y_i}{\partial \bar y}=\frac{\partial}{\partial \bar x}\left[\overline{\rho D}\frac{\partial Y_i}{\partial \bar x}\right]+\frac{\partial}{\partial \bar y}\left[\overline{\rho D}\frac{\partial Y_i}{\partial \bar y}\right]+\bar{\dot\omega}_i \qquad (2.6)$$

where $i = O_2, CO_2, H_2O$

The gas phase chemistry is described by the one-step overall chemical reaction, which is $1[fuel] + f_O[O_2] \rightarrow f_C[CO_2] + f_H[H_2O] + \bar q$

where

f_O: stoichiometric $O_2/fuel$ mass ratio

f_C: stoichiometric $CO_2/fuel$ mass ratio

f_H: stoichiometric $H_2O/fuel$ mass ratio

$\bar q$: heat of combustion per unit mass of fuel

The corresponding reaction rate is described by a second-order Arrhenius-typed chemical kinetics, $\bar{\dot\omega}_F = -\bar B\bar\rho^2 Y_F Y_O \exp(-\bar E/\overline{RT})$, and the relationship among these reaction rates is expressed as follow. $\bar{\dot\omega}_F = \bar{\dot\omega}_O/f_O = -\bar{\dot\omega}_C/f_C = -\bar{\dot\omega}_H/f_H$.

Equation of state:

$$\overline{P} = \overline{\rho}\,\overline{R}\,\overline{T} \tag{2.7}$$

The viscosity variation with temperature is assumed to be:

$$\overline{\mu} = C_1 \overline{T}^{\,r} \tag{2.8}$$

where C_1 is a determined constant and the index r, usually ranged from 0.75 to 1.25 (Turns, 1996), is adopted as 1.0. Since the incoming flow velocity around the flame is much slower than the speed of sound, the ratio of the pressure difference to the absolute pressure throughout the region of interest is much less than one, implying that the dependence of density on pressure can be ignored. Therefore, the relationship between gas phase density and temperature can be rewritten as:

$$\overline{\rho} \propto \frac{1}{\overline{T}} \tag{2.9}$$

Solid phase governing equation:

Conservation of mass equation:

$$\frac{\partial \overline{m''_s}}{\partial \overline{y}} = -\frac{\partial \overline{\rho_s}}{\partial \overline{t}} = \overline{A_s}\left(\frac{\overline{\rho_s} - \overline{\rho_{sf}}}{1 - \dfrac{\overline{\rho_{sf}}}{\overline{\rho_{s\infty}}}}\right)\exp\left(-\frac{\overline{E_s}}{\overline{R}\,\overline{T_s}}\right) \tag{2.10}$$

Conservation of energy equation:

$$\overline{\rho_s}\,\overline{C_s}\frac{\partial \overline{T_s}}{\partial \overline{t}} = \overline{k_s}\frac{\partial^2 \overline{T_s}}{\partial \overline{x}^2} + \overline{k_s}\frac{\partial^2 \overline{T_s}}{\partial \overline{y}^2} + \frac{\partial \overline{m''_s}}{\partial \overline{y}}\left[\overline{L} + \left(\overline{C_s} - \overline{C_p}\right)\left(\overline{T_s} - \overline{T_\infty}\right)\right] - \overline{m''_s}\,\overline{C_p}\frac{\partial \overline{T_s}}{\partial \overline{y}} \tag{2.11}$$

These two equations provide a system of coupled partial differential equations to be solved for $\overline{\rho_s}$ and $\overline{T_s}$ under the given boundary and initial conditions and the heat transfer by conduction from gas phase to solid phase is obtained as soon as the gas phase equations are solved. The governing equations are subjected to the following initial and boundary conditions.

Initial conditions:

Gas phase:

At $\bar{t}\le 0$

$$\bar{u}=\bar{u}(y)=\frac{4\bar{u}}{H^2}(\bar{H}\bar{y}-\bar{y}^2),\bar{v}=0,Y_F=Y_C=Y_H=0,Y_O=Y_{O\infty},\bar{T}=\bar{T}_\infty \qquad (2.12)$$

Solid phase:

At $\bar{t}\le 0$

$$\overline{\rho}_s=\overline{\rho}_{s\infty},\overline{T_s}=\overline{T}_\infty \qquad (2.13)$$

Boundary conditions:

Gas phase:

At $\bar{x}=\bar{x}_{\min}$

$$\bar{u}=\bar{u}(y)=\frac{4\bar{u}}{\bar{H}^2}(\bar{H}\bar{y}-\bar{y}^2),\bar{v}=0 \qquad (2.14)$$

$$Y_F=Y_C=Y_H=0,Y_O=Y_{O\infty},\bar{T}=\overline{T_\infty},\left(1-\frac{2}{3\bar{a}}\frac{\partial}{\partial\bar{x}}\right)\overline{I_0}=\sigma\overline{T_\infty}^4 \qquad (2.15)$$

At $\bar{x}=\bar{x}_{\max}$

$$\frac{\partial\bar{u}}{\partial\bar{x}}=\frac{\partial\bar{v}}{\partial\bar{x}}=\frac{\partial\bar{T}}{\partial\bar{x}}=\frac{\partial\overline{I_0}}{\partial\bar{x}}=\frac{\partial Y_F}{\partial\bar{x}}=\frac{\partial Y_O}{\partial\bar{x}}=\frac{\partial Y_C}{\partial\bar{x}}=\frac{\partial Y_H}{\partial\bar{x}}=0 \qquad (2.16)$$

At $\bar{y}=\bar{\tau}$, $-\bar{L}\le\bar{x}\le 0$

$$\bar{u}=0,\bar{T}=\overline{T_s},\overline{m''_w}=\overline{\rho_w}\,\overline{v_w} \qquad (2.17)$$

$$\overline{m''_w}Y_{Fs}=\overline{m''_w}Y_{Fw}-\overline{\rho}\,\overline{D}\frac{\partial Y_F}{\partial\bar{y}}\bigg|_{\bar{y}=\bar{\tau}} \qquad (2.18)$$

$$\overline{m''_w}Y_{is}=\overline{m''_w}Y_{iw}-\overline{\rho}\,\overline{D}\frac{\partial Y_i}{\partial\bar{y}}\bigg|_{\bar{y}=\bar{\tau}},\ \text{where}\ i=O_2,CO_2,H_2O,\ \ Y_{Fs}=1,Y_{is}=0 \qquad (2.19)$$

$$\left(1-\frac{2}{3\bar{a}}\frac{\partial}{\partial\bar{y}}\right)\overline{I_0}=\varepsilon\overline{T_s}^4 \qquad (2.20)$$

At $\bar{y}=\bar{\tau}$, $\bar{x}_{\min}\le\bar{x}\le-\bar{L}$, $0\le\bar{x}\le\bar{x}_{\max}$

$$\bar{u}=\bar{v}=\frac{\partial\bar{T}}{\partial\bar{y}}=\frac{\partial\overline{I_0}}{\partial\bar{y}}=\frac{\partial Y_F}{\partial\bar{y}}=\frac{\partial Y_O}{\partial\bar{y}}=\frac{\partial Y_C}{\partial\bar{y}}=\frac{\partial Y_H}{\partial\bar{y}}=0 \qquad (2.21)$$

At $\bar{y}=\bar{y}_{\max}$

$$\bar{u} = \bar{v} = \frac{\partial \bar{T}}{\partial \bar{y}} = \frac{\partial \bar{I}_0}{\partial \bar{y}} = \frac{\partial Y_F}{\partial \bar{y}} = \frac{\partial Y_O}{\partial \bar{y}} = \frac{\partial Y_C}{\partial \bar{y}} = \frac{\partial Y_H}{\partial \bar{y}} = 0 \qquad (2.22)$$

Solid phase:

At $\bar{x} = -L$

$$\bar{\rho}_s = \bar{\rho}_{s\infty}\,,\quad \bar{T}_s = \bar{T}_\infty \qquad (2.23)$$

At $\bar{x} = \bar{x}_{\min}$ and $\bar{x} = \bar{x}_{\max}$

$$\frac{\partial \bar{T}_s}{\partial \bar{x}} = 0 \qquad (2.24)$$

At $\bar{y} = \bar{y}_{\min}$ and $\bar{x}_{\min} \le \bar{x} \le \bar{x}_{\max}$

$$\frac{\partial \bar{T}_s}{\partial \bar{y}} = 0 \qquad (2.25)$$

At $\bar{y} = \bar{\tau}$, $-\bar{L} \le \bar{x} \le 0$

$$\bar{k}_s \frac{\partial \bar{T}_s}{\partial \bar{y}} = \bar{\mu} \frac{\partial \bar{T}}{\partial \bar{y}} + \bar{q}_{ex} - \frac{\varepsilon\sigma}{\bar{\tau}}\left(\bar{T}_s^{\,4} - \bar{T}_\infty^{\,4}\right) + \frac{\bar{q}_y^{\,r}}{\bar{\tau}} \qquad (2.26)$$

where $-\frac{\varepsilon\sigma}{\bar{\tau}}\left(\bar{T}_s^{\,4} - \bar{T}_\infty^{\,4}\right)$ and $\frac{\bar{q}_y^{\,r}}{\bar{\tau}}$ are heat lost by radiation from solid to ambient gas and radiation feedback from gas to solid, respectively.

At $\bar{y} = \bar{\tau}$, $\bar{x}_{\min} \le \bar{x} \le -\bar{L}$ and $0 \le \bar{x} \le \bar{x}_{\max}$

$$\frac{\partial \bar{T}_s}{\partial \bar{y}} = 0 \qquad (2.27)$$

2.3 Radiation model

The transfer of energy from and within a burning environment is controlled by diffusive, convective and radiative processes. Because the temperatures associated with combustion are high, a proper physical description needs to account for radiation unless the characteristic radiation-to-convection ratio of the system is small. Bhattacharjee and Grosshandler (1989) define the following radiation/convection parameter, ψ, in terms of the flame, surrounding wall and inlet temperatures, the mass flux of material brought into the flame times its heat capacity, $\rho_i u_i c_p$, and the optical thickness of the system based upon the absorption coefficient, a , and a stream-wise dimension. The highly absorbing fires in large volumes can be strongly influenced by radiation; conversely, a large thermal input can diminish the importance of radiation if the absorption properties, temperature and volume of interest remain about constant. However, the absorption coefficient of the cool gases surrounding a fire can influence the transfer of energy from a burning object to a distant object.

The radiation model used in the study of Wu and Chen (2004) is the P1 model, which the semi-gray scheme is adopted to define the effective absorption coefficient. Because the gas phase radiative properties are highly dependent on the temperature and mixture concentrations, the simple assumptions are unrealistic and unsuitable to determine the radiative properties. Therefore, this work modifies the original model of Wu and Chen (2004) by using the narrow band model instead of the P1 model. The present radiation model incorporates the subroutine RADCAL developed by Grosshandler (1993) to determine the gas absorption coefficient. The absorption coefficient of the combined gases is calculated from a narrow band model and a combination a tabulated spectral properties and theoretical approximations to the vibration-rotational molecular bands.

For the forced convection channel flow, the radiation terms $\frac{\partial \bar{q}_x^r}{\partial \bar{x}}$ and $\frac{\partial \bar{q}_y^r}{\partial \bar{y}}$ in Eq. (2.4) can be expressed as (Siegel and Howell, 1992):

$$\frac{\partial \bar{q}_x^r}{\partial \bar{x}} = 4\pi \bar{a}\left(\frac{\sigma \bar{T}^4}{\pi} - \bar{I}\right) \qquad (2.28)$$

$$\frac{\partial \bar{q}_y^{\,r}}{\partial \bar{y}} = 4\pi\bar{a}\left(\frac{\sigma\bar{T}^4}{\pi} - \bar{I}\right) \tag{2.29}$$

Substitute Eqs. (2.28) and (2.29) into the energy equation (2.4) and the radiation term can be expressed as

$$\nabla\cdot\bar{q}^{\,r} = \frac{\partial \bar{q}_x^{\,r}}{\partial \bar{x}} + \frac{\partial \bar{q}_y^{\,r}}{\partial \bar{y}} = 8\pi\bar{a}\left(\frac{\sigma\bar{T}^4}{\pi} - \bar{I}\right) \tag{2.30}$$

in which $\frac{\sigma\bar{T}^4}{\pi}$ represents the blackbody intensity, $\bar{I_b}$, and $\bar{I}$ is the radiation intensity. $\bar{I}$ can be obtained from the solution of the radiation transfer equation, which is listed as below (Grosshandler,1980):

$$I = \int_{\omega=0}^{\infty}\int_{0}^{U} k_\omega \frac{e_{b\omega}}{\pi}\exp\left(-\int_0^u k_\omega du'\right)du\,d\omega \tag{2.31}$$

where k_ω and $e_{b\omega}$ respectively represent the spectral absorption coefficient and Planck’s blackbody distribution function. The spectral absorption coefficient and the spectral optical depth of the combustion products, including carbon dioxide and water vapor, are calculated according to the narrow band model, RADCAL (Grosshandler, 1993). RADCAL utilizes the optical depth to determine the spectral transmittance and intensity as each new spatial element is added to the radiating path. Radiation from the far wall is counted after being attenuated by the calculated transmittance along the total length of the path. Then, the spectral intensity is integrated across the spectrum to obtain the total radiated energy flux.

The radiation transfer equation (2.31) can be represented by the spectral transmittance, τ_ω, and the expression can be rewritten as

$$I = -\int_{\omega=0}^{\infty}\int_{1}^{\tau_\omega(l)} \frac{e_{b\omega}(T,\omega)}{\pi}d\tau_\omega \tag{2.32}$$

where τ_ω is defined as

$$\tau_\omega(l) = e^{-X_\omega(l)} \tag{2.33}$$

and X_ω represents the optical depth, defined as

$$X_\omega(l)=\int_0^l k_\omega(l')\frac{\rho}{\rho_0}dl' \tag{2.34}$$

for the mixture of carbon dioxide and water vapor. The combined optical depth along a non-homogeneous path can be obtained by adding together the contributions to optical depth from each species, therefore, Eq. (2.34) can be rewritten in the form as (Grosshandler,1980):

$$X_{\omega,mix}(l)=\int_0^l\left[k_{\omega,w}(l')P_w(l')+k_{\omega,c}(l')P_c(l')\right]\frac{T_0}{P_0T(l')}dl' \tag{2.35}$$

where the subscripts *c* and *w* refer to the carbon dioxide and water vapor, respectively.

The radiation properties of carbon dioxide and water vapor are highly non-gray and the steep gradients of the temperature and composition concentrations in the combustion system cause significant non-homogeneity for the radiation properties. Therefore, the determination of proper values of k_ω used in Eq. (2.35) is an important issue. The Curtis-Godson approximation (1964) presented the absorption coefficient in a non-homogeneous gas of path length, *l*, and the expression is

$$k_{\omega,CG}(l)=\overline{S/d}_{CG}\left[1+\frac{\left(\int_0^l\frac{\rho(l')}{\rho_0}dl'\right)^2(\overline{S/d}_{CG})^2}{4\int_0^l\gamma_L\overline{1/d}(l')\overline{S/d}(l')\rho(l')/\rho_0dl'}\right]^{-1/2} \tag{2.36}$$

where the $\overline{S/d}$ is the mean line-strength to spacing parameter and can be found by summing up the contributions to line strength, S, from each rotational line divided by the distance, d, between adjacent lines. The other important parameter in the equation is $\overline{1/d}$, which represents the mean inverse line spacing.

The two narrow band parameters, $\overline{S/d}$ and $\overline{1/d}$, are both functions of temperature and wave number. For the carbon dioxide, they are determined from the modified anharmonic oscillator/rotator model developed by Malkmus (1963). For the water vapor, they are tabulated based upon the experimental measurements by Ludwig et al. (1973). The narrow band model, RADCAL (Grosshandler, 1993), utilizes these data of carbon dioxide and water vapor to calculate the absorption coefficient for the primary infrared bands. Finally, the spectral optical depths of each individual species can be determined and the radiation intensity of combustion gases will be obtained by the radiation transfer equation.

2.4 Governing equations in non-dimensional form

This combustion model solves the system of governing equations non-dimensionally. This procedure can avoid too large or too small values appearing in computation. Now a nondimensionalization procedure is presented as follows. The choice for the reference velocity ($\overline{V_r}$), temperature ($\overline{T^*}$) and the characteristic length ($\bar{\delta}$) are specified first. The opposed flow velocity is selected as reference velocity in this study. The reference temperature is defined as the average temperature of the ambient temperature ($\overline{T_\infty}$) and adiabatic flame temperature ($\overline{T_f}$). The thermal diffusion length is chosen as the characteristic length, defined as $\bar{\delta} = \overline{\alpha^*}/\overline{V_r}$, which is based on the balance between the convection and conduction terms in the energy equation. According to the selected reference velocity, temperature and characteristic length, the dimensionless quantities are defined as follows.

$$x = \bar{x}/\bar{\delta} \qquad y = \bar{y}/\bar{\delta} \qquad t = \bar{t}\,\overline{V_r}^{\,2}/\overline{\alpha^*}$$

$$u = \bar{u}/\overline{V_r} \qquad v = \bar{v}/\overline{V_r} \qquad m'' = \overline{m''}/\overline{\rho^*}\,\overline{V_r}$$

$$T = \bar{T}/\overline{T_\infty} \qquad \gamma = \overline{T^*}/\overline{T_\infty} \qquad \rho = \bar{\rho}/\overline{\rho^*}$$

$$g = \overline{g} / \overline{g_e} \qquad \mu = \overline{\mu} / \overline{\mu^*} \qquad P = (\overline{P} - \overline{P_\infty}) \Big/ \overline{\rho^*}\,\overline{V_r}^{\,2}$$

$$E = \overline{E} \Big/ \overline{R}\,\overline{T_\infty} \qquad q = \overline{q} / \overline{C_p}\,\overline{T_\infty} \qquad \Pr = \overline{\nu} / \overline{\alpha}$$

$$Le = \overline{\alpha} / \overline{D} \qquad Da = \overline{B}\,\overline{\rho^*}\,\overline{\delta} / \overline{V_r} \qquad Gr = \overline{g}(\overline{\rho_\infty} - \overline{\rho_f})\overline{\delta}^3 \Big/ \overline{\rho^*}\,\overline{\nu^*}^{\,2}$$

$$C = \overline{C_p} \Big/ \overline{C_s} \qquad L = \overline{L} / \overline{C_s}\,\overline{T_\infty} \qquad k_s = \overline{k_s} \Big/ \overline{k^*}$$

$$\rho_s = \overline{\rho_s} \Big/ \overline{\rho_{s\infty}} \qquad T_s = \overline{T_s} / \overline{T_\infty} \qquad \alpha_s = \overline{\alpha_s} / \overline{\alpha^*}$$

$$E_s = \overline{E_s} / \overline{R}\,\overline{T_\infty} \qquad A_s = \overline{A_s}\,\overline{\alpha^*} \Big/ \overline{V_r}^{\,2} \qquad q_{ex} = \overline{q_{ex}}\,\overline{\alpha^*} / \overline{\tau}\,\overline{\rho_{s\infty}}\,\overline{C_s}\,\overline{T_\infty}\,\overline{V_r}^{\,2}$$

$$m_s'' = \overline{m_s''}\,\overline{\alpha^*} / \overline{\rho_{s\infty}}\,\overline{V_r}^{\,2}\,\overline{\tau} \qquad \tau = \overline{\tau}\,\overline{C_s}\,\overline{\rho_{s\infty}}\,\overline{V_r} / \overline{k^*} \qquad K_P = \overline{K_P} \cdot \overline{\delta}$$

$$\mathrm{Re} = \overline{\rho^*}\,\overline{\alpha^*} \Big/ \overline{\mu^*} \qquad I_0 = \overline{I_0} \Big/ \sigma \overline{T_\infty}^{\,4} \qquad a = \overline{a}\,\overline{\delta}$$

$$N_\infty = \overline{k^*}\,\overline{V_r} / \overline{\sigma}\,\overline{T_\infty}^{\,3}\,\overline{\alpha^*}$$

The notation appeared above can be referred in nomenclature and the quantities with superscript * are evaluated at reference temperature. Consequently, the non-dimensional equations can be obtained by substituting above definitions into the dimensional equations. The resultant non-dimensional governing equations for both the gas and solid phases are expressed as follows.

Gas phase:

Continuity equation:

$$\frac{\partial \rho}{\partial t} + \frac{\partial(\rho u)}{\partial x} + \frac{\partial(\rho v)}{\partial y} = 0 \tag{2.37}$$

X-momentum equation:

$$\rho\frac{\partial u}{\partial t} + \rho u\frac{\partial u}{\partial x} + \rho v\frac{\partial u}{\partial y} = -\frac{\partial P}{\partial x} + \frac{\partial}{\partial x}\left[\frac{2\mu}{\mathrm{Re}}\frac{\partial u}{\partial x} - \frac{2\mu}{3\mathrm{Re}}\left[\frac{\partial u}{\partial x} + \frac{\partial v}{\partial y}\right]\right] + \frac{\partial}{\partial y}\left[\frac{\mu}{\mathrm{Re}}\left[\frac{\partial u}{\partial y} + \frac{\partial v}{\partial x}\right]\right] + \frac{Gr}{\mathrm{Re}^2}(\rho_\infty - \rho) \tag{2.38}$$

Y-momentum equation:

$$\rho\frac{\partial v}{\partial t}+\rho u\frac{\partial v}{\partial x}+\rho v\frac{\partial v}{\partial y}=-\frac{\partial P}{\partial y}+\frac{\partial}{\partial y}\left[\frac{2\mu}{\mathrm{Re}}\frac{\partial v}{\partial y}-\frac{2\mu}{3\mathrm{Re}}\left[\frac{\partial u}{\partial x}+\frac{\partial v}{\partial y}\right]\right]+$$
$$\frac{\partial}{\partial x}\left[\frac{\mu}{\mathrm{Re}}\left[\frac{\partial u}{\partial y}+\frac{\partial v}{\partial x}\right]\right] \tag{2.39}$$

Energy equation:

$$\rho\frac{\partial T}{\partial t}+\rho u\frac{\partial T}{\partial x}+\rho v\frac{\partial T}{\partial y}=\frac{1}{\Pr\mathrm{Re}}\left[\frac{\partial}{\partial x}\left[\mu\frac{\partial T}{\partial x}\right]+\frac{\partial}{\partial y}\left[\mu\frac{\partial T}{\partial y}\right]\right]-$$
$$q\dot{\omega}_F-\frac{a}{N_\infty}(T^4-I_0) \tag{2.40}$$

where $\dot{\omega}_F=-Da\rho^2Y_FY_O\exp(-E/T)$

Fuel species equation:

$$\rho\frac{\partial Y_F}{\partial t}+\rho u\frac{\partial Y_F}{\partial x}+\rho v\frac{\partial Y_F}{\partial y}=\frac{1}{\Pr\mathrm{Re}\,Le}\left[\frac{\partial}{\partial x}\left[\mu\frac{\partial Y_F}{\partial x}\right]+\frac{\partial}{\partial y}\left[\mu\frac{\partial Y_F}{\partial y}\right]\right]+\dot{\omega}_F \tag{2.41}$$

Other species equation:

$$\rho\frac{\partial Y_i}{\partial t}+\rho u\frac{\partial Y_i}{\partial x}+\rho v\frac{\partial Y_i}{\partial y}=\frac{1}{\Pr\mathrm{Re}\,Le}\left[\frac{\partial}{\partial x}\left[\mu\frac{\partial Y_i}{\partial x}\right]+\frac{\partial}{\partial y}\left[\mu\frac{\partial Y_i}{\partial y}\right]\right]+f_i\dot{\omega}_F \tag{2.42}$$

where $i=O_2,CO_2,H_2O$

Equation of state:

$$\rho\cong\frac{\gamma}{T} \tag{2.43}$$

The equation for viscosity variation with temperature

$$\mu=\frac{T}{\gamma} \tag{2.44}$$

Solid phase:

Conservation of mass:

$$\frac{\partial\rho_s}{\partial t}=-(A_s)\left(\frac{\rho_s-\rho_{sf}}{1-\rho_{sf}}\right)\exp\left(-\frac{E_s}{T_s}\right) \tag{2.45}$$

Conservation of energy:

$$\rho_s\frac{\partial T_s}{\partial t}=\frac{\partial m_s''}{\partial y}\tau[L+(1-C)(T_s-1)]+\alpha_s\frac{\partial^2T_s}{\partial x^2}+\alpha_s\frac{\partial^2T_s}{\partial y^2}-(Cm_s''\tau)\frac{\partial T_s}{\partial y} \tag{2.46}$$

The non-dimensional gas and solid governing equations are listed in Table 1. Finally, the initial and boundary conditions in dimensionless form are presented as follows.

Gas phase initial condition:

At $t \le 0$

$$u = u(y) = \frac{4u_\infty}{h^2}(hy - y^2), v = 0, Y_F = Y_C = Y_H = 0, Y_O = Y_{O\infty}, T = 1 \tag{2.47}$$

Solid phase initial condition:

At $t \le 0$

$$\rho_s = T_s = 1 \tag{2.48}$$

Gas phase boundary conditions:

At $x = x_{\min}$

$$u = u(y) = \frac{4u_\infty}{h^2}(hy - y^2), v = 0, Y_F = Y_C = Y_H = 0, Y_O = Y_{O\infty} \tag{2.49}$$

$$T = 1, \left(1 - \frac{2}{3a}\frac{\partial}{\partial x}\right) I_0 = 1 \tag{2.50}$$

At $x = x_{\max}$

$$\frac{\partial u}{\partial x} = \frac{\partial v}{\partial x} = \frac{\partial T}{\partial x} = \frac{\partial Y_F}{\partial x} = \frac{\partial Y_O}{\partial x} = \frac{\partial Y_C}{\partial x} = \frac{\partial Y_H}{\partial x} = \frac{\partial I_0}{\partial x} = 0 \tag{2.51}$$

At $y = \tau$, $-L \le x \le 0$

$$u = 0, \quad T = T_s, \quad m_w'' = \rho_w v_w \tag{2.52}$$

$$m_w'' Y_{Fs} = m_w'' Y_{Fw} - \frac{\mu}{\Pr \operatorname{Re} Le} \left.\frac{\partial Y_F}{\partial y}\right|_{y=\tau} \tag{2.53}$$

$$m_w'' Y_{is} = m_w'' Y_{iw} - \frac{\mu}{\Pr \operatorname{Re} Le} \left.\frac{\partial Y_i}{\partial y}\right|_{y=\tau}, \text{ where } i = O, C, H \; Y_{Fs} = 1, Y_{is} = 0 \tag{2.54}$$

$$\left(1 - \frac{2}{3a}\frac{\partial}{\partial y}\right) I_0 = \varepsilon T_s^4 \tag{2.55}$$

At $y = \tau$, $x_{\min} \le x < -L$ and $0 < x \le x_{\max}$

$$u = v = \frac{\partial T}{\partial y} = \frac{\partial Y_F}{\partial y} = \frac{\partial Y_O}{\partial y} = \frac{\partial Y_C}{\partial y} = \frac{\partial Y_H}{\partial y} = \frac{\partial I_0}{\partial y} = 0 \tag{2.56}$$

At $y = y_{\max}$

$$u = v = \frac{\partial T}{\partial y} = \frac{\partial Y_F}{\partial y} = \frac{\partial Y_O}{\partial y} = \frac{\partial Y_C}{\partial y} = \frac{\partial Y_H}{\partial y} = \frac{\partial I_0}{\partial y} = 0 \tag{2.57}$$

Solid phase boundary conditions:

At $x = -L$

$$\rho_s = T_s = 1 \tag{2.58}$$

At $x = x_{\max}$ and $x = x_{\min}$

$$\frac{\partial T_s}{\partial x} = 0 \tag{2.59}$$

At $y = y_{\min}$ and $x_{\min} \le x \le x_{\max}$

$$\frac{\partial T_s}{\partial y} = 0 \tag{2.60}$$

At $y = \tau$, $-L \le x \le 0$

$$K_s \left.\frac{\partial T_s}{\partial y}\right|_{y=\tau} = \mu \left.\frac{\partial T}{\partial y}\right|_{y=\tau} + \frac{1}{\tau N_\infty}\frac{1}{3a}\left.\frac{\partial I_0}{\partial y}\right|_{y=\tau} + q_{ex} - \frac{1}{\tau N_\infty}\cdot \varepsilon (T_s^4 - 1) \tag{2.61}$$

At $y = \tau$, $x_{\min} \le x < -L$ and $0 < x \le x_{\max}$

$$\frac{\partial T_s}{\partial y} = 0 \tag{2.62}$$

2.5 Solution methodology

This numerical study is conducted using the opposed flow velocity and temperature and the solid fuel thickness as parameters to investigate flame ignition and the subsequent downward flame spread behavior. Notably, in the present simulation, a finite-length fuel slab is used, the ignition/combustion is in a two-dimensional wind tunnel, and both gas and solid phase radiations are considered. The ambient oxygen concentration in this model is fixed at 0.233.

The numerical calculation is initiated from a prescribed external radiant heat flux, q_{ex}, input on the solid fuel surface at time $t=0$. The profile of the incident radiation flux is a Gaussian distribution and its non-dimensional form can be expressed as

$$q_{ex} = Q_{\max} \exp\left(-\alpha x^2\right) \tag{2.63}$$

where $Q_{\max}$ is the non-dimensional peak value of the external radiant heat flux, α is a Gaussian distribution shape factor and the x is the non-dimensional distance along the solid fuel surface. The solid fuel absorbs the external heat to raise its temperature gradually and pyrolyze the fuel vapor mixing the air to form the flammable mixture. The ignition occurs as soon as the gas phase temperature raises high enough to enhance the chemical reaction and the flame stars to propagate downward subsequently.

The finite difference equation for each variable is obtained by integrating the differential equation over the relative computational cell, associating with specified interpolation applied on the interface between the variable of two adjacent grid points. The detailed derivation of finite difference equations is carried out in Appendix A. The resulting finite difference equations are:

continuity equation:

$$C_E u_P - C_W u_W + C_N v_P - C_S v_S = 0 \tag{2.64}$$

momentum equations:

$$a_P^u u_P = \sum a_{nb}^u u_{nb} + S_C^u + A_{ew}^u (p_P - p_E) \tag{2.65}$$

$$a_P^v v_P = \sum a_{nb}^v v_{nb} + S_C^v + A_{ns}^v (p_P - p_N) \tag{2.66}$$

The energy, fuel and oxidizer species equations can be expressed as following general form of

$$a_P^\phi \phi_P = \sum a_{nb} \phi_{nb} + S_C^\phi \tag{2.67}$$

where ϕ represents temperature, fuel and oxidizer mass fractions. The summations are applied over E, W, N and S points, the values of dependent variables u, v, ϕ and p are evaluated at (n+1) iteration and the expressions of coefficients such as A's, a's, S's and C's are also given in Appendix A. The appearance of Equs. (2.64)-(2.67) seems to be linear, but it is not because the coefficients are also the function of dependent variable itself.

The numerical scheme utilizes the SIMPLE (Semi-Implicit Method for Pressure-Linked Equations) algorithm developed by Patankar (1980). Since the momentum equations can be solved only when the pressure field is given or somehow estimated. An equation for pressure is needed to resolve the problem. The thinking of SIMPLE procedure is that unless the correct pressure field is employed, the resulting velocity will not satisfy the continuity equation. Therefore, a pressure correction equation is derived by linking the continuity equation. The derivation is outlined next. Because the pressure field is unknown in the beginning, a P^* is guessed in momentum equation. An imperfect velocity field based on guessed P^* will be denoted by u^* and v^*. This crossed velocity field is resulted from the following equations.

$$a_p^u u_p^+ = \sum a_{nb}^u u_{nb}^+ + S_C^u + (p_P^+ - p_E^+) A_{P'}^u \tag{2.68}$$

$$a_p^v v_p^+ = \sum a_{nb}^v v_{nb}^+ + S_C^v + (p_P^+ - p_N^+) A_{P'}^v \tag{2.69}$$

The continuity equation generally will not be satisfied by employing u^* and v^* into it, instead a net non-zero mass source m_p will be generated where

$$m_P = C_E u_P^+ - C_W u_E^+ + C_N v_P^+ - C_S v_S^+ \tag{2.70}$$

Since the mass source is originated from P^*, the next step is to fine a way of improving the guessed P^* such that the resulting crossed velocity will progressively get closer to satisfy the continuity equation. First, a correct pressure is proposed that

$$p = p^{+} + p^{'} \tag{2.71}$$

where $p^{'}$ is called the pressure correction. Suppose that the true velocity components u and v respond to this pressure change in the following ways:

$$u_P = u_P^{+} + (p_P^{'} - p_E^{'})(A_{ew}^{u} / a_p^{u}) \tag{2.72}$$

$$v_P = v_P^{+} + (p_P^{'} - p_N^{'})(A_{ns}^{v} / a_p^{v}) \tag{2.73}$$

Then, substitute the velocity components into the continuity equation using the above velocity-correction formulas (Eqs. (2.72) and (2.73)), we can obtain, after rearrangement, the following difference equation for $p^{'}$:

$$a_P^P p_P^{'} = a_E^P p_E^{'} + a_W^P p_W^{'} + a_N^P p_N^{'} + a_S^P p_S^{'} + S_C^P \tag{2.74}$$

where

$$a_E^P = C_E (A_{ew}^{u} / a_p^{u})_{E'}$$

$$a_W^P = C_W (A_{ew}^{u} / a_p^{u})_{P'}$$

$$a_N^P = C_N (A_{ns}^{v} / a_p^{v})_{N'}$$

$$a_S^P = C_S (A_{ns}^{v} / a_p^{v})_{P'}$$

$$a_P^P = a_E^P + a_W^P + a_N^P + a_S^P$$

$$S_C^P = -m_p$$

Once $p^{'}$ is obtained from Eq. (2.74), the velocities and pressure will be updated by $p^{'}$ through Eqs. (2.71)-(2.73). In the computation, as soon as the numerical results meet the criteria of convergence, the value of m_P will come out to be practically zero for all control volumes. Therefore, $p^{'} = 0$ at all grid points will be acceptable solutions of Eq. (2.74) and the crossed velocities and pressure will be the correct velocities and pressure.

The present radiation model incorporates the subroutine RADCAL developed by Grosshandler (1993) to determine the gas absorption coefficient. Since the radiation subroutine is complicated and consumes much computing time, it is executed once after ten iterations in each time step. The model is solved with a marching time step. At each time step, the gas and solid phase equations are solved separately. The solid phase equations are coupled with the gas phase equations through a mass and energy balance linkage. An iteration procedure is performed until all variables in the gas and solid phases converge to their respective acceptable criteria. For each grid point a residual *R* can be calculated as

$$R = \sum a_{nb}\phi_{nb} + S_c - a_p\phi_p \tag{2.75}$$

Obviously, when the discretization equation is completely satisfied, *R* should be zero. In practice, this is impossible to satisfy. Because of this, the suitable convergence criterion should be selected that the largest value of $|R|$ in the computational domain is less than a convergence criterion, ε. The value of ε is set to be 0.01 in this work. When the conditions of $|R|_{\max} < \varepsilon$ satisfied simultaneously for each dependent variable, the iteration procedure is stopped. Thereafter, the procedure moves to the next time step. Computations are carried out using a non-uniform mesh distribution as shown in the figure 2.2. The calculation performed with a non-uniform mesh according to the formula listed as below:

$$Dx(I) = Dx(I-1)\times 1.042 \text{ if } Dx(I) \geq 2.5,\ Dx(I) = 2.5 \text{ for } x < 0 \tag{2.76}$$

$$Dx(I) = Dx(I-1)\times 1.1 \text{ if } Dx(I) \geq 2.5,\ Dx(I) = 2.5 \text{ for } x > 0 \tag{2.77}$$

$$Dy(J) = Dy(J-1)\times 1.1 \text{ if } Dy(J) \geq 2.5,\ Dy(J) = 2.5 \tag{2.78}$$

The smallest grid is 0.01 cm wide. Most of the grid points are clustered in an external radiative heating region to capture drastic variations in the flame; the grids then expand upstream and downstream. The tests of the independence of the grid-size were conducted in advance and the results are shown in Table 2. According to the grid-independence test, a non-dimensional time step of Δt = 10 (equivalent to a real time of 0.02 s) and non-uniform grid dimensions of 290×95 were found to optimize the balance among resolution, computational time and memory space requirements. The time step that was selected in this work is much smaller than those used in previous studies, such as 0.0548 s in Lin and Chen (2000) and 0.05 s in Wu and Chen (2004). Hence, the present computation is expected to be more accurate and suitable for examining gas phase ignition. In sum, the computational procedure is shown in figure 2.3 and the whole produce is expressed briefly as follows.

1. Read initial conditions for both gas and solid phase.
2. Solve solid phase conservation equations.
3. Combine interface conditions.
4. Guess the pressure field P^*
5. Solve the momentum equations to obtain u^*, v^*.
6. Solve pressure correction equation to obtain P'.
7. Calculate P by adding P' to P^*
8. Calculate u, v from the velocity correction formulas
9. Solve the discretization equations for other variables (temperature and concentration), return to step 2, and repeat the whole procedures until a converged solution is obtained.
10. Update initial conditions for all variables and march next time step.

The computational time associated with each case was approximately two days on a 2.8GHz Intel Pentium 4 PC at National Chiao Tung University.

Chapter 3

Results and discussion

As mentioned previously, this dissertation consists of three parts. In this chapter, the computation results as well as the detailed discussion for each part are given in the following sections. These results are also compared with corresponding experimental measurements and numerical predictions.

The method and apparatus used to conduct the experiment are briefly described as follows. The wind tunnel used in the experiment is 70 cm long and has 10*10 cm^2 rectangular cross section. The test specimens are PMMA slabs, which are 30 cm long, 3 cm wide and have thicknesses of 0.82 cm and 1.74 cm, respectively. Each specimen is mounted on the groove in the test section, whose sides are covered with asbestos plates to minimize side effects. Remind that the solid fuel is assumed to be homogeneous that its compositions are uniform and its thickness is remained constant by assuming the flame spreads relatively fast enough that the fuel surface near the flame base remains approximately flat. The air, heated by the heater, is drawn into the entire test section and then flows over the specimen. The specimen is ignited using an electrically heated Ni-Cr wire, which is placed above the PMMA surface. A 15V A.C. current is passed through the Ni-Cr wire. The current is cut off when the flame is ignited. The laser holographic interferometry and K- type thermocouples are utilized to measure the local gas temperature in the test section and the PMMA surface temperature, separately. The thermocouples are separated by 5 cm. A thermocouple signal is recorded using a multi-channel Yokogawa DA-2500 analyzing recorder and the flame spread rate is determined by dividing 5 cm by the time recorded to have elapsed between the peaks on each of the two temperature traces.

3.1 Numerical study for downward flame spread over a finite-length PMMA slab with radiation effect in a two-dimensional wind tunnel

In this topic, several aspects of the original combustion model of Wu et al. (2003) are modified to investigate the downward flame spread over a finite-length PMMA slab with radiation effect in a two-dimensional wind tunnel. Parametric studies were conducted by changing the opposed flow velocity and temperature and the solid fuel thickness, in the same ranges as in the experiment of Pan (1999), to enable the results to be compared fairly with those of Pan (1999) and Wu et al. (2003). Notably, in the simulation of Wu et al. (2003), the fuel slab extends infinitely in both directions, the ignition/combustion is in an open atmosphere and both gas and solid radiations are neglected. The discrepancies between the previous combustion models of Wu et al. (2003) and present work are listed in the Table 3. The ambient oxygen concentration in the present model is fixed at 0.233. Table 4 present the physical data used in this study and the non-dimensional parameters are in Table 5.

In the initial state, the solid fuel of 298K is heated by the hotter opposed flow of 313K, 333K and 353K, respectively, and its temperature raises gradually. As soon as the solid fuel temperature reaches a steady one, an external heat flux stars to heat the solid fuel surface. Figure 3.1.1 shows the steady state temperature distributions along the PMMA surface before the external radiative heat flux is incident on the fuel under three opposed flow velocities $\bar{u}_\infty = 40 cm/s$, $70 cm/s$ and $100 cm/s$ and opposed flow temperatures from 313K to 353K. The solid and dashed lines represent the Pan's experimental (1999) and present numerical results, respectively. The experimental error in the temperature measurement is

$\pm 5.2K$. The predictions are quite consistent with the measurements. From this figure, it can be found that the differences decline as the flow velocity increases at fixed flow temperature, but increases with the flow temperature at a fixed flow velocity. The former result follows for the fact that the upstream boundary layer may not have been fully developed in the experimental test section, especially in the low velocity regime. However, the flow in the numerical simulation is assumed to be fully developed and the boundary layer thickness is fixed. For the latter result, the temperature distribution in the experimental tunnel is expected to be less uniform as opposed flow temperature increases at fixed flow velocity. In addition, the errors of the instruments used to measure temperature such as the thermocouple and data recorder, also increase with the opposed flow temperature.

Figure 3.1.2 displays the time history of the flame profiles from ignition to subsequent flame spread for $\overline{u_\infty} = 40cm/s$, $\overline{T_i} = 313K$ and $\overline{\tau} = 0.82cm$. The right half of the figure is the fuel and oxidizer mass fraction distributions whereas the left half of the figure shows the temperature contours and flow velocity vector distributions. At $\overline{t} = 0$, the incident radiation flux of the Gaussian distribution starts to heat the solid fuel. The solid fuel absorbs the heat and raises its temperature gradually. While the solid fuel reaches the pyrolysis temperature, the solid fuel pyrolyzes the fuel vapor mixing with the air to form the flammable mixture, as demonstrated in figure 3.1.2(a). However, the flame is not ignited due to a small amount of fuel vapor and the low gas phase temperature. Thereafter, the concentration of the flammable mixture increases continuity and the gas phase temperature raises high enough to enhance the chemical reaction as well. In this interval, the fuel vapor and air are now well premixed by the convection and diffusion. According to Nakabe et al. (1994) and Ferkul and T'ien (1994), the gas phase ignition as occurring as soon as the dimensional reaction rate ($\overline{\dot{\omega}_F}$) reaches $10^{-4}\ g/cm^3 s$. The starting point of gas phase ignition occurs at $t = 14.12s$, as shown in figure 3.1.2(b). The thermal plume downstream is longer because of the high opposed flow. An extra source for the gas phase temperature rise is from the chemical reaction in addition to the solid conduction.

After that, the chemical reaction rate increases sharply and releases much heat, resulting in the flame grows quickly within a very short period and the flame size reaches a maximum value at $\mathrm{t} = 14.14\mathrm{s}$, as illustrated in figure 3.1.2(c). As following, the flame size and temperature reduce simultaneously, as displayed in figure 3.1.2(d). The flame gradually transfers from a premixed flame to a diffusion one. From the fuel and oxidizer mass fraction distributions in the figure 3.1.2(d), it can be seen that the fuel vapor and oxidizer is premixed in the flame front, whereas the fuel vapor and oxidizer is mixed by the diffusion in the flame downstream region. In order to sustain the flame itself, the flame front begins to extend upstream (downward direction) to pyrolyze the solid fuel to generate more fuel vapor to form the flammable mixture for support itself, as depicted from figure 3.1.2(e) to figure 3.1.2(g). After that, the steady flame spreads downward with the flame front.

Figure 3.1.3 plots the ignition delay time versus the opposed flow temperature at three opposed flow velocities $\overline{u_\infty} = 40$ cm/s, 70cm/s and 100cm/s and solid fuel thicknesses of 0.82 cm and 1.74 cm. Notably, the solid fuel length herein is finite. The values expressed by solid symbols are ignition delays for $\bar{\tau} = 0.82$ cm, whereas those represented by hollow symbols are for $\bar{\tau} = 1.74$ cm. This figure reveals that the ignition delay time increases with the opposed flow velocity, because the thermal boundary layer is thinner in regime of higher opposed flow velocity, in which more produced fuel vapors are carried downstream, hindering the accumulation of fuel vapor near the solid fuel surface, increasing the formation time of the flammable mixture, delaying the ignition. However, at a fixed opposed flow velocity, the ignition delay falls as the opposed flow temperature increases, because a flow at higher temperature can heat the solid fuel more effectively, generating more fuel vapor, and forming the flammable mixture sooner, shortening the ignition delay time. Moreover, the ignition delay for $\bar{\tau} = 1.74$ cm is longer than that for $\bar{\tau} = 0.82$ cm at a fixed flow velocity and temperature. A thicker solid fuel has a greater thermal inertia (the ability of a material to conduct and store heat) and requires more energy to reach the ignition temperature, increasing the ignition delay. The experimental observations of Pan (1999) and Chen (1999) and the predictions of Wu et al. (2003) and Wu and Chen (2003) have confirmed these findings.

Figure 3.1.4 plots the ignition delay time as a function of the opposed flow temperature with and without the radiation effects and the solid fuel lengths are finite and infinite, respectively. The ignition delay times with radiation (cases a,b,e) are longer than that without radiation (cases c,d,f), which fact can be explained as follows. Figure 3.1.5 displays the distributions of heat fluxes along the solid fuel surface at the instant just before ignition ($\bar{t} = 13.72s$). q_{ex} and q_c are the external input radiant heat flux with a Gaussian distribution and the conductive heat flux from the gas, respectively. q_{gr} and q_{sr} represent the gas phase radiation feedback to the solid fuel and the radiation heat loss from the solid fuel to the ambient. The sum of total heat fluxes is the net heat flux on the surface of the solid fuel, q_{net}. A positive value means that the solid fuel gains energy from the gas phase and a negative value represents the loss of heat from the surface of the solid fuel. It shows that the magnitude of gas phase radiation changes insignificantly and can be negligible because the flame ignites in a high speed flow regime. Furthermore, this figure demonstrates that the net heat flux, q_{net}, near the origin is lower when the radiation effect is considered. The solid fuel must receive more energy for pyrolysis to produce fuel vapor, spending more time to form the flammable mixture. Hence, the ignition occurs more slowly with radiation. The inset in figure 3.1.5 plots the distributions of solid fuel temperature and the density contours just before ignition. It reveals that the solid fuel temperature is lower with radiation, reducing the magnitude of fuel vapor. Furthermore, the differences between the ignition delay time in the figure 3.1.4 increase with the opposed flow temperature (cases a,c or cases b,d) and decrease with the opposed flow velocity (cases e,f). The former result follows for the fact that q_{sr} is proportional to T_s^4. The solid fuel surface temperature is higher when it is immersed in a hotter flow, so the heat lost by radiation from the solid fuel surface to the surroundings is increased. The later result is because that the convection effect is more effective at higher flow velocity. In other words, the radiation is less important in the high velocity regime. Additionally, whether the solid fuel length is finite or infinite does not significantly influence the ignition delay (cases a,b or cases c,d). This is because the ignition delay time is dominated by the opposed flow velocity and temperature and the solid fuel thickness, but not the solid fuel length.

Figure 3.1.6 plots the pyrolysis front positions as a function of time at $\bar{\tau} = 0.82cm$, $\overline{T_i} = 333K$ and $\overline{u_\infty} = 70cm/s$. The pyrolysis front position is defined as the first upstream position of $\rho_s = 0.99$. The steady flame spread rate can be obtained from the slope of a best fit line that passes through the pyrolysis front positions. Computations are carried out by using a non-uniform mesh distribution. Most of the grid points are clustered around the external radiative heating region (x=0) and then they are expanded upstream and downstream. Hence, the flame displacement shows the stair-step pattern when the flame spreads far away from the origin. However, it does not alter the expected constant flame spread rate, indicated by that the straight line passes through these stair-step points. The steady flame spread rate at various opposed flow velocities and temperatures can also be determined by this way, and they are presented in the next figures.

Figures 3.1.7 and 3.1.8 present the flame spread rate versus the opposed flow temperature at three opposed flow velocities for solid fuel thicknesses of 0.82 cm and 1.74 cm, respectively. The symbols represent the data measured by Pan (1999), whereas the solid and dashed lines indicate the results simulated herein and the prediction of Wu et al. (2003), respectively. There are three computed results in each line. The conditions, such as the opposed flow velocity and temperature, used in the computations are all the same as those used in experiments. These two figures indicate that the flame spread rate increases with the opposed flow temperature at a fixed opposed flow velocity. The flame spread rate falls as the opposed flow velocity increases at a fixed opposed flow temperature. Furthermore, the flame spread rate of a thicker solid fuel is lower at a given opposed flow velocity and temperature. The phenomena described above can be explained in detail as follows.

Figure 3.1.9 depicts the temperature contours of the gas and solid phases and the velocity vector distributions at a fixed opposed flow velocity of $\bar{u}_\infty = 40 cm/s$ and opposed flow temperatures of 313K, 333K and 353K. As expected, a hotter opposed flow leads to a stronger flame. For example, the non-dimensional maximum flame temperatures are 5.286, 5.343 and 5.44 at opposed flow temperatures of 313K, 333K and 353K, respectively. The solid fuel receives more energy from the stronger flame, increasing the upstream pyrolysis length (and the preheat length) and increasing the intensity that shortens the formation time of flammable mixture ahead of the flame front. Therefore, the flame spread rate increases with the opposed flow temperature. Figure 3.1.10 display the heat flux distributions along the solid fuel surface at $\bar{t} = 25s$ under a fixed opposed flow velocity $\overline{u_\infty} = 40cm/s$ and the insets (a), (b) and (c) of this figure show the peak values of q_{net}, the sum of q_c , q_{gr} and q_{sr}, for the opposed flow temperature of 313K, 333K and 353K, respectively. The heat flux distributions are all similar for various opposed flow temperature but a comparison among the insets reveals that the magnitude of q_{net} increases with the opposed flow temperature. This result demonstrates that the solid phase absorbs more energy from the flame to pyrolyze the fuel into gaseous vapor, reducing the time to form flammable mixture and accelerating the flame spread. The predictions of Kumar et al. (2003a) and Wu and Chen (2004) confirm this result. Moreover, this figure shows that the magnitude of gas phase radiation changes insignificantly and can be negligible because the flame spreads in a high speed flow regime.

Figure 3.1.11 displays the temperature contours of gas and solid phases and the velocity vector distributions at various opposed flow velocities from 40 cm/s to 100 cm/s and a flow temperature fixed at 313K. The flame spread rate falls as the opposed flow velocity increases at a fixed flow temperature, because the flame stretching increases with the opposed flow velocity. The heat transferred from the flame front becomes less able to preheat the solid fuel and most of the fuel vapors generated from the pyrolysis zone are carried downstream. These factors result in a weaker flame and the corresponding flame spread rate becomes lower.

Figure 3.1.12 presents the temperature contours of gas and solid phases for a given opposed flow velocity of 40cm/s and temperature of

313K for solid fuel thicknesses of 0.82cm and 1.74cm. The flame spread rate declines as the solid fuel thickness increases at a given opposed flow velocity and temperature, because a thicker solid fuel has a greater thermal inertia that requires more energy to be heated to a temperature that supports pyrolysis, such more time is required to form the flammable mixture and the flame spread rate is reduced. This figure demonstrates that the flame and preheated area upstream of solid fuel are both larger when the solid fuel is thinner, which results were predicted by West et al. (1994) and Wu et al. (2003). Additionally, the flame spread rate varies with the solid fuel thickness at a fixed opposed flow velocity and temperature, but the thermal boundary layer and the maximum flame temperature are not significantly affected. This phenomenon has been verified by the experiments of Pan (1999) and Chen (1999), which also demonstrated that the thermal boundary layer and the maximum flame temperature are independent of the solid fuel thickness. Both results of the present work and Pan’s experiment (1999) show that the maximum reduction in flame spread rate is no more than 20% as fuel thickness increases from 0.82 cm to 1.74 cm. This indeed demonstrates the features of thermally thick fuel used in these two studies.

The predicted flame spread rates of the presented work are generally closer to Pan’s experimental measurements (1999) than the results simulated by Wu et al. (2003) because several factors such as finite length solid fuel, enclosure effect and both gas and solid radiations are considered in the present combustion model. Figure 3.1.13 displays the temperature contours of gas and solid phases for a given opposed flow velocity of 40cm/s and temperature of 313K with and without radiation effect. It reveals that the upstream preheated area of the solid fuel is shorter when the radiation is not neglected; suggesting that the heat loss from the solid fuel is increased, reducing its pyrolysis intensity. Figure 3.1.14 depicts the gas phase temperature contours over the solid fuel surface as determined by Pan’s experiment (1999) (figure 3.1.14(a)) and as predicted by present work (figure 3.1.14(b)) and Wu et al. (2003) (figure 3.1.14(c)), at $\bar{u}_\infty = 40cm/s$, $\bar{T}_i = 313K$ and $\bar{\tau} = 0.82cm$. The black portions represent solid fuel. The flame tail defined in this work is the area of the flame temperature contours, where no solid fuel is appeared under the flame. The solid fuel infinitely expands upstream and downstream and the flame tail continues to grow over the solid fuel surface as showed in Figure 3.1.14(c), whereas in Figures 3.1.14(a) and 3.1.14(b), the flame tail contract slightly over the solid fuel surface of finite length. The downstream solid fuel can not continually supply fuel vapor to form the flammable mixture when the flame spreads over the finite length solid fuel. This phenomenon reduces the overall flame temperature, decreasing the flame spread rate. Furthermore, the enclosure effect is included in this study. The enclosure effect confines the flow more parallel to the solid fuel surface and it influences on the flame spread behavior slightly. However, the enclosure effect becomes less important in the high speed flow regime and it is more pronounced for the three-dimensional configuration than for the two-dimensional one. The numerical study of Nakamura et al. (2002) also confirmed this result. Accordingly, these factors as mentioned above results in the predictions herein are similar to the experimental values. However, the discrepancies of the flame spread rate between the present model and experiment are still greater at low opposed flow regime. The reason may be attributed to the present study does not consider the three-dimensional effect, which may affects the flame behavior obviously, especially in the low speed flow regime.

3.2 Effect of opposed flow on flame spread over a finite-length PMMA slab in a two-dimensional wind tunnel

The aforementioned series of studies, such as those of Pan (1999), Wu et al. (2003) and the part 1 of present dissertation, concluded that the influence of opposed flow velocity on the flame spread behavior exceeds that of opposed flow temperature as flow velocity is increased further, and that the discrepancies between the predicted and measured results, especially in the low flow speed regime are due to the radiation effect. Moreover, numerous investigations, such as those of West et al. (1994), Rhatigan et al. (1998), Tizon et al. (1999) and Zhu and Gore (2005), demonstrated that the radiation effect becomes stronger as the flow speed declines. Therefore, this topic systematically investigates the effects of opposed flow velocity on the flame spread characteristics considering the radiation effect over a finite-length PMMA slab in a two-dimensional wind tunnel. The opposed flow velocities simulated herein are varied from 0 to 100cm/s, whereas the ones used by Pan (1999), Wu et al. (2003) and the part 1 of present dissertation are varied from 40 to 100cm/s. The entire process, from ignition to subsequent flame spread, is examined in detail. The effects of opposed flow temperature, solid fuel thickness and radiation heat loss at various flow velocities are also discussed.

Figure 3.2.1 plots the computed ignition delay time as a function of opposed flow velocity at a fixed opposed flow temperature of 313K with and without radiation in the gas and solid phases. The ignition delay time is defined herein as the instant at which the first appearance of the dimensional reaction rate reaches $10^{-4}\ g/cm^3s$. This figure reveals that the ignition delay time increases with the opposed flow velocity. This occurs because the temperature of the solid fuel increases to the pyrolysis temperature with greater difficulty in the faster flow due to the stronger convective cooling effect. In addition, most of the generated fuel vapors are carried downstream by the fast flow, extending the formation time of a flammable mixture adjacent to the solid fuel surface. Therefore, for these two reasons the ignition delay time is longer in the faster flow regime. Furthermore, in figure 3.2.1 the results with and without the effect of radiation are compared. The ignition delay with radiation is expected to be longer than that without radiation. The solid fuel requires longer time and more energy to reach the pyrolysis temperature in order to produce fuel vapors as heat is lost by radiation, these increasing the formation time of the flammable mixture and the ignition delay time as well. In the ignition stage radiant loss therefore dominates radiant heat absorption by the gas and the solid.

Figure 3.2.2 plots the flow velocity vector distributions and the non-dimensional temperature contours for the gas and solid phases at several opposed flow velocities at a fixed opposed flow temperature of 313K. Notably, both gas and solid phase radiations are considered. The left and right-hand sides of figure 3.2.2 depict the temperature contours for the gas and solid phases, respectively. Both fronts of temperature contours (gas and solid phase) along the solid fuel surface move further upstream (the upstream defined herein is the direction of inlet opposed flow) and then shift back to downstream as the opposed flow velocity continuously increases. Additionally, the flame size is reduced and the gas temperature contours are pushed toward the solid fuel surface as the opposed flow velocity increases. Also, the curvature of the apex of the temperature contours declines as the opposed flow velocity increases. In this figure, it can be found that some of the flames are further upstream than others. This is because the flame spread rate varies with the opposed flow velocity non-monotonically. The faster flame spread rate leads to the flame further upstream. These aforementioned phenomena will be discussed in detail later. Figure 3.2.3 plots the fuel and oxidizer mass fraction distributions that correspond to figure 3.2.2. The solid and dashed lines represent the fuel and oxidizer mass fraction distributions, respectively. Clearly, the fuel and oxidizer are premixed well at the flame front. The premixed flammable mixture plays the role of a source to support combustion enabling the flame can therefore sustain itself to spread upstream. This fact that there is premixing near the flame leading edge was first noted in the PhD thesis of DeRis (1968) and subsequently a detailed discussion was given by Wichman (1984). Behind the premixed region, the flame is a diffusion flame.

Figure 3.2.4 plots the predicted flame spread rate as a function of opposed flow velocity at a fixed opposed flow temperature of 313K with and without gas and solid phase radiation. The flame spread rate is determined by the motion of the pyrolysis front, which is defined as the first position of $\rho_s = 0.99$. The flame spread rate varies with the opposed flow velocity non-monotonically and two flame spread regimes are separated by the peak value in between. The peak occurs at a flow velocity of approximately 32 cm/s and the maximum change in flame spread rate is about 13.2%. In the first regime, $\bar{u}_\infty < 32cm/s$, where the flame spread rate increases with the opposed flow velocity. In the second regime, $\bar{u}_\infty > 32cm/s$, where the flame spread rate decreases as the opposed flow velocity increases, opposite to the trend in the first regime. In the first flame spread regime, the controlling mechanism of flame spread is oxygen transport. The higher speed opposed flow supplies more oxygen to the flame, to mix with the fuel vapor, shortening the formation time of the flammable mixture near the solid fuel surface, and thus strengthening the flame and accelerating the spread. However, as the opposed flow velocity increases into the second regime, the controlling mechanism of the flame spread is chemical kinetics. As the opposed flow velocity increases, most of the fuel vapors are carried downstream. The gas residence time decreases and the chemical reaction does not have sufficient time to proceed to completion, reducing the ratio of the residence time of the mixture to the chemical time (i.e. the Damköhler number). These phenomena mentioned above have been confirmed by the prior study of DeRis (1968). In addition, the increase in the stretch effect reduces the thickness of the flame, as shown in figure 3.2.2, and it is more difficult for the forward heat transfer from the flame to preheat the solid fuel. Consequently, the flame becomes weaker, such that the spread rate is lower in the regime of high flow velocity.

The opposed flow velocity is used as a parameter to study the flame spread behavior. The radiation to conduction parameter ($1/N_\infty$) and Damköhler number (Da) will be changed by the variation of opposed flow velocity. The definitions of $1/N_\infty$ and Da are $\overline{\sigma}\overline{T_\infty}^3\overline{\alpha^*}/\overline{k^*}\overline{V_r}$ and $\overline{B}\overline{\rho^*}\overline{\delta}/\overline{V_r}$, respectively. Table 6 lists the values of flame-spread rate ($\overline{V_f}$), $1/N_\infty$ and Da variation with opposed flow velocity. It can be found that the values of both $1/N_\infty$ and Da are reduced with an increase of opposed flow velocity. The increase in flame spread rate with increased opposed flow velocity is attributed to greater heat and/or oxygen transport as the flame is pressed closer to the fuel surface due to thinning boundary layers and enhanced mixing of fuel and oxidizer. At opposed flow velocity greater than 32cm/s, the flame spread rate falls gradually toward blow-off extinction. This decrease in flame spread rate is attributed to Damköhler number effects which shorter residence times for chemical reaction to occur actually limit the flame spread process; further thinning of the oxygen concentration and thermal boundary layers no longer acts to enhance the mixing and subsequent chemical reaction rate. In the other hand, the radiation effect on the flame spread behavior becomes insignificant when the opposed flow velocity increases further. In higher speed flow regime, the conduction and convection are the dominant mechanisms. Several numerical and experimental studies, such as those of Lastrina et al. (1971), Fernandez-Pello and Hirano (1983), Olson (1991), Wichman (1992), Tizon et al. (1999) and Fujita et al. (2002), have found this qualitative trend of the flame spread rate mentioned above. Figure 3.2.4 reveals that the flame spread rates with radiation are all lower than those without radiation. The heat loss by radiation weakens the flame and reduces the spread rate as well. Additionally, the peak value of flame spread rate occurs at an opposed flow velocity of approximately 32 cm/s. The parameter used in the present study is the opposed flow velocity and the opposed flow temperature and solid fuel thickness are fixed at the constant values. Therefore, the peak value of flame spread rate may be changed at other value of opposed flow velocity when the opposed flow temperature or solid fuel thickness are changed.

Figure 3.2.5 plots the heat flux magnitudes of q_{gr} and q_{sr} under various opposed flow velocities at a fixed opposed flow temperature of 313K. The heat fluxes, q_{gr} and q_{sr}, represent the gas phase radiation feedback to the solid fuel and the heat loss by radiation from the solid fuel to the ambient, respectively. The comparison of q_{gr} and q_{sr} demonstrates that the magnitude of the gas phase radiation is relatively much smaller, because the heat transfer mechanisms associated with flame spreading in a fast flow are dominated by conduction and convection. In other words, the maximum absolute values of q_{gr} and q_{sr} are 0.0499 and 0.812, respectively. Hence it can be found that $|q_{gr}|/|q_{sr}| << 1$. Accordingly, the apparent radiation heat transfer herein is preferentially only from the solid fuel to the ambient. Since q_{sr} is proportional to T_s^4 and the maximum solid fuel temperature herein is defined as the burnout temperature, 668K, the magnitude of q_{sr} is almost invariant throughout the simulated flow speed regime.

A recirculation flow just ahead of the flame front is observed, and its intensity increases with the opposed flow velocity, as illustrated in figure 3.2.6. This figure displays the temperature contours of the gas phase and the streamline distributions at a fixed opposed flow temperature of 313K for the three opposed flow velocities of 7cm/s, 32 cm/s and 100cm/s. The presence of the recirculation flow enhances the mixing of fuel vapor and the oxidizer. Additionally, the flow can also carry some heat upstream from the flame and simultaneously brings some of the cold air from upstream into the flame. These two mechanisms are competing with each other. As the flow velocity continues to increase, the latter effect outweighs the former one, indicating that the cooling effect is prominent. This phenomenon weakens the flame and reduces the corresponding spread rate. The recirculation region has been numerically confirmed by the prior researches, such as Whichman (1992) and Higuera et al. (1997).

Figure 3.2.7 plots the preheat lengths versus opposed flow velocity at a fixed opposed flow temperature of 313K with and without radiations. The preheat length herein is defined as the distance between the non-dimensional temperature contours of 1.1 and 2.1 along the solid fuel surface, as shown in the inset of figure 3.2.7. The maximum change in preheat length is about 15%. The preheat zone becomes narrower as the opposed flow velocity increases and the dependence on opposed flow velocity becomes stronger as the velocity declines. A larger preheat length corresponds to a shorter required time for solid fuel to raise its temperature to the pyrolysis temperature, thereby increasing pyrolysis intensity. However, an excessive preheat length causes the dispersion of heat across a rather wide region, slowing the flame spread, as displayed in figures 3.2.4 and 3.2.7. These two figures demonstrate that the preheat length is larger in the region of lower flow velocity, but the corresponding flame spread rate is not higher. As the opposed flow velocity increases further, the convective cooling effect becomes stronger and the forward heat transfer from the flame to preheat the solid fuel becomes more difficult, shortening the preheat length. Furthermore, the preheat length with radiation is smaller than that without radiation because heat is lost by radiation, reducing the total heat received by the solid fuel.

Figure 3.2.8 plots the maximum flame temperature in the gas phase as a function of opposed flow velocity at a fixed opposed flow temperature of 313K with and without radiation. The flame temperature initially increases sharply and then declines slightly as the opposed flow velocity increases, suggesting that the dependence on opposed flow velocity is stronger at lower velocity. According to the phenomena of flame spread mentioned previously, the variation of the flame temperature can also be divided into two regimes. In the first regime, prior to the flame spread rate maximum of figure 3.2.4 where the opposed flow velocity is below 32cm/s, the flame becomes stronger and the flame spread rate increases with the flow velocity, resulting in an increase of the flame temperature. In the second regime, where the opposed flow velocity exceeds 32 cm/s, the flame spread rate decreases as the opposed flow velocity increases, indicating that a weaker flame spreads in this flow velocity regime and, therefore, the flame temperature is reduced, but its variation is inconspicuous. This result demonstrates that the effect of opposed flow velocity on the flame temperature in the high speed flow regime is not very significant, but it pushes the flame toward the solid fuel surface, allowing it to be more or less parallel to the surface, as shown in figure 3.2.2. Pan (1999) and Chen (1999) also experimentally observed this phenomenon. Comparing the flame temperatures measured in these two experimental works (not shown here) reveals that the temperatures predicted herein are higher. This difference may possibly be attributed to the side heat loss from the flame to the side walls of the wind tunnel in the experiment. The wind tunnel utilized in the experimental test is three-dimensional, whereas the flame spreads in a two-dimensional wind tunnel in the present simulation. Note from figure 3.2.8 that radiation only slightly affects the flame temperature because the magnitudes of the gas and solid phase radiation is small compared with the heat conducted in the gas phase.

Figure 3.2.9 plots the total heat fluxes received by the solid fuel against the opposed flow velocity at a fixed opposed flow temperature of 313K with and without radiation. The maximum change in heat flux received by solid fuel is about 12%. From previous figure, the variation of maximum flame temperature is quite insignificant, indicating that the solid-phase radiation makes more contribution in total heat flux than that of gas-phase one. The dependence of the heat supplied to the solid fuel on the opposed flow velocity can also be divided into two regimes, which are consistent with the flame spread predictions described previously in figures 3.2.4 and 3.2.8. Since the heat supplied to the solid fuel is controlled mainly by the flame temperature, the heat flux received by the solid fuel in the first regime increases rapidly due to the rapid rise of the flame temperature. However, in the second regime, the flame temperature is reduced as the flow velocity increases, reducing the heat supplied to the solid fuel. The change of heat flux in a fast flow is insignificant because the variation in the flame temperature is slight.

The effects of the opposed flow temperature and solid fuel thickness on the flame spread characteristics are also investigated in this work. Figure 3.2.10 plots the ignition delay as a function of the opposed flow temperature at three opposed flow velocities of 10cm/s, 40cm/s and 100cm/s and two solid fuel thicknesses of 0.82cm and 1.74cm. Notably, both gas and solid phase radiation is considered. Figure 3.2.10 reveals that the ignition delay time decreases as the opposed flow temperature increases at a fixed opposed flow velocity regardless of whether the solid fuel thickness is 0.82cm or 1.74cm. This is because that the hotter opposed flow temperature preheats the solid fuel more effectively, reducing the quantity of heat needed to raise the solid surface temperature to its pyrolysis temperature. The time required to pyrolyze the fuel vapors mixed with air to form the flammable mixture is reduced. Consequently, the flame can be ignited more quickly. Furthermore, this figure shows that the variation in the ignition delay becomes negligible as the opposed flow velocity is increased further, suggesting that the effect of the opposed flow temperature on flame ignition becomes weaker in the faster flows. Restated, the effect of the opposed flow velocity is more important than that of the opposed flow temperature, which fact was confirmed by Pan (1999), Wu et al. (2003). Additionally, the ignition delay times with a solid fuel thickness of 1.74cm are all expected to be longer than those with a solid fuel thickness of 0.82cm. A thicker solid fuel has a greater thermal inertia which is defined as the ability of a material to conduct and store heat (Di Blasi, 1995); hence the solid fuel requires more time to receive the heat required for it to reach the pyrolysis temperature, these increasing the ignition delay time.

Figure 3.2.11 plots the flame spread rate versus the opposed flow temperature at three opposed flow velocities of 10cm/s, 40cm/s and 100cm/s and two solid fuel thicknesses of 0.82cm and 1.74cm. As expected, a hotter opposed flow leads to a stronger flame. For example, the non-dimensional maximum flame temperatures at the opposed flow temperatures of 313K, 333K and 353K are 5.286, 5.343 and 5.44, respectively, at a fixed opposed flow velocity of 40cm/s. The enhanced pyrolysis intensity shortens the formation time of the flammable mixture ahead of the flame front. Hence, the flame spread rate increases with the flow temperature at a fixed opposed flow velocity. Note that the flame spread rate at an opposed flow velocity of 10cm/s and a temperature of 313K is the lowest among all opposed flow velocities. However, the variation of the flame spread rate at an opposed flow velocity of 10cm/s is steepen than those at 40 and 100 cm/s as the opposed flow temperature increases, revealing that the influence of the upstream gas temperature on the flame spread rate is stronger at the lower flow speeds. Moreover, a comparison between two solid fuel thicknesses shows that the flame spread rates over the thicker solid fuel sample are all slower than those of the thinner fuel. Di Blasi (1995) and Di Blasi and Wichman (1995) also obtained this finding. As mentioned previously, this result is attributed to the fact that a thicker solid fuel has a greater thermal inertia, such that increasing the temperature of the fuel is more difficult. Accordingly, the solid fuel takes longer to form the flammable mixture near the solid fuel surface, reducing the flame spread rate.

3.3 The investigation of downward flame spread over a finite-length PMMA slab in a wind tunnel by using the unsteady three-dimensional combustion model

In the previous topics, the greater discrepancies of results between the simulation and the experiment still exist in low opposed flow regime. This may be attributed to the 3D effect is not included in the combustion model. Therefore, this topic utilizes the unsteady three-dimensional combustion model to study the influence of 3D effect on the flame behavior over a finite-length PMMA slab. The present three-dimensional unsteady combustion model is basically developed from the original two-dimensional one of part 1 of present work. In this problem, the governing equations and the assumptions are basically the same as these given in the previous description of chapter 2, except that the model is developed from two-dimension to three-dimension. Therefore, the mathematical model and the assumptions are not represented here for brevity. The non-dimensional gas and solid governing equations are listed in Table 7. The discrepancies between the part 1 of present dissertation and present work are listed in the Table 8.

Figure 3.3.1 presents the configuration of three-dimensional ignition over a vertically oriented PMMA slab in a mixed convective environment. The dimensions of wind tunnel and the solid fuel plates used in the present simulation are all the same as those of Pan's experiment (1999). Computations are carried out using a non-uniform mesh distribution as shown in the figure 3.3.2. The tests of the independence of the grid-size were conducted in advance and the results are shown in Table 9. According to the grid-independence test, a non-dimensional time step of $\Delta t = 10$ (equivalent to a real time of 0.02 s) and non-uniform grid dimensions of $290 \times 95 \times 50$ were found to optimize the balance among resolution, computational time and memory space requirements. The prior numerous studies, such as those of Mell and Kashiwagi (2000), Nakamura et al. (2002) and Shih and T'ien (2003), indicated that the 3D effect is dominated by the flow velocity. Therefore, the parametric study herein is conducted by changing the opposed flow velocity and its range is the same as used in the experiment of Pan (1999), to enable the results to be compared fairly with the prior predictions of Wu et al. (2003) and the part 1 of present dissertation. Remind that the solid fuel in present study is assumed to be homogeneous that its compositions are uniform and its thickness is remained constant by assuming the flame spreads relatively fast enough that the fuel surface near the flame base remains approximately flat. Notably, both the computation domain utilized in these combustion models mentioned above are two-dimensional, whereas the one utilized in the present model is three-dimensional. The ambient oxygen concentration in the present model is fixed at 0.233.

Figure 3.3.3 displays the three-dimensional flame spread over the solid fuel surface. The left hand side is the camera image observed by the Pan’s experiment (1999) and the right hand side demonstrates the simulated result in the present study. The opposed flow velocity and temperature are 40cm/s and 313K and the solid fuel thickness is 0.82cm. The simulated flame profile is highly similar to the one of experiment. It can be found that both the flame tails of experimental observation and the simulation contract over the solid fuel surface. This is because the asbestos plates locates behind the origin ($x = y = z = 0$) and it does not continuously provide the fuel vapor to form the flammable mixture. This factor increases the formation time of flammable mixture and decreases the intensity of chemical reaction as well. Hence, the overall flame temperature is reduced, declining the downstream flame size. However, the flame tail of Wu et al. (2003) still grows (not shown here) because the solid fuel expends upstream and downstream infinite and the flame spreads in an open atmosphere. Furthermore, in this figure, it can be seem that the opposed flow is confined by the tunnel walls and the flame is pushed by the flow toward the solid fuel surface slightly.

Figure 3.3.4 displays the time history of the three-dimensional flame profiles and the flow velocity vector distributions from ignition to subsequent flame spread for the opposed flow velocity of 40cm/s and temperature of 313K and the solid fuel thickness of 0.82cm. The time history of ignition and subsequent flame spread is similar to that mentioned in the part 1 of present dissertation. The solid fuel receives the external heat flux to raise its temperature gradually and some part of the heat received by the solid fuel also heats the gas phase simultaneously, as shown by figure 3.3.4(a) and figure 3.3.4(b). The flame is ignited as gas phase temperature raise high enough, resulting the drastic chemical reaction and thermal expansion, as demonstrated in figure 3.3.4(c). Thereafter, the flame starts to spread downward and spreads with steady rate after several seconds, as shown in figure 3.3.4(d).

Figure 3.3.5 displays the ignition delay time as a function of opposed flow velocity for 2D and 3D problems, respectively. The opposed flow temperature and solid fuel thickness are fixed at 313K and 0.82cm. As mentioned previously, the ignition delay time increases with an increase of opposed flow velocity. However, in this figure, it can be found that the ignition delay times of 3D problem are greater than ones of 2D problem and the discrepancies of ignition delay time between the 2D and 3D problems are decrease with an increase of opposed flow velocity. The difference of ignition delay time between 2D and 3D problems for opposed flow velocity of 40cm/s is 0.64s, whereas the one for opposed flow velocity of 100cm/s is 0.11s. In the lower opposed flow regime of 3D problem, the fuel vapor is carried downstream by the convection but some of the fuel vapor is diffused to the lateral sides of wind tunnel, hindering the accumulation of fuel vapor near the solid fuel surface, increasing the formation time of the flammable mixture, resulting the greater difference of ignition delay time between the 2D and 3D problems. However, in the higher opposed flow regime of 3D problem, the fuel vapor transferred to the lateral sides of wind tunnel by the diffusion becomes difficult. In other words, most of produced fuel vapor is carried downstream by convection. This phenomenon is similar to that of 2D problem. Therefore, the influence of 3D effect on ignition delay time is reduced when the flame is ignited under the high speed flow regime.

Figure 3.3.6 presents the steady flame spread rate versus the opposed flow velocity at a fixed opposed flow temperature of 313K and a solid fuel thickness of 0.82 cm. The steady flame spread rate herein is determined by the slope of a best fit line that passes through the pyrolysis front position which is defined as the first upstream position of $\rho_s = 0.99$. The solid, dash and dash-dot lines in this figure indicate the simulated results of the present work, the part 1 of present dissertation and Wu et al. (2003), respectively. There are three results in each line. The circular symbols separately represent the data measured by Pan (1999). Notably, the conditions such as the opposed flow velocity and temperature and the solid fuel thickness used in these computations are all the same as those used in the experiment. This figure indicates that all the flame spread rates of experimental measurement and simulated results fall as the opposed flow velocity increases. Comparing with the results between the experiment and predictions in the figure 3.3.6, the results of present work are closer to those of experiment, especially in lower speed flow regime. In the investigation of part 1 of present dissertation, the enclosure effect and both gas and solid phase radiations are added to the combustion model. The enclosure effect confines the flow more parallel to the solid fuel surface and enhances the oxygen supply for combustion, increasing the flame spread rate. Additionally, the radiation effect plays a role of heat loss from the solid fuel and reduces the pyrolysis intensity, decreasing the flame spread rate. These two effects are competing with each other. Obviously, the influence of enclosure on the flame spread rate overcomes the one of radiation in this flow speed regime. Hence, the flame spread rate of part 1 of present dissertation increases compared with the one of Wu et al. (2003).

In the present work, the 3D effect is considered in the combustion model. The 3D effect includes two mechanisms, such as the oxygen diffusion from the side walls of tunnel to the flame and the heat loss from the flame to the side walls of tunnel. The former one enhances the chemical reaction and the flame intensity as well, whereas the latter one results in a lower flame temperature and reduces the corresponding spread rate. Figure 3.3.7 displays the temperature contours of gas phase and flow velocity vector distributions at a fixed opposed flow velocity of 40cm/s and temperature of 313K and solid fuel thickness of 0.82cm for 2D and 3D problems, respectively. In this figure, it can be seem that the flame profiles are almost the same between the 2D and 3D problems but the flame front for 3D problem is shift back to downstream slightly due to the slower flame spread rate, as shown in figure 3.3.6. Figures 3.3.8 illustrate the flame characteristics on X-Z plane for opposed flow velocity of 40cm/s and temperature of 313K and solid fuel thickness of 0.82cm at t = 25s. Figures 3.3.9 and 3.3.10 separately display the flame characteristics on Y-Z plane for opposed flow velocity of 40cm/s and 100cm/s at t = 25s and the opposed flow temperature and solid fuel thickness are fixed at 313K and 0.82cm. The right half displays the gas phase temperature contours and flow velocity vector distributions, whereas the left half presents the fuel and oxidizer mass fractions, respectively. In the figure 3.3.8, it can be seem that the solid fuel pyrolyze the fuel vapor mixing the air to form the flammable mixture in the flame front region. The ambient oxygen concentration is fixed at 0.233 in the present study and the oxygen supply rate from side to the flame center by diffusion will be decreased with an increase of flow convective velocity, as shown in figures 3.3.9 and 3.3.10. Comparing with the magnitude of oxygen supply by convection, the oxygen side diffusion can be neglected due to the flame spread in high speed flow regime. Therefore, the influence of oxygen side diffusion on the flame spread rate is insignificant in the present study. This phenomenon mentioned above has been confirmed by the prior studies of Mell and Kashiwagi (2000), and Shih and T’ien (2003). In the other hand, the cold tunnel walls conduct heat away from the flame which introduces the heat loss. In these figures, it can be seem that the higher gas phase temperature contours are clustered at the flame leading edge and then drop gradually from the flame center to the side walls. Moreover, it can also be pointed out that the influences of lateral walls are more significant than that of the top wall. For example, in the figure 3.3.9, the distance (0.85cm) from the origin to the joint of the isothermal of 1.17 on the z axis is shorter than that (1.02cm) on the y axis. It indicates that the heat loss from the flame to the lateral walls of wind tunnel is greater than that to the top wall of wind tunnel because the distance (5cm) between the origin and lateral wall of wind tunnel is shorter than one (10cm) between the origin and top wall of wind tunnel. Summarized the factors discussed above, the overall 3D effect on the flame spread behavior in this work is to decrease the flame spread rate and it can be seem that the flame spread rate of present work compared with the results of part 1 of present dissertation is slightly reduced from the figure 3.3.6. Hence, the flame spread rates predicted in the present work are closer to the ones measured by the experiment of Pan (1999), especially in lower speed flow regime.

Chapter 4

Conclusions

This work numerically investigates the flame ignition and subsequent flame spread characteristics over a finite-length PMMA slab under mixed convection conditions in a wind tunnel using an unsteady combustion model. The modified combustion model of present study, included finite-length solid fuel, enclosure effect, gas and solid phase radiations and 3D effect, is expected to be more completeness and accuracy to predict the ignition delay time and flame spread rate. The previous studies mostly are addressed either thermally thick or thin materials, whereas the present work is emphasized on intermediate-thickness materials.

The first part of this study utilizes an unsteady combustion model, with opposed flow velocity and temperature and solid fuel thickness as parameters, to investigate the effects of these factors on the ignition delay and the subsequent downward flame spread over a PMMA slab of finite length under mixed convection conditions in a two-dimensional wind tunnel. The results obtained by simulation herein are compared with the corresponding predictions and experimental measurements. The ignition delay time increases as the opposed flow velocity or the solid fuel thickness increases and the flow temperature falls. Additionally, the steady flame spread rate increases as the opposed flow velocity or the solid fuel thickness declines and the flow temperature increases. The gas phase radiation effect can be neglected because the flame spreads in the high speed flow regime. On the other hand, the solid phase radiation affects the ignition delay time and flame spread rate significantly. It increases the ignition delay time and reduces the flame spread rate. Moreover, the downstream flame size grows over an infinite length fuel plate, whereas that herein contracts slightly over a finite length fuel plate, resulting in the lower flame spread rate. The factors, such as radiation and finite fuel length mentioned above, reduce the flame spread rate and thus mitigate the discrepancies between the predicted results of present work and the corresponding experimental measurements. However, the discrepancies remained in the low flow velocity regime, because the three-dimensional effect is neglected in the present two-dimensional model. Also, the enclosure effect is insignificant in the high flow velocity regime and in the two-dimensional model.

The second part of this study utilizes an unsteady combustion model with variable opposed flow velocity as parameters to investigate the flame ignition and subsequent downward flame spread over a finite-length PMMA slab with mixed convection conditions in a two-dimensional wind tunnel. The gas and solid phase temperatures, preheat length of solid fuel and the heat flux received by the solid fuel are used to examine flame ignition and spread characteristics. The numerical results show that the ignition delay time increases with the opposed flow velocity and it increases when radiation is considered. Additionally, the flame spread behaviors can be divided into two regimes based on the opposed flow velocity: one is the oxygen transport control regime for $\bar{u}_{\infty} < 32 cm/s$ and the other one is the chemical kinetic control regime $\bar{u}_{\infty} > 32 cm/s$. The steady flame spread rate firstly increases and then declines as the opposed flow velocity is increased continuously. Furthermore, the results demonstrate that radiation weakens the flame and always reduces the corresponding spread rate. When compared with the radiation heat loss from the solid to the ambient, the gas phase radiation feedback is insignificant and can be neglected. This work also discusses the influences of the opposed flow temperature and solid fuel thickness on the flame spread behavior. The predictions indicate that the hotter opposed flow temperature facilitates ignition and enhances the flame strength as defined by an increase in the corresponding spread rate. The ignition delay time becomes longer and the flame spread rate is reduced as the solid fuel thickness is increased. The comparison of ignition delay time and flame spread rate between several opposed flow velocities and temperatures demonstrates that the influence of the opposed flow temperature on the flame becomes inconspicuous as the opposed flow velocity is increased further. All of these results should be of assistance and guidance to the development of the models that seek to incorporate additional physical processes.

The third part of this study utilizes a three-dimensional unsteady combustion model with opposed flow velocity as parameters to investigate the influences of 3D effect on the ignition and subsequent downward flame spread over a finite-length PMMA slab under mixed convection conditions in the wind tunnel. The results obtained by simulation herein are compared with the corresponding experimental measurements of Pan (1999) and predictions of Wu et al. (2003) and the part 1 of present dissertation. The simulated flame profile in this part is similar to that observed by the experiment. The ignition delay time increases with an increase of opposed flow velocity. However, the ignition delay times of 3D problem are greater than ones of 2D problem and the discrepancies of ignition delay time between the 2D and 3D problems are decrease with an increase of opposed flow velocity. This is because the fuel vapor transferred to the lateral sides of wind tunnel by the diffusion becomes difficult when the flame is ignited under a high speed flow regime. The simulated results indicate that the flame spread rate decreases with an increase of opposed flow velocity. The flame is stretched by the high speed flow and most of the fuel vapors are carried downstream, reducing the intensity of chemical reaction and the strength of flame as well. Hence, the corresponding flame spread rate is decreased with opposed flow velocity. A comparison is made between the earlier experiment and simulations. The results indicate that the predicted values of present work are similar to the ones of experiment, especially in the lower speed flow regime. This is because the 3D effect is added in the present combustion model. The 3D effect has two mechanisms to influence the flame behaviors. One is the oxygen side diffusion and the other one is the heat losses to the side walls. The simulated results of present work demonstrate that the former effect influences the flame spread insignificant because the flame spreads under a high convective flow, whereas the latter one reduces the flame temperature slightly as well as the flame spread rate. Therefore, the overall 3D effect on the flame behaviors in the present study is to reduce the spread rate of flame. Additionally, the simulated results show that the influence of lateral walls of wind tunnel are greater than that of top wall of wind tunnel due to the shorter distance between the flame and lateral walls of wind tunnel.

References

Aynai, M. B., Esfahani, J. A. and Mehrabian, R., Downward Flame Spread over PMMA Sheets in Quiescent Air: Experimental and Theoretical Studies, *Fire Safety Journal*, **41**, 164 (2006).

Bhattacharjee, S. and Grosshandler, W., Effect of Radiative Heat Transfer on Combustion Chamber Flows, *Combustion and Flame*, **77**, 347 (1989)

Bhattacharjee, S. and Altenkirch, R. A., The Effect of Radiation on Flame Spread in a Quiescent, Microgravity Environment, *Combustion and Flame*, **84**, 160 (1991).

Bhattacharjee, S., King, M., Takahashi, S., Nagumo, T. and Wakai, K., Downward Flame Spread over Poly(Methyl)Methacrylate, *Proceedings of the Combustion Institute*, **28**, 2891 (2000).

Chang, W. K., Chen, C. H. and Liou, T. M., Numerical Study for Downward Flame Spread over a Finite-length PMMA with Radiation Effect, Accepted by *International Journal of Transport Phenomena*, in press (2007).

Chen, C. H. and Cheng, M. C., Gas Phase Radiative Effects on Downward Flame Spread in Low Gravity, *Combustion Science and Technology*, **97**, 63 (1994).

Chen, R. J., Experimental Analyses of Flame Spread Behavior over Solid Fuel Under Suddenly Opposed Flow, MS thesis, National Tsing Hua University, Hsinchu, Taiwan, R.O.C. (1999).

Delichatsios, M. A., Exact Solution for the Rate of Creeping Flame Spread over Thermally Thin Materials, *Combustion Science and Technology*, **44**, 257 (1986).

DeRis, J. N., The Spread of a Diffusion Flame over a Combustible Surface, Ph. D. Thesis, Harvard University (1968).

Di Blasi, C., Influences of Sample Thickness on The Early Transient Stages of Concurrent Flame Spread and Solid Burning, *Fire Safety Journal*, **25**, 287

(1995a).

Di Blasi, C., Predictions of Wind-Opposed Flame Spread Rates and Energy Feedback Analysis for Charring Solids in a Microgravity Environment, *Combustion and Flame*, **100**, 332 (1995b).

Di Blasi, C. and Wichman, I. S., Effect of Solid-Phase Properties on Flames Spreading over Composite Materials, *Combustion and Flame*, **102**, 229 (1995).

Fernandez-Pello, A. C. and Hirano, S. T. Controlling Mechanisms of Flame Spread, *Combustion Science and Technology*, **32**, 1 (1982).

Ferkul, P. V. and T'ien, J. S., A Model of Low-speed Concurrent Flow Flame Spread over a Thin Fuel, *Combustion Science and Technology*, **99**, 345 (1994).

Fujita, O., Takahashi, J. and Ito, K., Experimental Study on Radiative Ignition of a Paper Sheet in Microgravity, *Proceedings of the combustion Institute*, **28**, 2761 (2000).

Fujita, O., Nishizawa, K. and Ito, K., Effect of Low External Flow on Flame Spread over Polyethylene Insulated Wire in Microgravity, *Proceedings of the combustion Institute*, **29**, 2545 (2002).

Goody, R. M., *Atmospheric Radiation I, Theoretical Basis*, Clarendon Press, Oxford (1964).

Grosshandler, W. L., Radiative Heat Transfer in Nonhomogeneous Gases: A Simplified Approach, *Journal of Heat and Mass Transfer*, **23**, 1447 (1980).

Grosshandler, W. L., RADCAL: a Narrow-Band Model for Radiation Calculations in a Combustion Environment, *NIST Technical Note 1402* (1993).

Higuera, F. J., Linan, A. and Iglesias, I., Effects of Boundary Layer Displacement and Separation on Opposed-Flow spread, *Combustion Theory and Modeling*,

1, 65 (1997).

Ito, A., Kudo, Y. and Oyama, H., Propagation and Extinction Mechanisms of Opposed-flow Flame Spread over PMMA for Different Sample Orientations, *Combustion and Flame*, **142**, 428 (2005).

Jiang, X. and Fan, Weicheng., Numerical Prediction of Flame Spread Over Solid Combustibles in a Microgravity Environment, *Fire Safety Journal*, **24**, 279 (1995).

Kumar, A., Shih, H. Y. and T'ien, J. S., A Comparison of Extinction Limits and Spreading Rates in Opposed and Concurrent Spreading Flames over Thin Solids, *Combustion and. Flame*, **132**, 667 (2003a).

Kumar, A., Tolejko, K. and T'ien, J. S., A Computation Study on Flame Radiation-Surface Interaction in Flame Spread over Thin Solid-Fuel, *The 6th ASME-JSME Thermal Engineering Joint Conference* (2003b).

Lin, P. H., and Chen, C. H., Numerical Analyses for Radiative Autoignition and Transition to Flame Spread over a Vertically Oriented Solid Fuel in a Gravitational Field, *Combustion Science and Technology*, **151**, 157 (2000).

Lin, T. H. and Chen, C. H., Influence of Two-Dimensional Gas Phase Radiation on Downward Flame Spread, *Combustion Science and Technology*, **141**, 83 (1999).

Ludwig, C. B., Malkmus, W., Reardon, J. E. and Thompson, J. A., *Handbook of Infrared Radiation from Combustion Gases*, NASA SP-3080 (1973).

Malkmus, W., Infrared Emissivity of Carbon Dioxide (4.3um band), *Journal of the Optical Society of America*, **53**, 951 (1963).

Mell, W. E. and Kashiwagi, T. (2000) Effects of Finite Sample Width on Transition and Flame Spread in Microgravity, *Proceedings of the Combustion Institute*, **28**, 2785.

Nakabe, K., McGrattan, K. B., Kashiwagi, T., Baum, H. R., Yamashita, H. and

Kushida, G., Ignition and Transition to Flame Spread over a Thermally Thin Cellulosic Sheet in a Microgravity Environment, *Combustion and Flame*, **98**, 361 (1994).

Nakamura, Y., Kashiwagi, T., Mcgrattan, K. B. and Baum, H. R., Enclosure Effects on Flame Spread over Solid Fuels in Microgravity, *Combustion and Flame*, **130**, 307 (2002).

Olson, S. L., Mechanisms of Microgravity Flame Spread Over a Thin Solid Fuel: Oxygen and Opposed Flow Effects, *Combustion Science and Technogy*, **76**, 233 (1991).

Olson, S. L., Kashiwagi, T., Fujita, O., Kikuchi, M. and Ito, K., Experimental Observations of Spot Radiative Ignition and Subsequent Three-Dimensional Flame Spread over Thin Cellulose Fuels, *Combustion and Flame*, **125**, 852 (2001).

Pan, I. J., Experimental Analyses of Flame Spread Behavior over Solid Fuel Under Opposed Flow, MS thesis, National Tsing Hua University, Hsinchu, Taiwan, R. O. C. (1999).

Patankar, S. V., *Numerical Heat Transfer and Fluid Flow*, New York, McGraw-Hill (1980).

Ratzell, A. C. III and Howell, J. R., Two-dimensional Radiation in Absorbing-emitting Media using the P-N Approximation, *ASME Journal of Heat Transfer*, **105**, 333 (1983).

Rhatigan, J. L., Bedir, H. and T'ien J. S., Gas-Phase Radiative Effects on the Burning and Extinction of a Solid Fuel, *Combustion and Flame*, **112**, 231 (1998).

Son, Y. and Ronney, P. D., Radiation-driven Flame Spread over Thermally Thick Fuels in Quiescent Microgravity Environment, *Proceedings of the Combustion Institute*, **29**, 2587 (2002).

Shih H. Y. and T'ien J. S., Modeling Wall Influence on Solid-Fuel Flame Spread in A flow Tunnel, *AIAA*, 97-0236 (1997).

Shih H. Y. and T'ien J. S.,. Modeling Concurrent Flame Spread over a Thin Solid in a Low-speed Flow Tunnel, *Proceedings of the Combustion Institute*, **28**, 2777 (2000).

Shih, H. Y. and T'ien J. S., A Three-dimensional Model of Steady Flame Spread over a Thin Solid in Low-speed Concurrent Flows, *Combustion Theory and Modeling*, **7**, 677 (2003).

Siegel, R. and Howell, J. R., *Thermal Radiation Heat Transfer*, Washington (1992).

Suzuki, M., Dobashi, R. and Hirano, T., Behavior of Fires Spreading Downward over Thick Paper, Twenty-Fifth Symposium (International) on Combustion, *The Combustion Institute*, 1439 (1994).

Takahashi, S., Nagumo, T., Wakai, K. and Bhattacharjee, S., Effect of Ambient Condition on Flame Spread over a Thin PMMA Sheet, *JSME International Journal Series B-Fluids and Thermal Engineering*, **43**, 556 (2000).

Takahashi, S., Kondou, M., Wakai, K. and Bhattacharjee, S., Effect of Radiation on Flame Spread over a Thin PMMA Sheet in Microgravity, *Proceedings of the Combustion Institute*, **29**, 2579 (2002).

Tizon, J. M., Salva, J. J. and Linan, A., Wind-Aided Flame Spread Under Oblique Forced Flow, *Combustion and Flame*, **119**, 41 (1999).

Turns, S. R., *An introduction to combustion concepts and applications*, McGraw-Hill Inc., (1996).

West, J., Bhattacharjee, S. and Altenkirch, R. A., Surface Radiation Effects on Flame Spread over Thermally Thick Fuels in an Opposing Flow, *Transactions of the ASME*, **116**, 646 (1994).

Wichman, I. S., Flame Spread in an Opposed Flow with a Linear Velocity

Gradient, *Combustion and Flame*, **50**, 287 (1983).

Wichman, I. S. and Williams, F. A., Simplified Model of Flame Spread in an Opposed Flow along a Flat Surface of a Semi-infinite Solid, *Combustion Science and Technology*, **32**, 91 (1983a).

Wichman, I. S. and Williams, F. A., Comments on Rates of Creeping Spread of Flame Over Thermally Thin Fuels, *Combustion Science and Technology*, **33**, 207 (1983b).

Wichman, I. S., Theory of Opposed-Flow Flame Spread, *Progress Energy Combustion Science*, **18**, 553 (1992).

Wu, K. K., Fan, W. F., Chen C. H., Liou, T. M. and Pan, I. J., Downward Flame Spread over a Thick PMMA Slab in an Opposed Flow Environment: Experiment and Modeling, *Combustion and Flame*, **132**, 697 (2003).

Wu, K. K. and Chen, C. H., A Numerical Analysis of Ignition to Steady Downward Flame Spread over a Thin Solid Fuel, *Combustion Science and Technology*, **175**, 933 (2003).

Wu, K. K.,. A Study of Flame Behaviors over a Solid Fuel in a Natural Convection Environment. Ph.D. Dissertation, National Chiao Tung University, Hsinchu, Taiwan, R.O.C. (2003).

Wu, K. K. and Chen, C. H., Radiation effects for Downward Flame Spread over a Thermally Thin Fuel in A Partial Gravity Environment, *Combustion Science and Technology*, **176**, 1909 (2004).

Zhu, X. L. and Gore, J.P., Radiation Effects on Combustion and Pollutant Emissions of High-pressure Opposed Flow Methane/Air Diffusion Flames, *Combustion and Flame*, **141**, 118 (2005).

Appendix A

Derivation of finite difference equations

A.1 Introduction

The momentum, energy and species equations (Eqs.(2.37)-(2.42)), with the continuity equation, can be rewritten in the following general form:

$$\frac{\partial}{\partial x}(\rho u\phi - \Gamma\frac{\partial\phi}{\partial x}) + \frac{\partial}{\partial y}(\rho v\phi - \Gamma\frac{\partial\phi}{\partial y}) = S_\phi \tag{A.1}$$

where ϕ is the dependent variable, Γ and S_ϕ represent the conductance and the source terms relevant to ϕ. The finite difference equation for each dependent variable is derived by integrating Eq. (A.1) over the corresponding computational cell, the integrations of temperature, fuel and oxidizer mass fractions are performed over the main cell, the integrations for the velocity components u and v, are carried out over the u cell and the v cell respectively.

The integrating procedures for all these equations are the same. Therefore, a detailed derivation for the variable integrating over the main cell is sufficient to illustrate the procedure and it is given in the next section. A summation of the results of integration for all of the variables is presented in section A.3.

A.2 Integration procedure

In the main cell, shown in figure A, attention is focused on the grid point P, which has the points E, W, N and S as its neighbors. The letters e, w, n and s denote the faces of control volume which are located at the mid-way between the grid points.

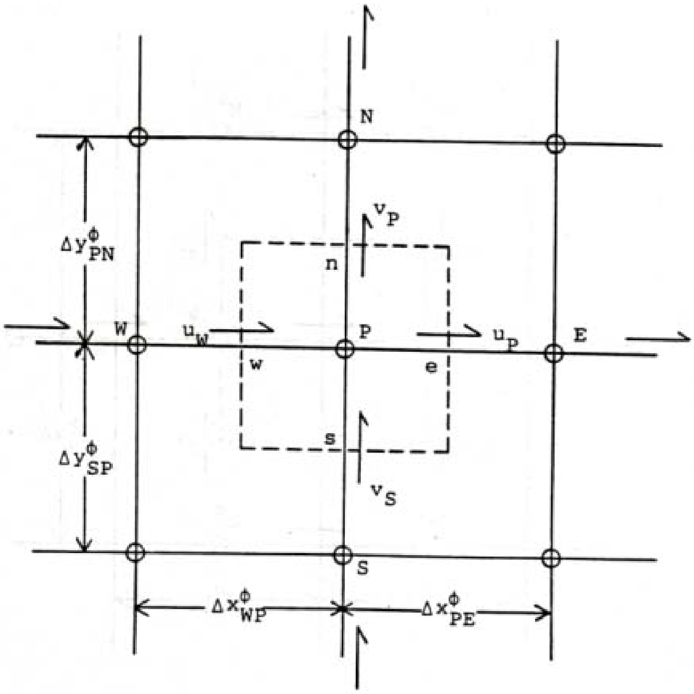

Figure A. Main cell

The integration of Eq. (A.1) over the main cell is

$$\int_s^n \int_w^e \frac{\partial}{\partial x}(\rho u \phi - \Gamma \frac{\partial \phi}{\partial x}) dxdy + \int_w^e \int_s^n \frac{\partial}{\partial y}(\rho v \phi - \Gamma \frac{\partial \phi}{\partial y}) dydx = \int_s^n \int_w^e S_\phi dxdy \tag{A.2}$$

The first integral on the left-hand side of Eq. (A.2) can be written as

$$\int_s^n \int_w^e \frac{\partial}{\partial x}(\rho u \phi - \Gamma \frac{\partial \phi}{\partial x}) dxdy = \int_s^n (\rho u \phi - \Gamma \frac{\partial \phi}{\partial x})_w^e dy = I_e - I_w \tag{A.3}$$

where

$$I_e = \int_s^n (\rho u \phi - \Gamma \frac{\partial \phi}{\partial x})_e dy$$

$$I_w = \int_s^n (\rho u \phi - \Gamma \frac{\partial \phi}{\partial x})_w dy$$

Approximately, I_e is given by

$$I_e = [(\rho u)_e \phi_e - \Gamma_e (\frac{\partial \phi}{\partial x})_e] A_{ew} \tag{A.4}$$

where $A^{\phi}_{ew} = \frac{1}{2}(\Delta y^{\phi}_{NP} + \Delta y^{\phi}_{PS})$ is the east or the west fact area of the control volume.

Eq. (A.4) consists of convection and conduction/diffusion terms. The most straight forward way to obtain the expression for both terms is assuming a piecewise-linear profile between the grid points. However, this kind of treatment sometimes causes disastrous outcome such that the finite difference equation may diverge. The power low scheme is applied on the convection term only, whereas the conduction term is still using the central difference scheme. Using this, Eq. (A.4) becomes

$$I_e = [\frac{1}{2}(\rho_E + \rho_P)u_P\phi_P - \frac{\Gamma_P + \Gamma_E}{2}\frac{\phi_E - \phi_P}{\Delta x_{PE}}]A_{ew}^{\phi} \tag{A.5a}$$

if $u_E > 0$

$$I_e = [\frac{1}{2}(\rho_E + \rho_E)u_P\phi_E - \frac{\Gamma_P + \Gamma_E}{2}\frac{\phi_E - \phi_P}{\Delta x_{PE}}]A_{ew}^{\phi} \tag{A.5b}$$

if $u_E < 0$

let

$$m_E^{\phi} = \frac{1}{2}(\rho_P + \rho_E)u_P A_{ew}^{\phi}$$

$$d_E^{\phi} = \frac{1}{2}(\frac{\Gamma_P + \Gamma_E}{\Delta x_{PE}^{\phi}})A_{ew}^{\phi} + \frac{1}{2}\left|m_E^{\phi}\right| \tag{A.6}$$

With the definitions given by Eq. (A.6), the conditional statements (A.5) can be written in a more compact form:

$$I_e = (d_E^{\phi} + \frac{1}{2}m_E^{\phi})\phi_P - (d_E^{\phi} - \frac{1}{2}m_E^{\phi})\phi_E \tag{A.7}$$

Using a similar manipulation for I_w in Eq. (A.3), we have

$$I_w = (d_W^{\phi} + \frac{1}{2}m_W^{\phi})\phi_W - (d_W^{\phi} - \frac{1}{2}m_W^{\phi})\phi_P \tag{A.8}$$

where

$$m_W^{\phi} = \frac{1}{2}(\rho_W + \rho_P)u_W A_{ew}^{\phi}$$

$$d_W^\phi = \frac{1}{2}(\frac{\Gamma_W + \Gamma_P}{\Delta x_{WP}^\phi})A_{ew}^\phi + \frac{1}{2}\left|m_W^\phi\right|$$

Substituting Eqs. (A.7) and (A.8) into Eq. (A.3) we get

$$\int_s^n \int_w^e \frac{\partial}{\partial x}(\rho u \phi - \Gamma \frac{\partial \phi}{\partial x})dxdy = I_e - I_w$$

$$= (d_E^\phi + \frac{1}{2}m_E^\phi + d_W^\phi - \frac{1}{2}m_W^\phi)\phi_P - (d_E^\phi - \frac{1}{2}m_E^\phi)\phi_E - (d_W^\phi + \frac{1}{2}m_W^\phi)\phi_W \qquad \text{(A.9)}$$

Similarly, the second integral on the left-hand side of Eq. (A.2) can be written as

$$\int_w^e \int_s^n \frac{\partial}{\partial y}(\rho v \phi - \Gamma \frac{\partial \phi}{\partial y})dydx$$

$$= (d_N^\phi + \frac{1}{2}m_N^\phi + d_S^\phi - \frac{1}{2}m_S^\phi)\phi_P - (d_N^\phi - \frac{1}{2}m_N^\phi)\phi_N - (d_S^\phi + \frac{1}{2}m_S^\phi)\phi_S \qquad \text{(A.10)}$$

where

$$m_N^\phi = \frac{1}{2}(\rho_P + \rho_N)v_P A_{ns}^\phi$$

$$m_S^\phi = \frac{1}{2}(\rho_S + \rho_P)v_S A_{ns}^\phi$$

$$d_N^\phi = \frac{1}{2}(\frac{\Gamma_P + \Gamma_N}{\Delta y_{PN}^\phi})A_{ns}^\phi + \frac{1}{2}\left|m_N^\phi\right|$$

$$d_S^\phi = \frac{1}{2}(\frac{\Gamma_S + \Gamma_P}{\Delta y_{SP}^\phi})A_{ns}^\phi + \frac{1}{2}\left|m_S^\phi\right|$$

and $A_{ns}^\phi = \frac{1}{2}(\Delta x_{PE}^\phi + \Delta x_{WP}^\phi)$ is the north or south face area of the control volume.

The resulting appearance of integration for the source term on the right-hand side of Eq. (A.2) depends on the actual expression S_ϕ itself. However, the integrating procedure is the same as what has been presented. In order to achieve a converged solution, the resulting finite difference representation of the source term is suggested to be in the following form:

$$\int_s^n \int_w^e S_\phi dxdy = S_1^\phi + S_P^\phi \phi_P \qquad \text{(A.11)}$$

where the quantity S_P^ϕ must not be positive to make numerical scheme stable.

Finally, substituting Equ. (A.9), (A.10) and (A.11) into Eq. (A.2), the differential equation can be transformed into a standard form of fully implicit finite difference equation:

$$a_P^\phi \phi_P = a_E^\phi \phi_E + a_W^\phi \phi_W + a_N^\phi \phi_N + a_s^\phi \phi_S + S_C^\phi \tag{A.12}$$

where

$$a_E^\phi = d_E^\phi - \frac{1}{2} m_E^\phi$$

$$a_W^\phi = d_W^\phi - \frac{1}{2} m_W^\phi$$

$$a_N^\phi = d_N^\phi - \frac{1}{2} m_N^\phi$$

$$a_S^\phi = d_S^\phi - \frac{1}{2} m_S^\phi$$

$$a_P^\phi = a_E^\phi + a_W^\phi + a_N^\phi + a_s^\phi + (m_E^\phi - m_W^\phi + m_N^\phi - m_S^\phi) - S_P$$

$$S_C^\phi = S_1^\phi$$

The coefficients, a_E, a_W, a_N and a_S, are guaranteed to be positive quantities by the definition themselves. For convergence, the value of a_P^ϕ should be positive. A special treatment for the mass source term, $(m_E - m_W + m_N - m_S)$, inside a_P^ϕ is needed. The finite difference equation for continuity equation is obtained by integrating Eq. (2.37) over the main cell. The result is

$$C_E u_P - C_W u_W + C_N v_P - C_S v_S = 0 \tag{A.13}$$

where

$$C_E = \frac{1}{2}(\rho_P + \rho_E) A_{ew}^\phi$$

$$C_W = \frac{1}{2}(\rho_W + \rho_P) A_{ew}^\phi$$

$$C_N = \frac{1}{2}(\rho_P + \rho_N) A_{ns}^\phi$$

$$C_S = \frac{1}{2}(\rho_S + \rho_P)A_{ns}^{\phi}$$

If mass balance is achieved in the control volume, from Eq. (A.13), the term of $(m_E - m_W + m_N - m_S)$ vanishes in Eq. (A.12). During the iteration procedure, however, this term usually is not zero and may lead to computational instability. The trick used to avoid this condition is to replace a_P^{ϕ} and S_C^{ϕ} in Eq. (A.12) by

$$a_P^{\phi} = a_E^{\phi} + a_W^{\phi} + a_N^{\phi} + a_s^{\phi} + Max(m_E^{\phi} - m_W^{\phi} + m_N^{\phi} - m_S^{\phi}, 0) - S_P \qquad \text{(A.14)}$$

$$S_C^{\phi} = S_1^{\phi} + Max(m_E^{\phi} - m_W^{\phi} + m_N^{\phi} - m_S^{\phi}, 0)\phi_P \qquad \text{(A.15)}$$

where superscript + denotes the quantity resulted from last iteration. This will ensure that all of the coefficients in Eq. (A.12) are positive to avoid the divergence due to the existence of negative coefficient in a_P^{ϕ}.

A.3. Summation of Finite Difference Equations

The forms of finite difference equations for T, Y_F and Y_O are identical except the expression of some of the coefficients. The form of the equation is given by Eq. (A.12) except the coefficients a_P^{ϕ} and S_C^{ϕ} are replaced using Eqns. (A.14) and (A.15).

For $\phi = u$, the finite difference equation is

$$a_P^u u_P = a_E^u u_E + a_W^u u_W + a_N^u u_N + a_s^u u_S + (P_P - P_E)A_{ew}^u + S_C^u$$

where

$a_i^u = d_i^u - \frac{1}{2}m_i^u$ for i = E or N

$a_i^u = d_i^u + \frac{1}{2}m_i^u$ for I = W or S

$$d_E^u = \frac{\mu_E}{\mathrm{Re}\,\Delta x_{PE}^u} + \frac{1}{2}\left|m_E^u\right|$$

$$d_W^u = \frac{\mu_P}{\mathrm{Re}\,\Delta x_{WP}^u} + \frac{1}{2}\left|m_W^u\right|$$

$$d_N^u = \frac{1}{4}(\frac{\mu_E + \mu_P + \mu_N + \mu_{NE}}{\mathrm{Re}\,\Delta y_{SP}}) + \frac{1}{2}\left|m_N^u\right|$$

$$d_S^u = \frac{1}{4}(\frac{\mu_E + \mu_P + \mu_N + \mu_{SE}}{\mathrm{Re}\,\Delta y_{SP}}) + \frac{1}{2}\left|m_W^u\right|$$

$$m_E^u = \frac{1}{4}[(\rho_E + \rho_P)u_P + (\rho_E + \rho_{EE})u_E]A_{ew}^u, \quad EE = E + 1$$

$$m_W^u = \frac{1}{4}[(\rho_E + \rho_P)u_P + (\rho_P + \rho_W)u_W]A_{ew}^u$$

$$m_N^u = \frac{1}{4}[(\rho_E + \rho_{NE})v_E + (\rho_P + \rho_N)v_P]A_{ns}^u$$

$$m_S^u = \frac{1}{4}[(\rho_E + \rho_{SE})v_{SE} + (\rho_P + \rho_S)v_S]A_{ns}^u$$

$$A_{ew}^u = \frac{1}{2}(\Delta y_{PN}^u + \Delta y_{SP}^u)$$

$$A_{ns}^u = \frac{1}{2}(\Delta x_{PE}^u + \Delta x_{WP}^u)$$

$$a_P^u = a_E^u + a_W^u + a_N^u + a_S^u + Max(m_E^u - m_W^u + m_N^u - m_S^u, 0) - S_P$$

$$S_C^u = S_1^u + Max(m_E^u - m_W^u + m_N^u - m_S^u, 0)u_P^+$$

$$S_1^u = \frac{1}{3\mathrm{Re}}[\frac{\mu_E}{\Delta x_{PE}^u}u_E - (\frac{\mu_E}{\Delta x_{PE}^u} + \frac{\mu_P}{\Delta x_{WP}^u})u_P + \frac{\mu_P}{\Delta x_{WP}^u}u_W]A_{ew}$$

$$+ \frac{1}{\mathrm{Re}}[(\frac{\mu_P + \mu_E + \mu_{NE} + \mu_N}{4} - \frac{2}{3}\mu_E)v_E$$

$$+ (\frac{2}{3}\mu_E - \frac{\mu_P + \mu_E + \mu_{SE} + \mu_S}{4})v_{SE}$$

$$+ (\frac{2}{3}\mu_W - \frac{\mu_P + \mu_E + \mu_{NE} + \mu_N}{4})v_P$$

$$+ (\frac{\mu_P + \mu_E + \mu_{SE} + \mu_S}{4} - \frac{2}{3}\mu_W)v_S]$$

For $\phi = v$, the finite difference equation is

$$a_P^v v_P = a_E^v v_E + a_W^v v_W + a_N^v v_N + a_s^v v_S + (P_P - P_N)A_{NS}^v + S_C^v$$

where

$$a_i^v = d_i^v - \frac{1}{2} m_i^v \quad \text{for i = E or N}$$

$$a_i^v = d_i^v + \frac{1}{2} m_i^v \quad \text{for I = W or S}$$

$$d_N^v = \frac{\mu_N}{\mathrm{Re}\,\Delta y_{PN}^v} A_{ns}^v + \frac{1}{2}\left|m_N^v\right|$$

$$d_S^u = \frac{\mu_P}{\mathrm{Re}\,\Delta y_{SP}^v} A_{ns}^v + \frac{1}{2}\left|m_S^v\right|$$

$$d_E^v = \frac{1}{4}\left(\frac{\mu_E + \mu_P + \mu_N + \mu_{NE}}{\mathrm{Re}\,\Delta x_{PE}^v}\right) A_{ew}^v + \frac{1}{2}\left|m_E^v\right|$$

$$d_W^u = \frac{1}{4}\left(\frac{\mu_E + \mu_W + \mu_N + \mu_{NW}}{\mathrm{Re}\,\Delta x_{WP}^V}\right) + \frac{1}{2}\left|m_W^v\right|$$

$$m_E^v = \frac{1}{4}[(\rho_N + \rho_{NE})u_N + (\rho_P + \rho_E)u_P]A_{ew}^v$$

$$m_W^v = \frac{1}{4}[(\rho_N + \rho_{NW})u_{NW} + (\rho_P + \rho_W)u_W]A_{ew}^v$$

$$m_N^v = \frac{1}{4}[(\rho_P + \rho_N)v_P + (\rho_N + \rho_{NN})v_N]A_{ns}^v, \quad NN = N + 1$$

$$m_S^v = \frac{1}{4}[(\rho_P + \rho_N)v_P + (\rho_P + \rho_S)v_S]A_{ns}^v$$

$$A_{ew}^v = \frac{1}{2}(\Delta y_{PN}^v + \Delta y_{SP}^v)$$

$$A_{ns}^v = \frac{1}{2}(\Delta x_{PE}^v + \Delta x_{WP}^v)$$

$$a_P^v = a_E^v v_E + a_W^v v_W + a_N^v v_N + a_S^v v_S + Max(m_E^v - m_W^v + m_N^v - m_S^v) - S_P$$

$$S_C^v = S_1^v + Max(m_E^v - m_W^v + m_N^v - m_S^v)v_P^+$$

$$S_1^v = \frac{1}{3\mathrm{Re}}\left[\frac{\mu_N}{\Delta y_{PN}^v} v_N - \left(\frac{\mu_N}{\Delta y_{PN}^v} + \frac{\mu_S}{\Delta y_{SP}^v}\right)v_P + \frac{\mu_S}{\Delta y_{SP}^v} v_S\right]A_{ns}$$

$$+ \frac{1}{\mathrm{Re}}\left[\left(\frac{\mu_P + \mu_E + \mu_{NE} + \mu_N}{4} - \frac{2}{3}\mu_N\right)u_N\right.$$

$$+(\frac{2}{3}\mu_N - \frac{\mu_N + \mu_P + \mu_W + \mu_{NW}}{4})u_{NW}$$

$$+(\frac{2}{3}\mu_S - \frac{\mu_N + \mu_P + \mu_E + \mu_{NE}}{4})u_P$$

$$+(\frac{\mu_N + \mu_P + \mu_W + \mu_{NW}}{4} - \frac{2}{3}\mu_S)u_W\,]$$

Table 1 Non-dimensional governing equations

Gas phase governing equation

$$\frac{\partial}{\partial t}(\rho\phi)+\frac{\partial}{\partial x}\left(\rho u\phi-\Gamma\frac{\partial\phi}{\partial x}\right)+\frac{\partial}{\partial y}\left(\rho v\phi-\Gamma\frac{\partial\phi}{\partial y}\right)=S$$

Equation	ϕ	Γ	S
Continuity	1	-	0
X-momentum	u	$\frac{\mu}{\mathrm{Re}}$	$-\frac{\partial P}{\partial x}+S_u+\frac{Gr}{\mathrm{Re}^2}(\rho_\infty-\rho)$
Y-momentum	v	$\frac{\mu}{\mathrm{Re}}$	$-\frac{\partial P}{\partial y}+S_v$
Energy	T	$\frac{\mu}{\mathrm{Pr}\,\mathrm{Re}}$	$-q\dot{\omega}_F-\frac{a}{N_\infty}\left(T^4-I_0\right)$
Fuel	Y_F	$\frac{\mu}{\mathrm{Pr}\,\mathrm{Re}\,Le}$	$\dot{\omega}_F$
Other species $i=O_2,CO_2,H_2O$	Y_i	$\frac{\mu}{\mathrm{Pr}\,\mathrm{Re}\,Le}$	$f_i\dot{\omega}_F$

Solid phase governing equations

Mass	$\frac{\partial\rho_s}{\partial t}=-(A_s)\left(\frac{\rho_s-\rho_{sf}}{1-\rho_{sf}}\right)\exp\left(-\frac{E_s}{T_s}\right)$
Energy	$\rho_s\frac{\partial T_s}{\partial t}=\frac{\partial m_s''}{\partial y}\tau\left[L+(1-C)(T_s-1)\right]+\alpha_s\frac{\partial^2T_s}{\partial x^2}+\alpha_s\frac{\partial^2T_s}{\partial y^2}-(Cm_s''\tau)\frac{\partial T_s}{\partial y}$

Radiation transport equation : $\frac{\partial^2 I_0}{\partial x^2}+\frac{\partial^2 I_0}{\partial y^2}=-3a^2(T^4-I_0)$

where

$$S_u=\frac{1}{3}\frac{\partial}{\partial x}(\frac{\mu}{\mathrm{Re}}\frac{\partial u}{\partial x})+\frac{\partial}{\partial y}(\frac{\mu}{\mathrm{Re}}\frac{\partial v}{\partial x})-\frac{2}{3}\frac{\partial}{\partial x}(\frac{\mu}{\mathrm{Re}}\frac{\partial v}{\partial y})$$

$$S_v=\frac{1}{3}\frac{\partial}{\partial y}(\frac{\mu}{\mathrm{Re}}\frac{\partial v}{\partial y})+\frac{\partial}{\partial x}(\frac{\mu}{\mathrm{Re}}\frac{\partial u}{\partial y})-\frac{2}{3}\frac{\partial}{\partial y}(\frac{\mu}{\mathrm{Re}}\frac{\partial u}{\partial x})$$

$$\dot{\omega}_F=-Da\rho^2Y_FY_O\exp(-E/T)$$

Table 2 Grid and time step test results

Grid number $x \times y$	Time step (s)	Ignition delay time (s)
290×125	0.02	14.12
290×95	0.02	14.12
315×95	0.02	14.12
330×95	0.02	14.12
290×95	0.05	14.46

Table 3 The discrepancies between the combustion models of Wu et al. (2003) and present work.

	Finite-length solid fuel	Enclosure effect	Gas and solid phase radiations	3D effect
Wu et al. (2003)	x	x	x	x
Present work	O	O	O	x

Table 4 Gas and solid properties values

Symbol	Value	Unit
$\bar{E}_s$	1.298×10^{5}	J/mol
$\bar{A}_s$	2.282×10^{9}	1/s
$\bar{L}$	-941.08	J/g
$\bar{k}_s$	2.675×10^{-3}	W/cmK
$\bar{C}_s$	1.465	J/gK
$\bar{\rho}_{s\infty}$	1.19	g/cm^3
$\bar{T}_v$	668	K
f	1.92	-
$\bar{C}_p$	$f(\bar{T}^*)$	J/gK
$\bar{u}_\infty$	variable	cm/s
$Y_{O\infty}$	0.233	-
$\bar{\rho}^*$	$f(\bar{T}^*)$	g/cm^3
$\bar{q}$	2.59×10^{4}	J/g
$\bar{\alpha}^*$	$f(\bar{T}^*)$	cm^2/s
$\bar{T}_\infty$	variable	K
$\bar{k}^*$	$f(\bar{T}^*)$	W/cmK
$\bar{\mu}^*$	$f(\bar{T}^*)$	g/cms
$\bar{E}$	8.895×10^{4}	J/mol
$\bar{B}$	5.928×10^{12}	cm^3/mols
$\bar{\tau}$	variable	cm
ε	1	-

Table 5 Non-dimensional parameters

Symbol	Parameter group	Value
A_s	$\overline{A}_s\overline{\alpha}^* / \overline{V}_r^{\,2}$	Variable
a	$\overline{a}\overline{\delta}$	Variable
C	$\overline{C_p} \big/ \overline{C_s}$	0.85
D_a	$\overline{B}\overline{\rho}^*\overline{\delta} / \overline{V}_r$	Variable
E	$\overline{E} \big/ \overline{R}\overline{T_\infty}$	32.129
E_s	$\overline{E}_s \big/ \overline{R}\overline{T_\infty}$	46.883
Gr	$\overline{g}(\overline{\rho_\infty} - \overline{\rho_f})\overline{\delta}^3 \Big/ \overline{\rho^*}\,\overline{\nu^*}^2$	Variable
k_s	$\overline{k_s} \big/ \overline{k^*}$	2.693
L	$\overline{L} \big/ \overline{C_s}\overline{T_\infty}$	-1.929
L_e	$\overline{\alpha} \big/ \overline{D}$	1.000
N_∞	$\overline{k^*}\,\overline{V_r} / \overline{\sigma T_\infty}^3\,\overline{\alpha^*}$	Variable
P_r	$\overline{\nu} \big/ \overline{\alpha}$	0.702
q	$\overline{q} \big/ \overline{C_p}\overline{T_\infty}$	62.459
R_e	$\overline{\rho}^*\overline{\alpha}^* \big/ \overline{\mu}^*$	1.424
T_V	$\overline{T_v} \big/ \overline{T_\infty}$	2.006
γ	$\overline{T^*} \big/ \overline{T_\infty}$	4.765
ρ_{sf}	$\overline{\rho_{sf}} \big/ \overline{\rho_{s\infty}}$	0.07
$\overline{\delta}$	$\overline{\alpha^*} / \overline{V_r}$	Variable
τ	$\overline{\tau}\overline{C}_s\overline{\rho}_{s\infty}\overline{V}_r / \overline{k}^*$	Variable
α_s	$\overline{\alpha}_s / \overline{\alpha}^*$	4.293×10^{-4}

Table 6 Effect of changing opposed flow velocity

$\overline{u_\infty}$ (cm/s)	$\overline{V_f}$ (cm/s)	$1/N_\infty$	Da
7	1.05×10^{-3}	0.076	4.87×10^{6}
10	2×10^{-3}	0.053	3.41×10^{6}
15	3.28×10^{-3}	0.035	1.95×10^{6}
30	4.98×10^{-3}	0.018	1.7×10^{6}
32	5.21×10^{-3}	0.017	1.56×10^{6}
35	5.07×10^{-3}	0.015	1.46×10^{6}
40	4.92×10^{-3}	0.013	7.3×10^{5}
70	3.4×10^{-3}	0.007	4.9×10^{5}
100	2.48×10^{-3}	0.005	3.4×10^{5}

Table 7 Non-dimensional governing equations

Gas phase governing equation

$$\frac{\partial}{\partial t}(\rho\phi)+\frac{\partial}{\partial x}\left(\rho u\phi-\Gamma\frac{\partial\phi}{\partial x}\right)+\frac{\partial}{\partial y}\left(\rho v\phi-\Gamma\frac{\partial\phi}{\partial y}\right)+\frac{\partial}{\partial z}\left(\rho z\phi-\Gamma\frac{\partial\phi}{\partial z}\right)=S$$

Equation	ϕ	Γ	S
Continuity	1	-	0
X-momentum	u	$\frac{\mu}{\mathrm{Re}}$	$-\frac{\partial P}{\partial x}+S_u+\frac{Gr}{\mathrm{Re}^2}(\rho_\infty-\rho)$
Y-momentum	v	$\frac{\mu}{\mathrm{Re}}$	$-\frac{\partial P}{\partial y}+S_v$
Z-momentum	w	$\frac{\mu}{\mathrm{Re}}$	$-\frac{\partial P}{\partial z}+S_w$
Energy	T	$\frac{\mu}{\mathrm{Pr}\,\mathrm{Re}}$	$-q\dot{\omega}_F-\frac{a}{N_\infty}(T^4-I_0)$
Fuel	Y_F	$\frac{\mu}{\mathrm{Pr}\,\mathrm{Re}\,Le}$	$\dot{\omega}_F$
Other species $i=O_2,CO_2,H_2O$	Y_i	$\frac{\mu}{\mathrm{Pr}\,\mathrm{Re}\,Le}$	$f_i\dot{\omega}_F$

Solid phase governing equations

Mass	$\frac{\partial\rho_s}{\partial t}=-(A_s)\left(\frac{\rho_s-\rho_{sf}}{1-\rho_{sf}}\right)\exp\left(-\frac{E_s}{T_s}\right)$
Energy	$\rho_s\frac{\partial T_s}{\partial t}=\frac{\partial m''_s}{\partial y}[L+(1-C)(T_s-1)]+\alpha_s\frac{\partial^2T_s}{\partial x^2}+\alpha_s\frac{\partial^2T_s}{\partial y^2}+\alpha_s\frac{\partial^2T_s}{\partial z^2}-(Cm''_s)\frac{\partial T_s}{\partial y}-(Cm''_s)\frac{\partial T_s}{\partial z}$

where

$$S_u=\frac{1}{3}\frac{\partial}{\partial x}(\frac{\mu}{\mathrm{Re}}\frac{\partial u}{\partial x})+\frac{\partial}{\partial y}(\frac{\mu}{\mathrm{Re}}\frac{\partial v}{\partial x})-\frac{2}{3}\frac{\partial}{\partial x}(\frac{\mu}{\mathrm{Re}}\frac{\partial v}{\partial y}+\frac{\mu}{\mathrm{Re}}\frac{\partial w}{\partial z})+\frac{\partial}{\partial z}(\frac{\mu}{\mathrm{Re}}\frac{\partial w}{\partial x})$$

$$S_v=\frac{1}{3}\frac{\partial}{\partial y}(\frac{\mu}{\mathrm{Re}}\frac{\partial v}{\partial y})+\frac{\partial}{\partial x}(\frac{\mu}{\mathrm{Re}}\frac{\partial u}{\partial y})-\frac{2}{3}\frac{\partial}{\partial y}(\frac{\mu}{\mathrm{Re}}\frac{\partial u}{\partial x}+\frac{\mu}{\mathrm{Re}}\frac{\partial w}{\partial z})+\frac{\partial}{\partial z}(\frac{\mu}{\mathrm{Re}}\frac{\partial w}{\partial y})$$

$$S_w=\frac{1}{3}\frac{\partial}{\partial z}(\frac{\mu}{\mathrm{Re}}\frac{\partial w}{\partial z})+\frac{\partial}{\partial z}(\frac{\mu}{\mathrm{Re}}\frac{\partial w}{\partial z})-\frac{2}{3}\frac{\partial}{\partial z}(\frac{\mu}{\mathrm{Re}}\frac{\partial u}{\partial x}+\frac{\mu}{\mathrm{Re}}\frac{\partial v}{\partial y})+\frac{\partial}{\partial z}(\frac{\mu}{\mathrm{Re}}\frac{\partial w}{\partial z})$$

$$\dot{\omega}_F=-Da\rho^2Y_FY_O\exp(-E/T)$$

Table 8 The discrepancies between the part 1 and part 2 of present dissertation and the present work.

	Finite-length solid fuel	Enclosure effect	Gas and solid phase radiations	3D effect
part 1 and part 2 of present dissertation	O	O	O	x
Part 3 of present dissertation	O	O	O	O

Table 9 Grid and time step test results

Grid number $x\times y$	Time step (s)	Ignition delay time (s)
$290\times 95\times 50$	0.02	14.76
$290\times 95\times 75$	0.02	14.76
$290\times 95\times 100$	0.02	14.76
$290\times 95\times 125$	0.02	14.76
$290\times 95\times 50$	0.05	14.95

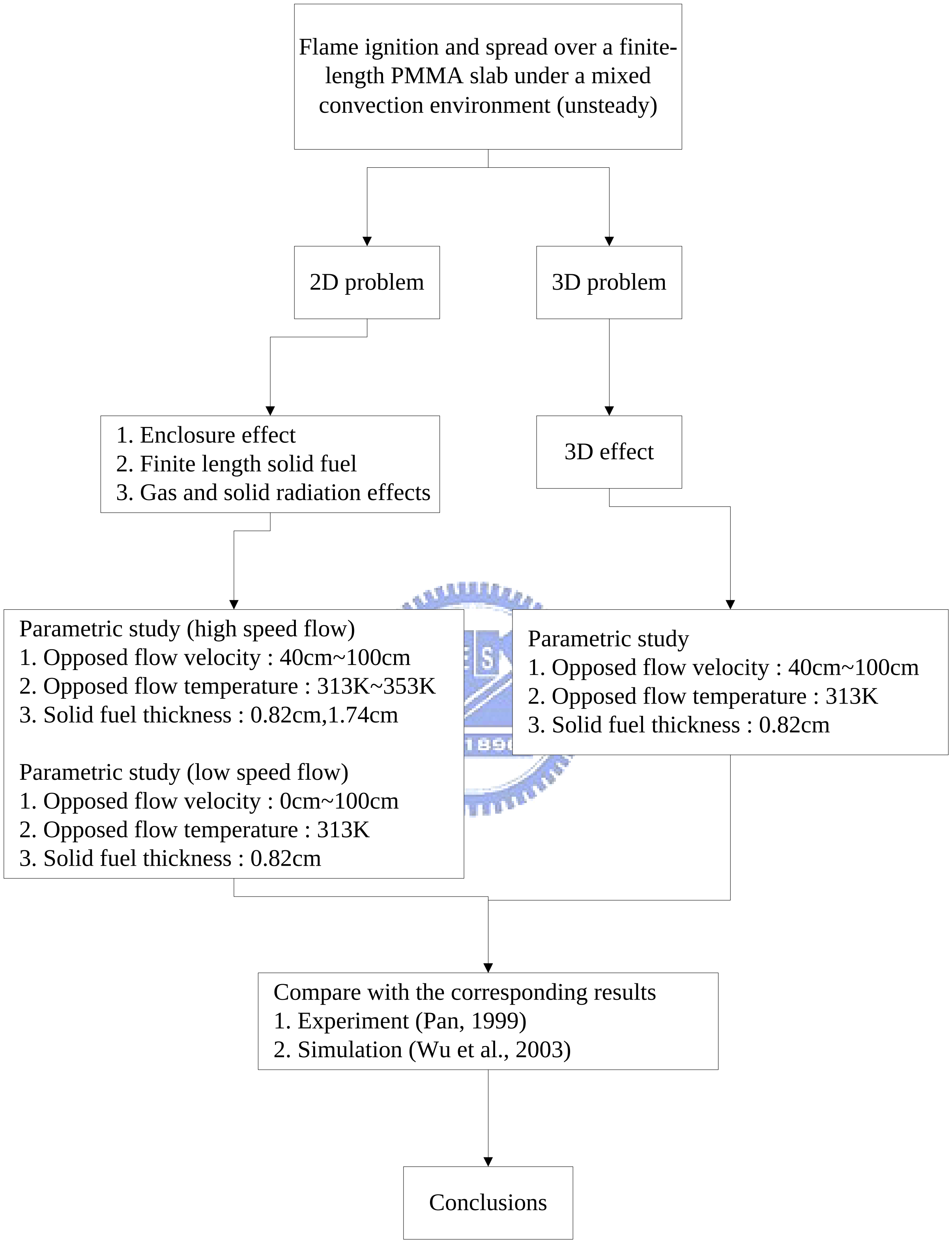

Figure 1.1 The structure of present dissertation.

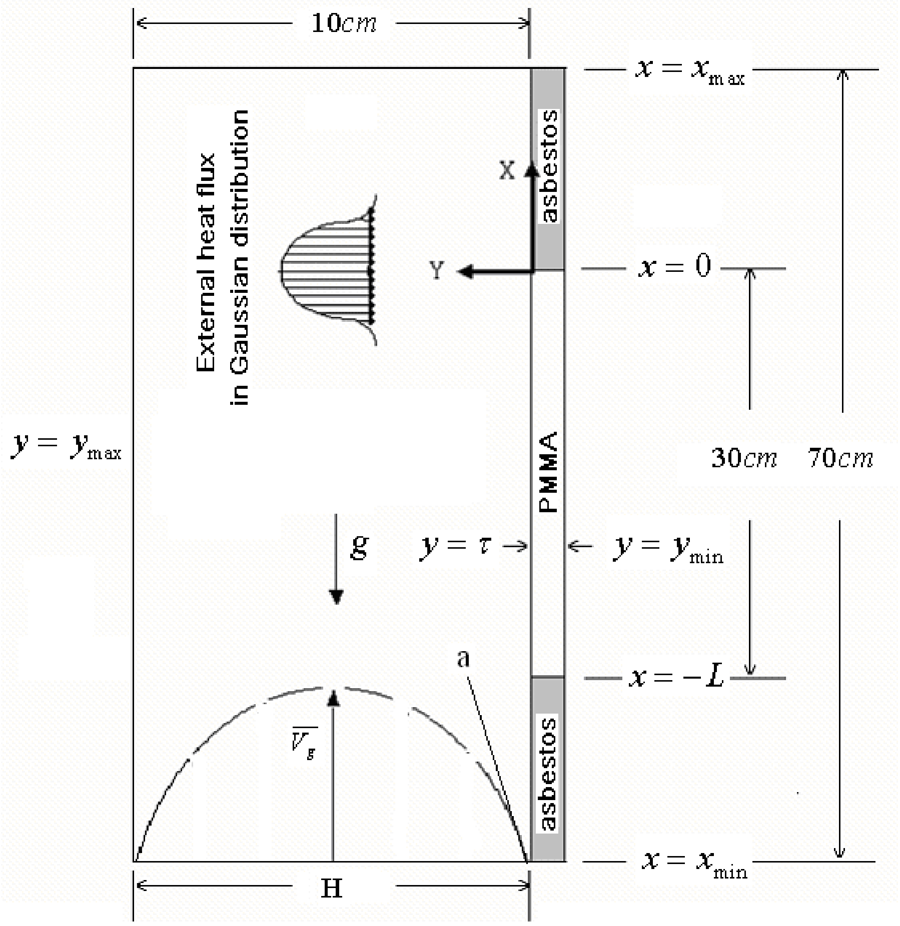

Figure 2.1 The schematic of flame spread over a thick PMMA slab in the mixed air flow in a wind tunnel.

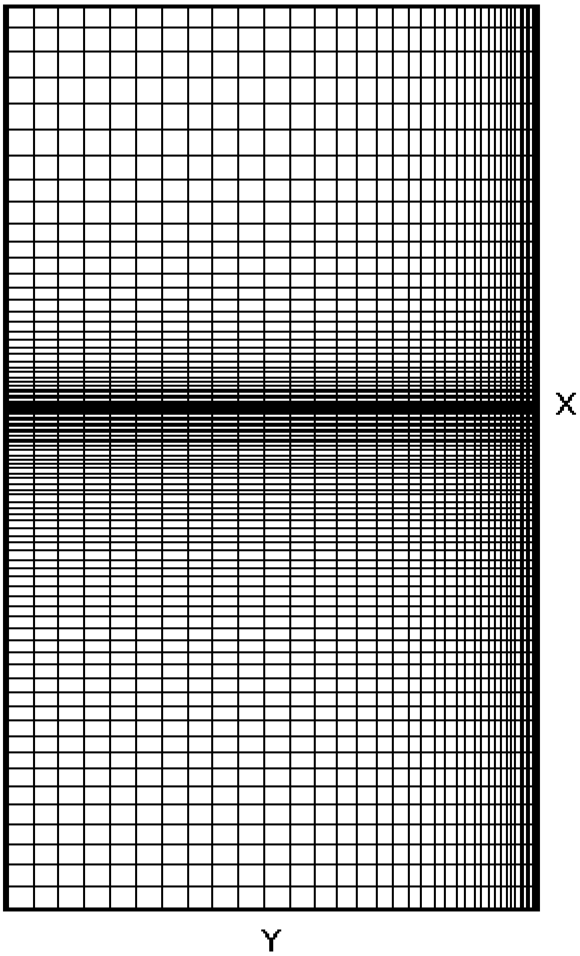

Figure 2.2 The non-uniform mesh distribution.

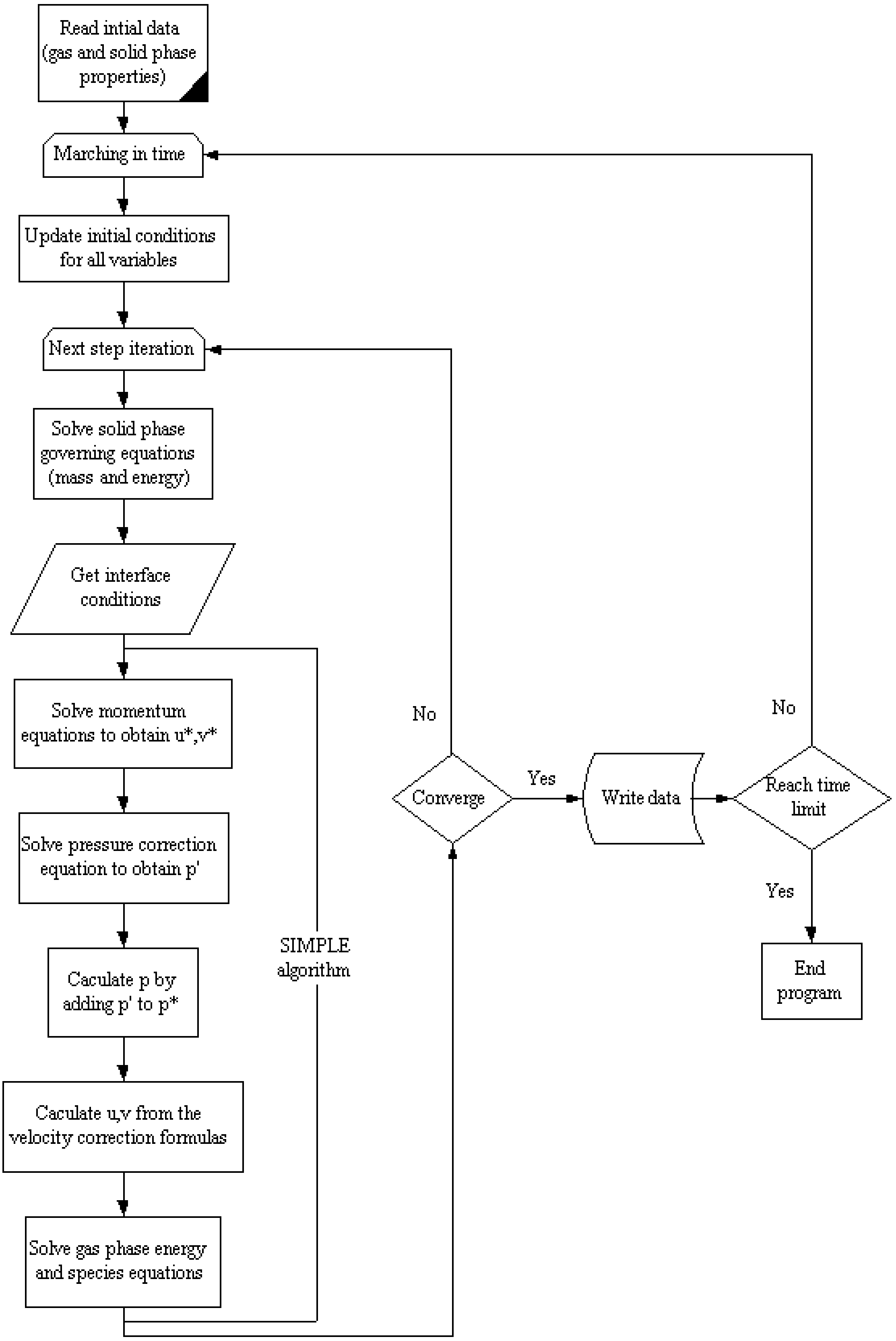

Figure 2.3 Computational algorithm for transient analysis.

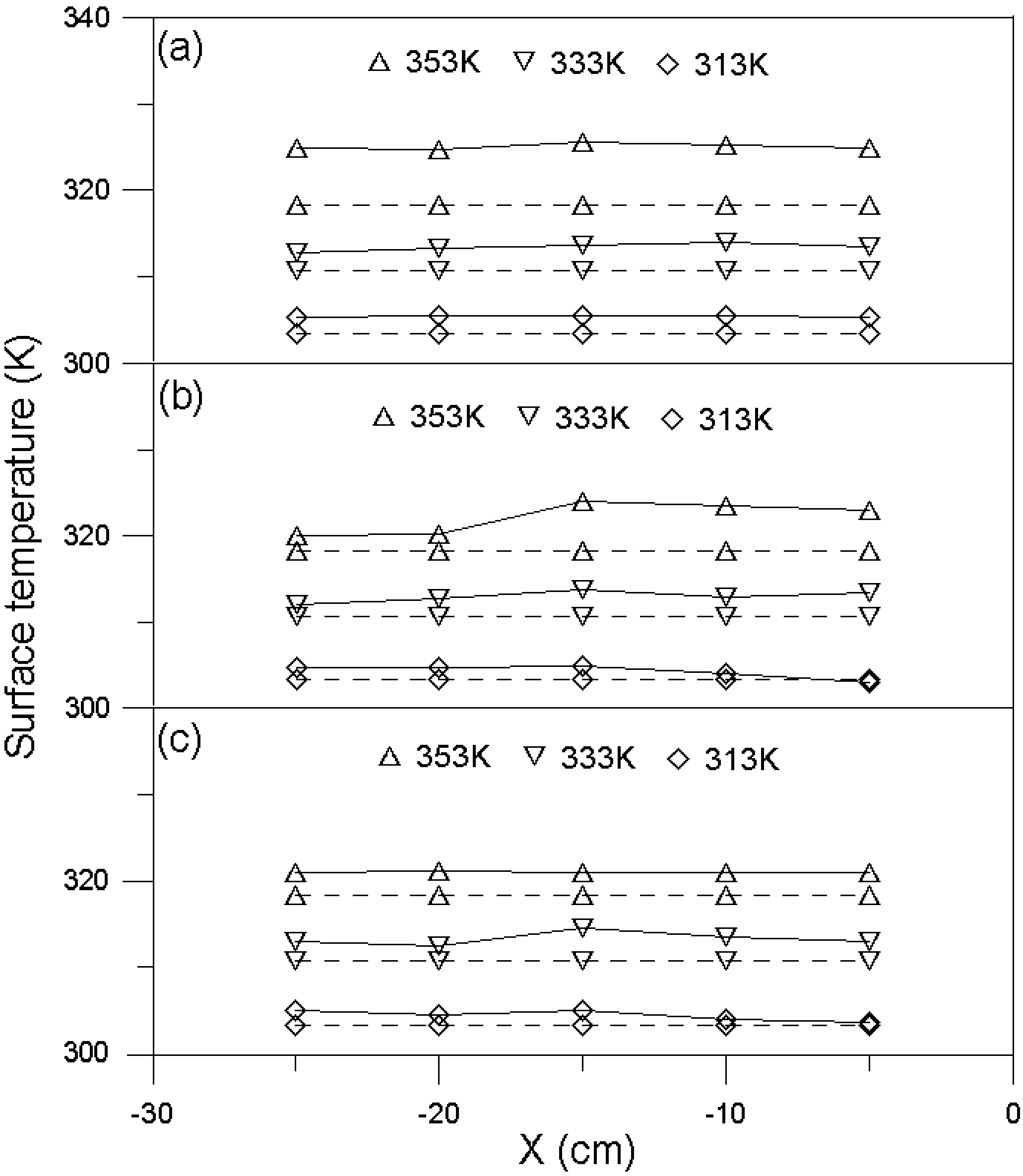

Figure 3.1.1 The steady temperature along PMMA surface under different opposed flow velocities for (a) $\bar{u}_\infty = 40 cm/s$ (b) $\bar{u}_\infty = 70 cm/s$ (c) $\bar{u}_\infty = 100 cm/s$, and the opposed flow temperatures are 313K, 333K and 353K, respectively. (solid and dashed lines represent the measurements and predictions, separately)

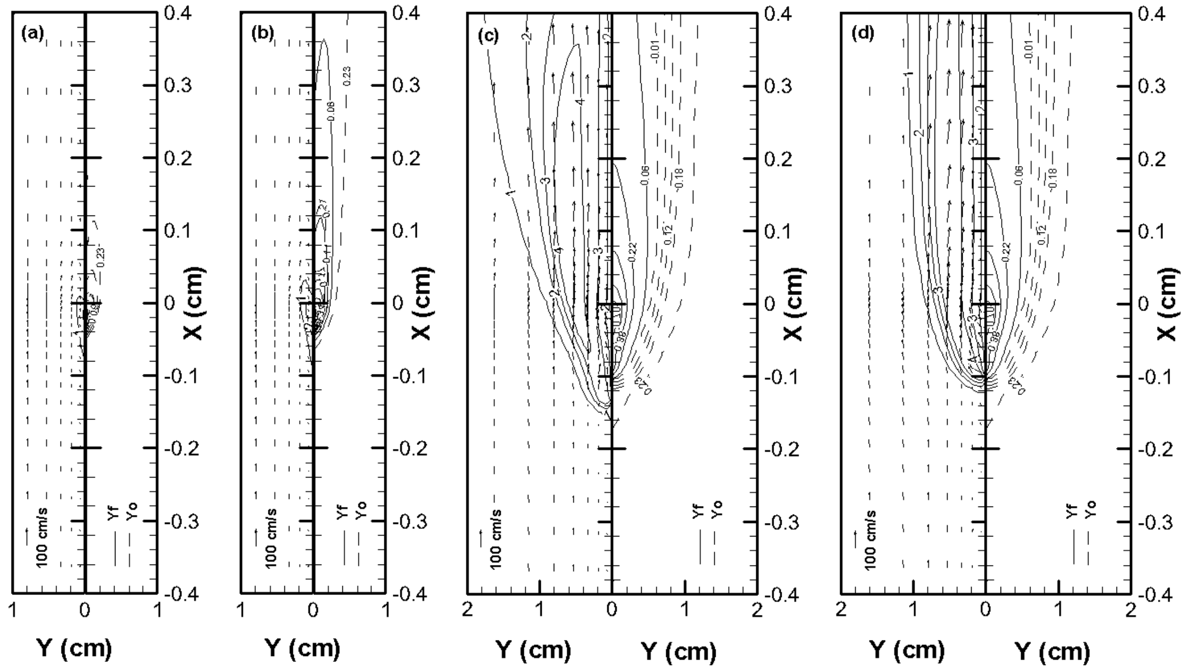

Figure 3.1.2 Time history of the flame profiles for $\overline{u_\infty} = 40cm/s$, $\overline{T_i} = 313K$ and $\bar{\tau} = 0.82cm$ at (a) $t = 12.5s$, (b) $t = 14.12s$, (c) $t = 14.14s$, (d) $t = 14.16s$, (e) $t = 17.08s$, (f) $t = 21.24s$, (g) $t = 25s$. Right half: fuel and oxidizer mass fraction distributions. Left half: temperature contours and flow velocity vector distribution.

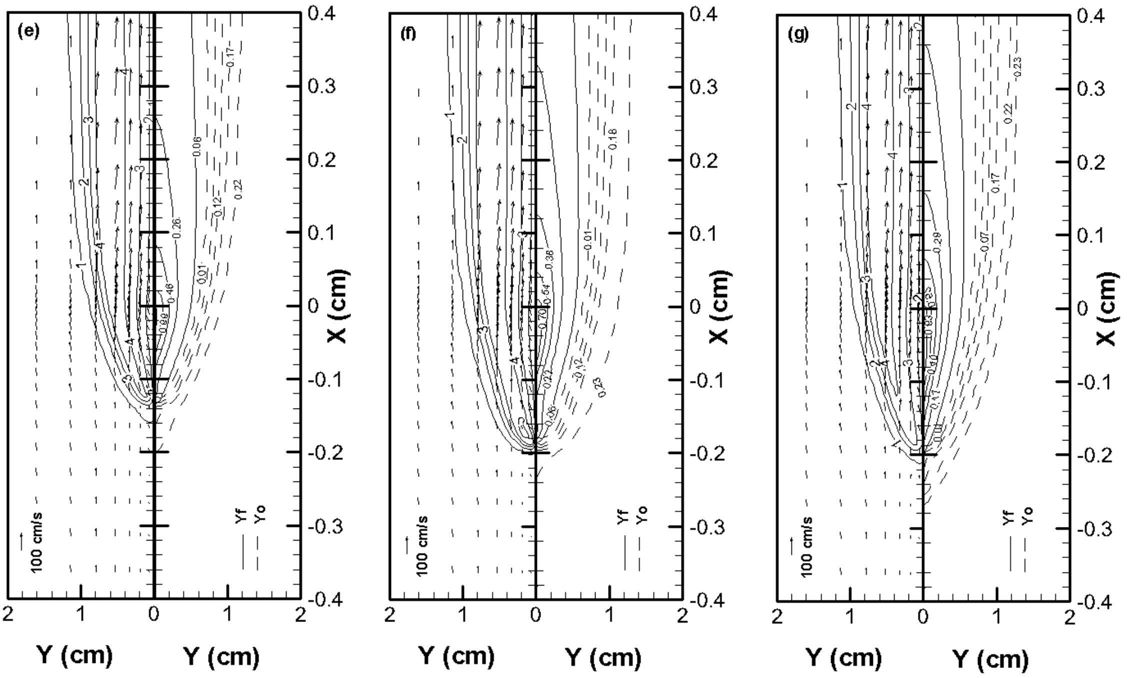

Figure 3.1.2 (continue) Time history of the flame profiles for $\overline{u_\infty} = 40cm/s$, $\overline{T_i} = 313K$ and $\overline{\tau} = 0.82cm$ at (a) $t = 12.5s$, (b) $t = 14.12s$, (c) $t = 14.14s$, (d) $t = 14.16s$, (e) $t = 17.08s$, (f) $t = 21.24s$, (g) $t = 25s$. Right half: fuel and oxidizer mass fraction distributions. Left half: temperature contours and flow velocity vector distribution.

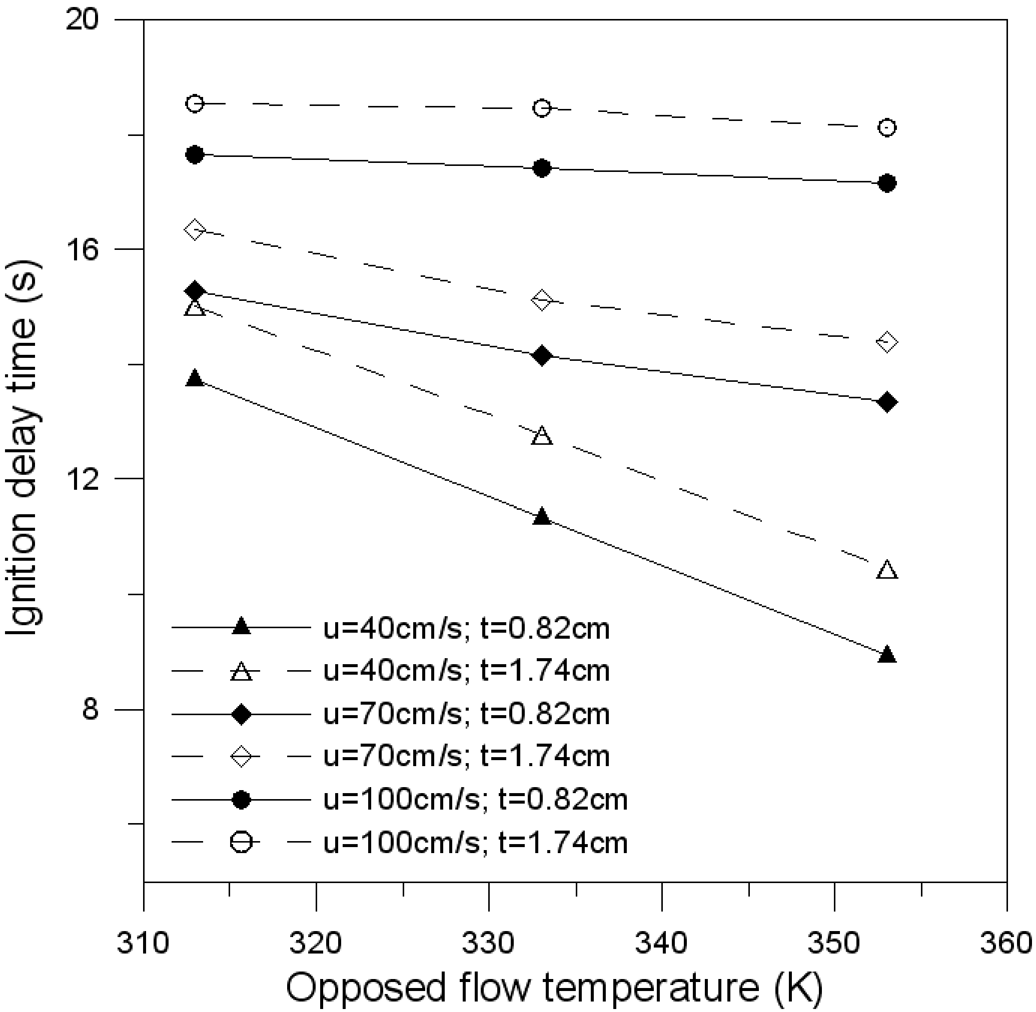

Figure 3.1.3 Ignition delay time versus the opposed flow temperature under different opposed flow velocity for solid fuel thicknesses are 0.82cm and 1.74cm, respectively.

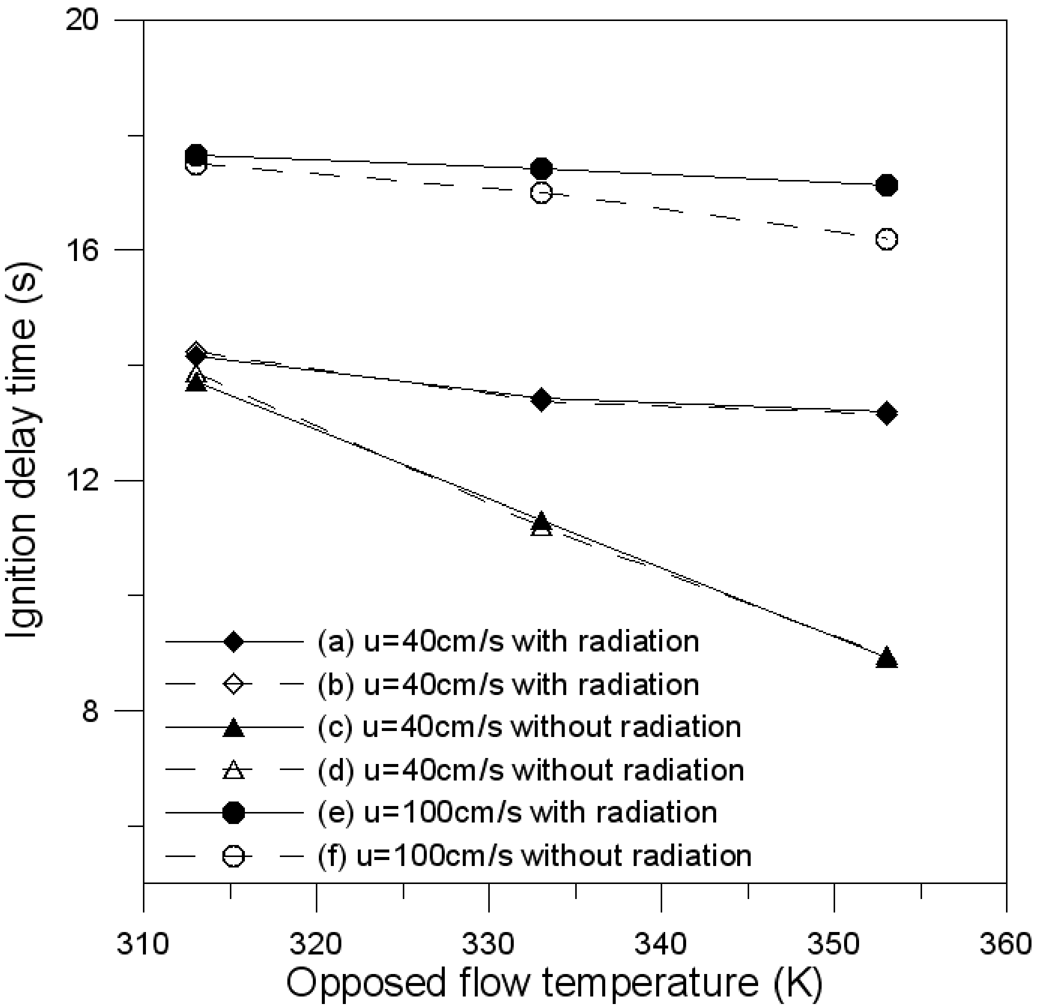

Figure 3.1.4 Ignition delay time versus the opposed flow temperature under different opposed flow velocity, the solid fuel lengths are (a) finite (b) infinite (c) finite (d) infinite (e) finite (f) finite, respectively.

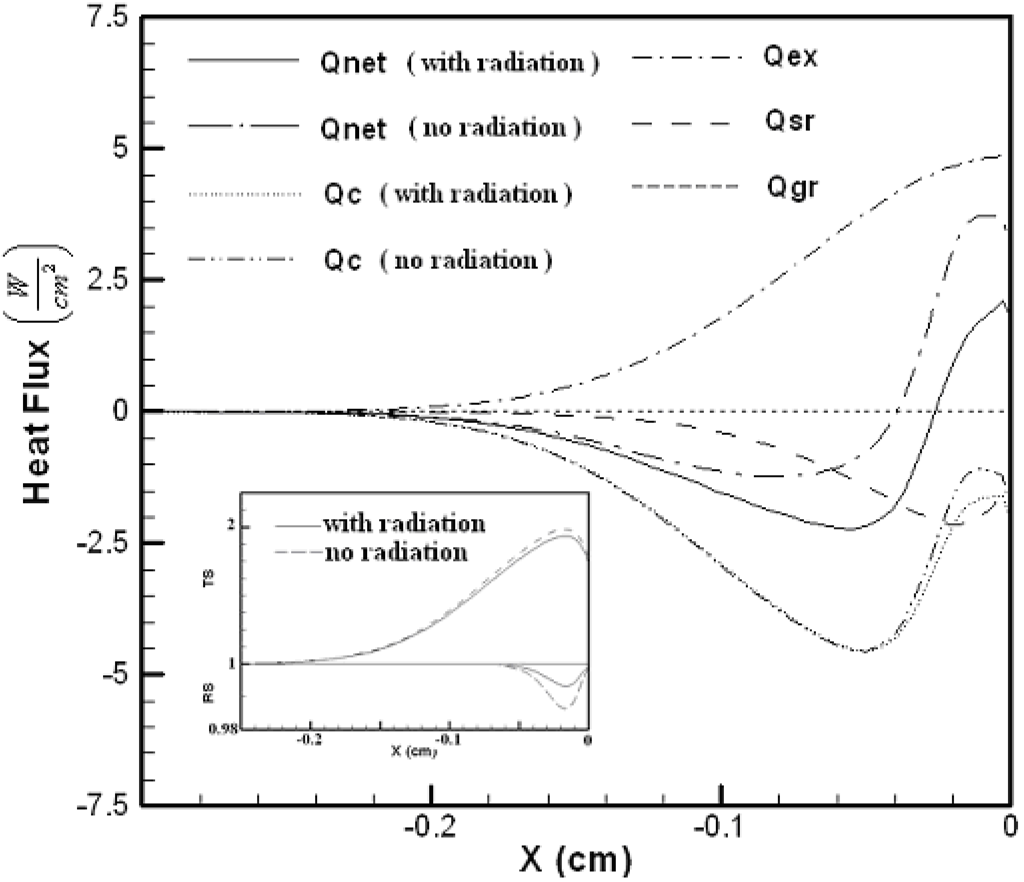

Figure 3.1.5 The distribution of heat fluxes along the solid fuel surface at $\bar{t} = 13.72s$, $\overline{u_\infty} = 40cm/s$, $\overline{T_i} = 313K$ and $\bar{\tau} = 0.82cm$ with and without radiation effects. The inset plots the distributions of the non-dimensional solid fuel temperature and the solid fuel density, respectively.

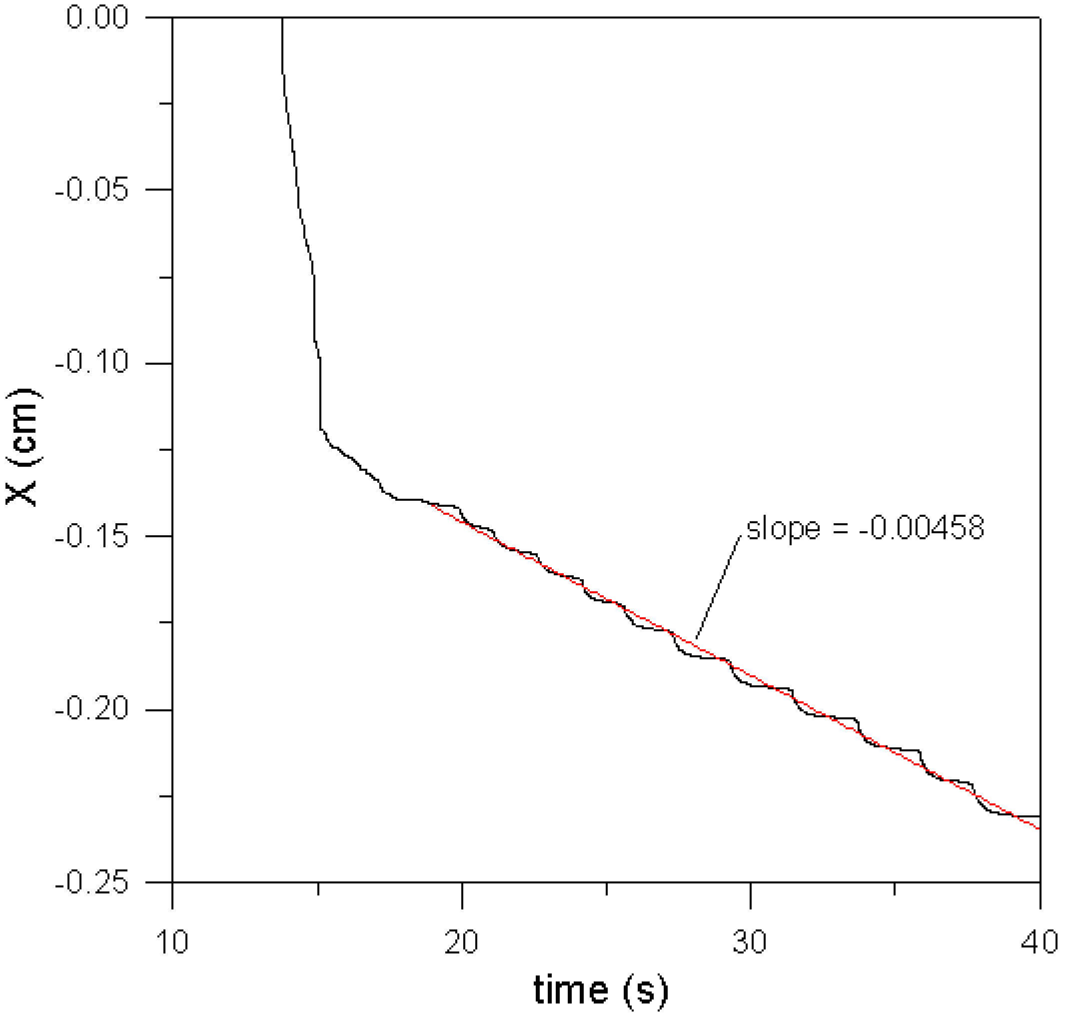

Figure 3.1.6 The pyrolysis front position varies with time at $\overline{u_\infty} = 70cm/s$, $\overline{T_i} = 333K$ and $\bar{\tau} = 0.82cm$.

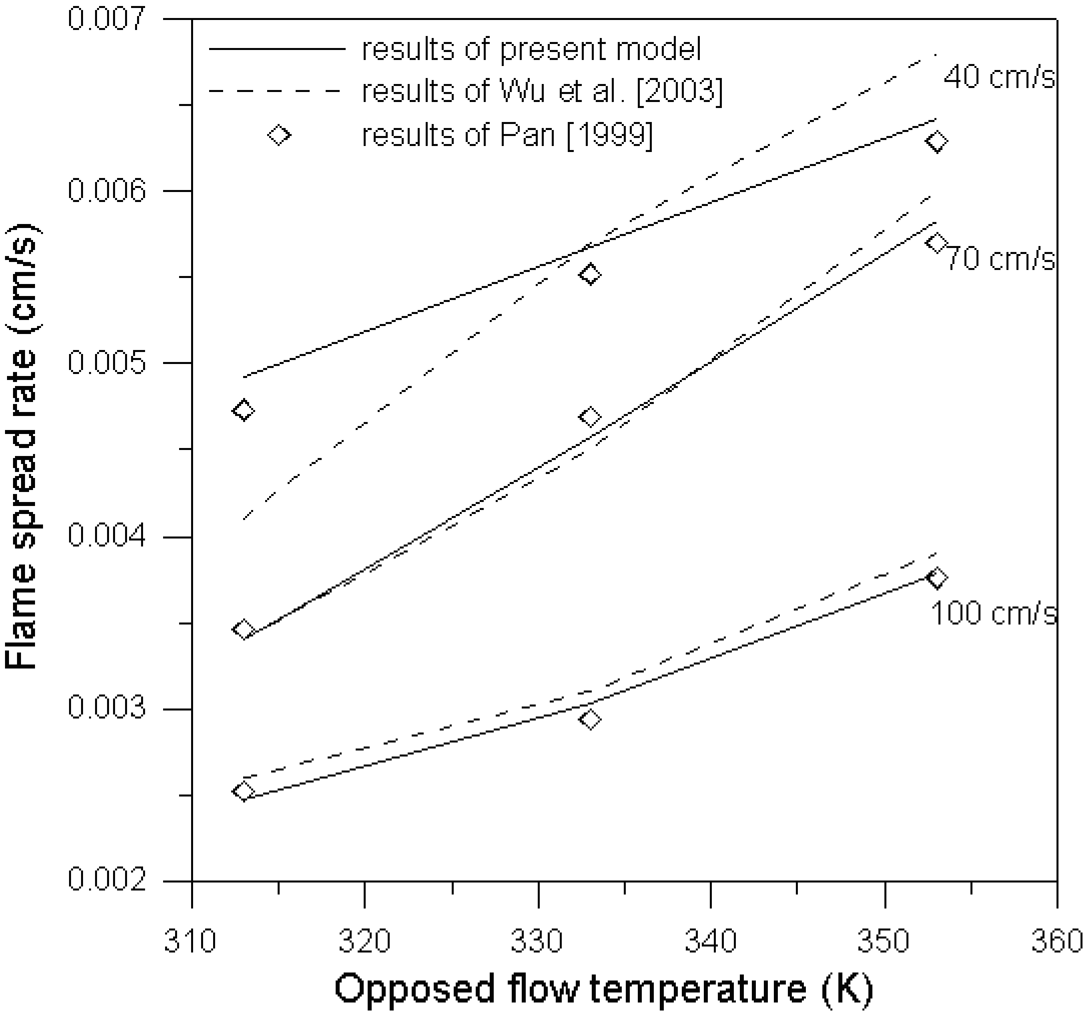

Figure 3.1.7 The flame spread rate versus the opposed flow temperature under different opposed flow velocities for the solid fuel thickness $\bar{\tau} = 0.82$ cm.

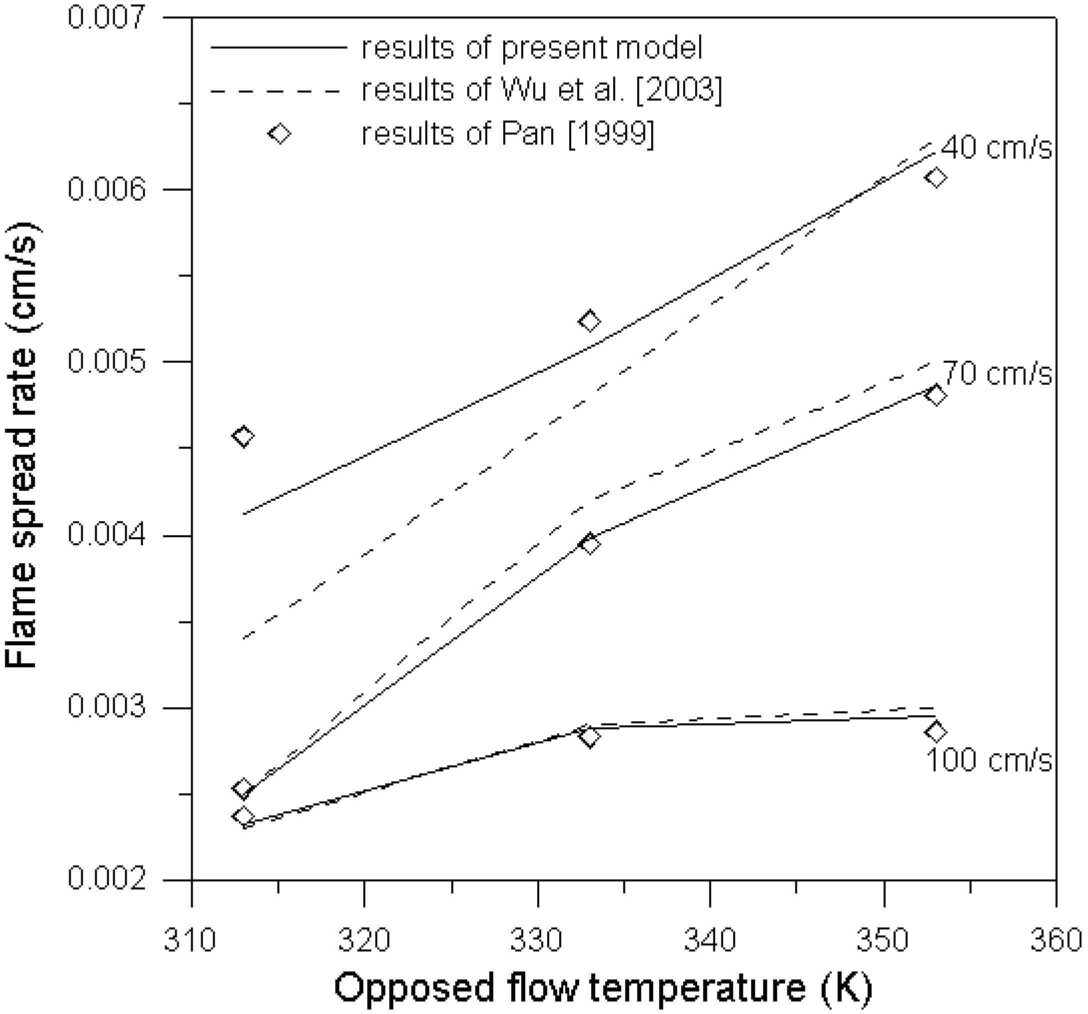

Figure 3.1.8 The flame spread rate versus the opposed flow temperature under different opposed flow velocities for the solid fuel thickness $\bar{\tau} = 1.74$ cm.

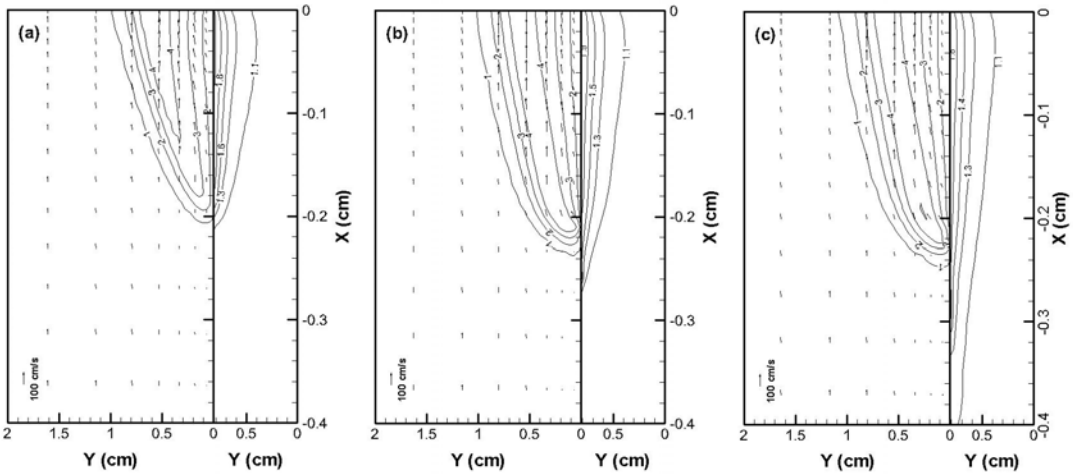

Figure 3.1.9 The temperature contours of gas and solid phases and vector distribution at $\bar{t} = 25s$, $\bar{u}_\infty = 40cm/s$ and $\bar{\tau} = 0.82cm$ for (a) $\bar{T}_i = 313K$, (b) $\bar{T}_i = 333K$ and (c) $\bar{T}_i = 353K$, respectively.

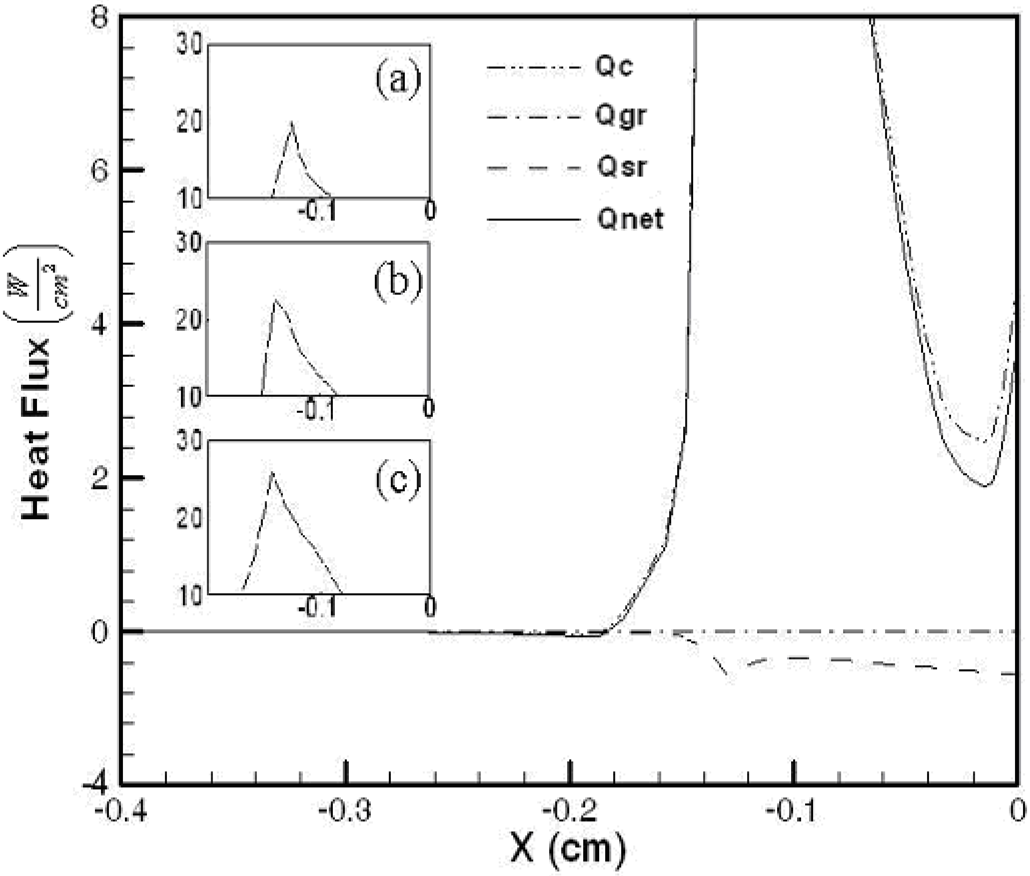

Figure 3.1.10 The distribution of heat fluxes along the solid fuel at $\bar{t} = 25s$, $\overline{u_\infty} = 40$ cm/s and $\bar{\tau} = 0.82cm$. The insets show the peak value of q_{net} for (a) $\overline{T_i} = 313K$, (b) $\overline{T_i} = 333K$ and (c) $\overline{T_i} = 353K$, separately.

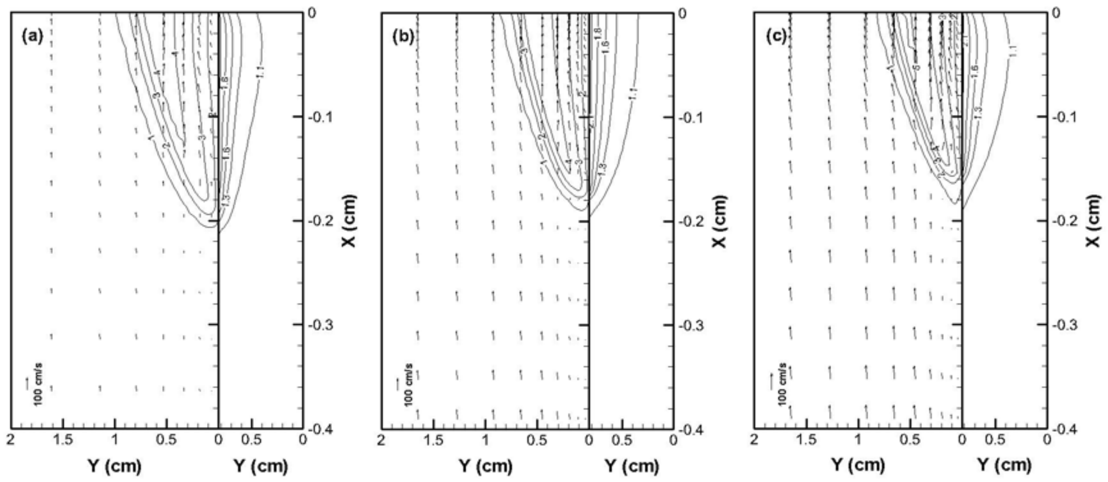

Figure 3.1.11 The temperature contours of gas and solid phases and vector distribution at $\bar{t} = 25s$, $\bar{T}_i = 313K$ and $\bar{\tau} = 0.82cm$ for (a) $\bar{u}_\infty = 40cm/s$, (b) $\bar{u}_\infty = 70cm/s$ and (c) $\bar{u}_\infty = 100cm/s$, respectively.

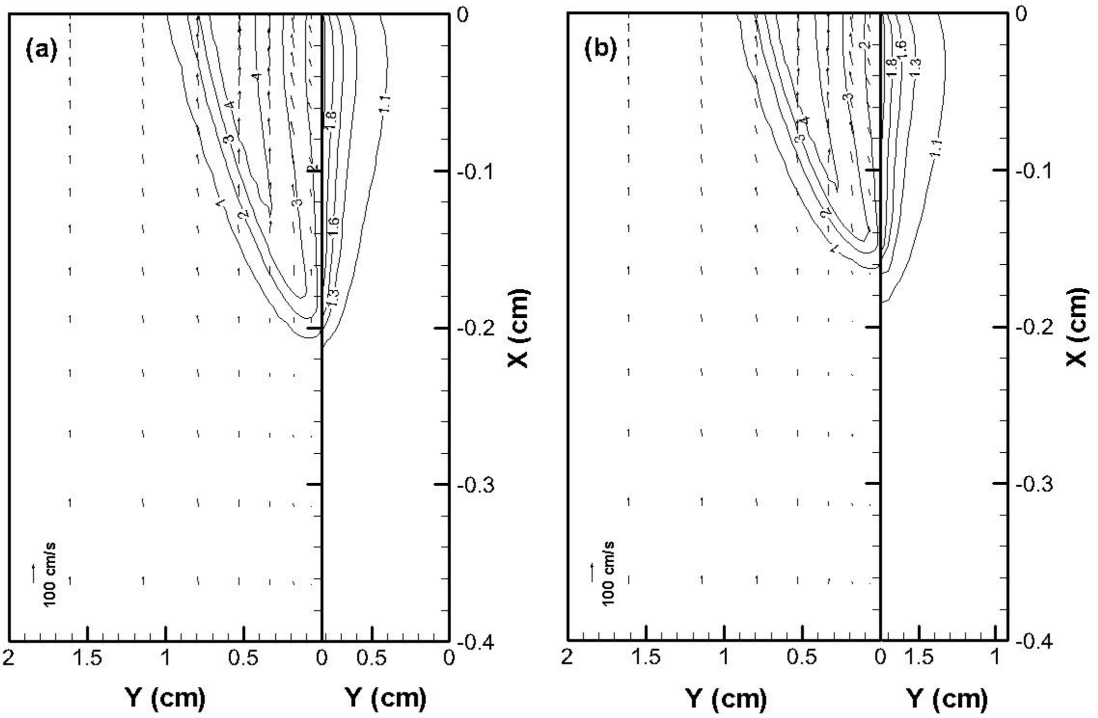

Figure 3.1.12 The temperature contours of gas and solid phases and vector distribution at $\bar{t} = 25s$, $\bar{u}_{\infty} = 40cm/s$, $\bar{T}_i = 313K$ and solid fuel thicknesses (a) $\bar{\tau} = 0.82cm$ (b) $\bar{\tau} = 1.74cm$, respectively.

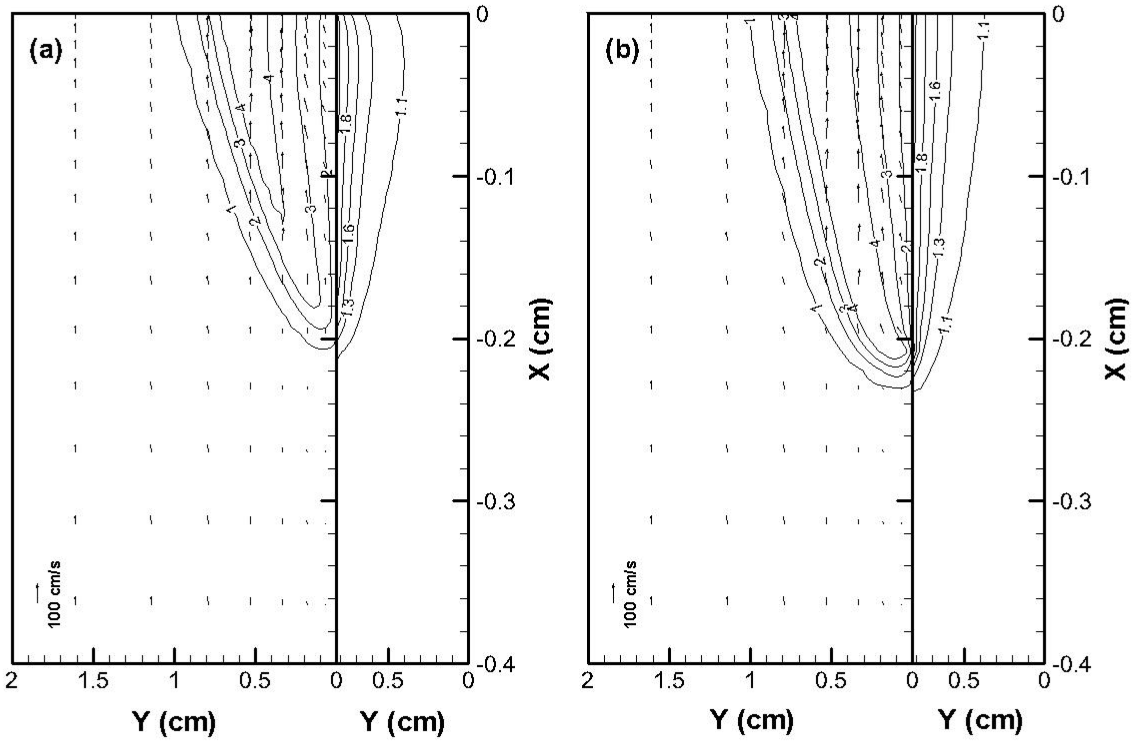

Figure 3.1.13 The temperature contours of gas and solid phases and vector distribution for (a) with radiation (b) without radiation, at $\bar{t} = 25s$, $\bar{u}_\infty = 40cm/s$, $\bar{T}_i = 313K$ and $\bar{\tau} = 0.82cm$.

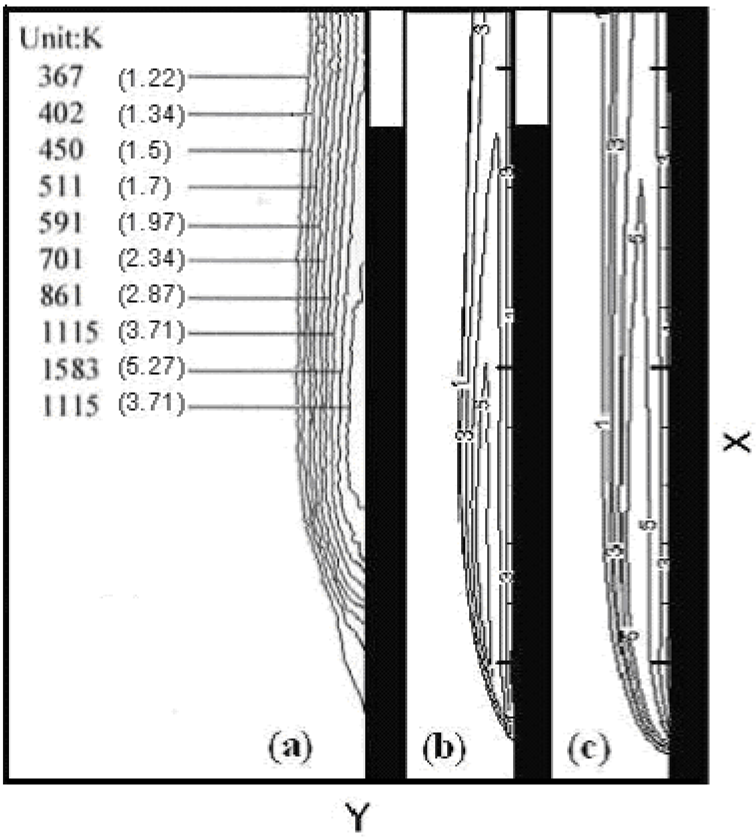

Figure 3.1.14 The gas phase temperature contour distributions over the solid fuel surface for (a) Pan's experiment (b) present work and (c) Wu's model, at $\bar{t} = 25s$, $\bar{u}_\infty = 40cm/s$, $\bar{T}_i = 313K$ and $\bar{\tau} = 0.82cm$. The figure 13(a) displays the flame temperature in Kelvin temperature scale and the non-dimensional temperature simultaneously.

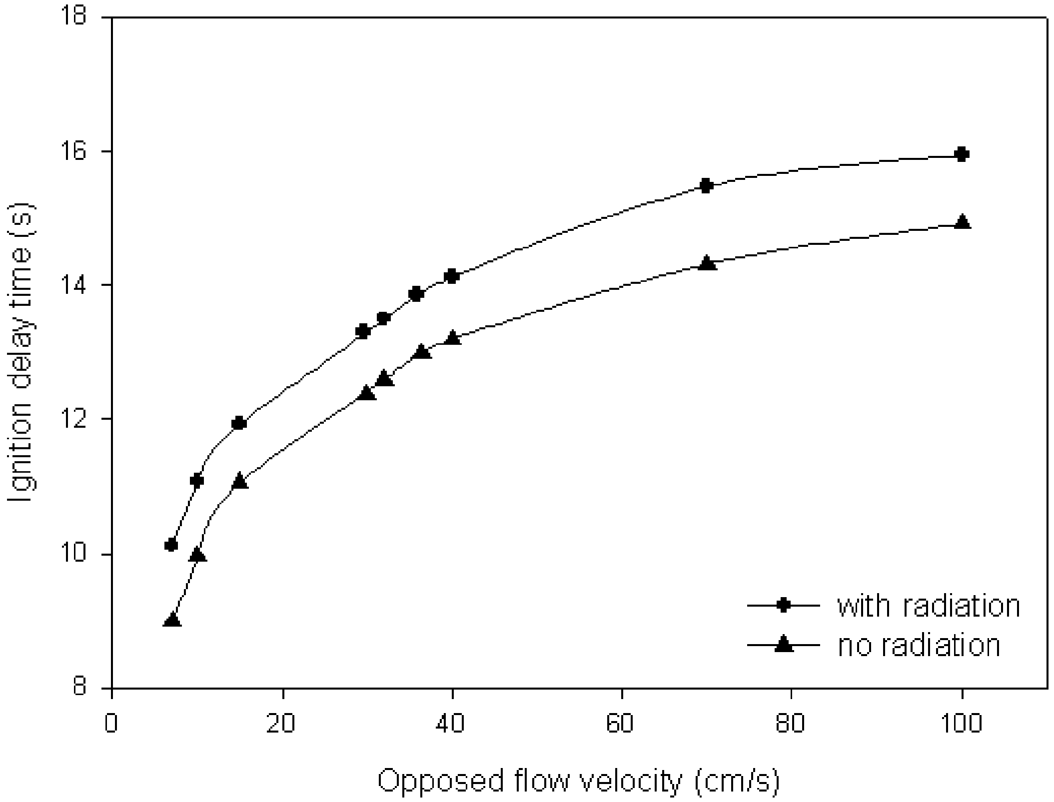

Figure 3.2.1 Ignition delay times as functions of opposed flow velocity at a fixed opposed flow temperature of 313K with and without radiation.

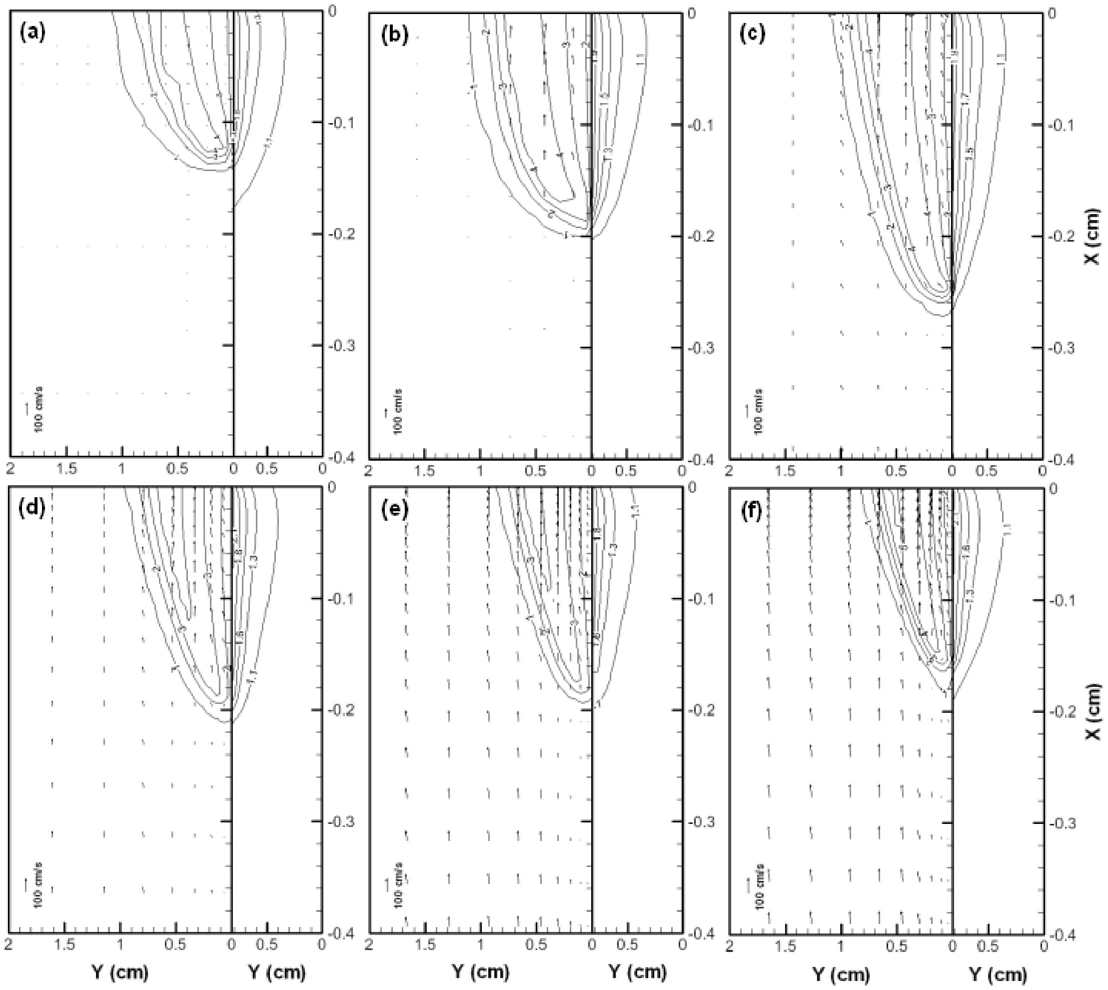

Figure 3.2.2 Flow velocity vector distributions and non-dimensional temperature contours for gas and solid phases at various opposed flow velocities, (a)7cm/s, (b)15cm/s, (c)32cm/s, (d)40cm/s, (e)70cm/s and (f)100cm/s, at a fixed opposed flow temperature of 313K. The centerline of wind tunnel is at 5cm along the Y axis of left hand side (not display in the figure).

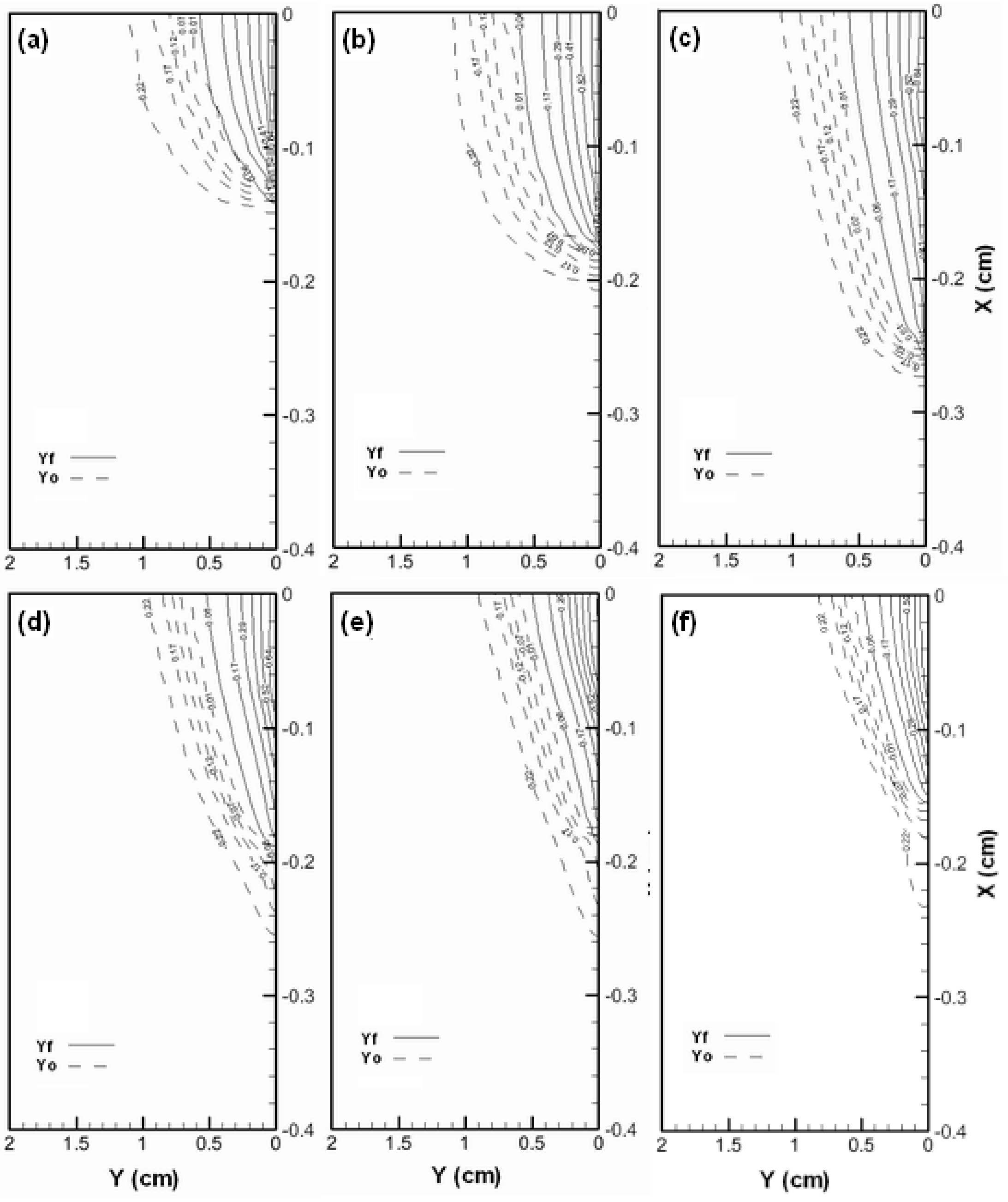

Figure 3.2.3 Fuel and oxidizer mass fraction distributions at various opposed flow velocities, (a)7cm/s, (b)15cm/s, (c)32cm/s, (d)40cm/s, (e)70cm/s and (f)100cm/s, at a fixed opposed flow temperature of 313K.

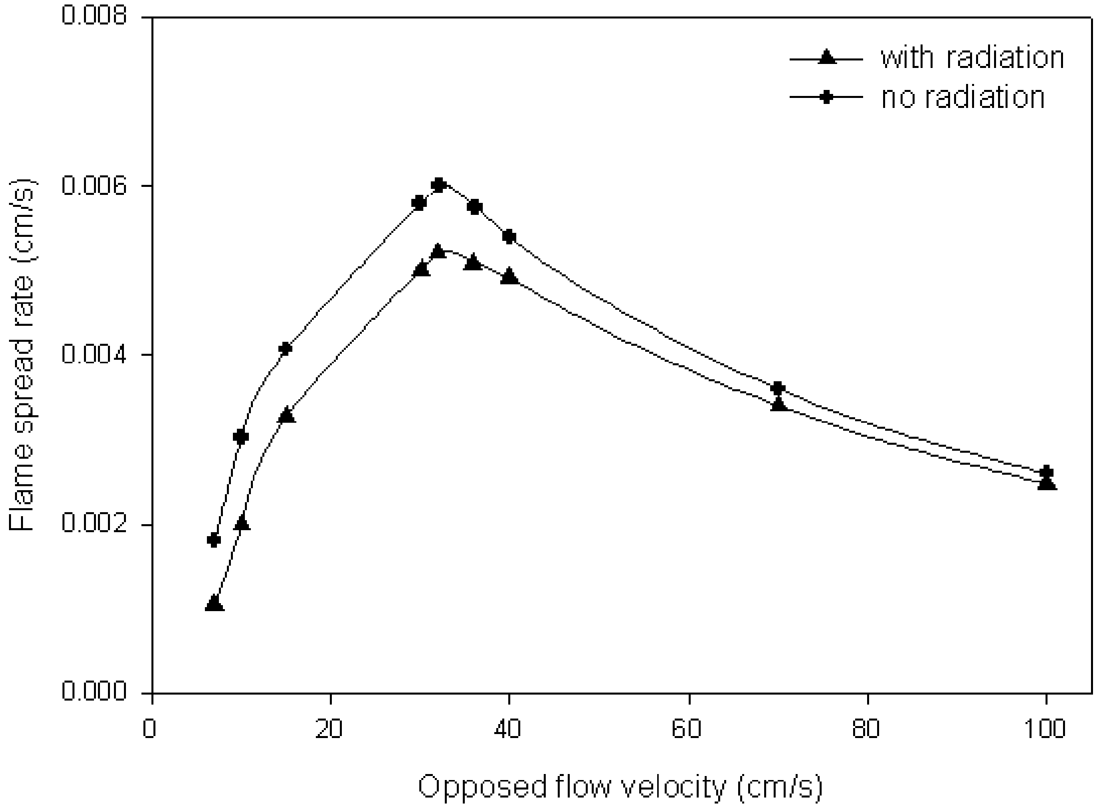

Figure 3.2.4 Flame spread rates versus opposed flow velocity at a fixed opposed flow temperature of 313K with and without radiation.

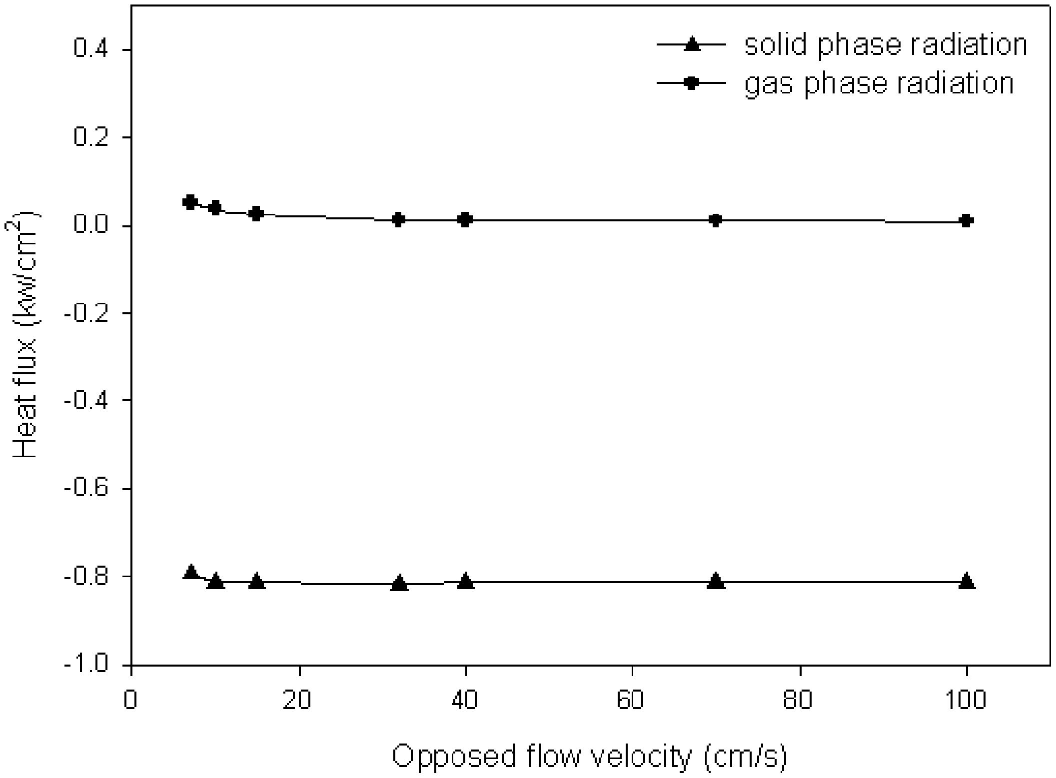

Figure 3.2.5 Heat flux magnitudes q_{gr} and q_{sr} at various opposed flow velocities at a fixed opposed flow temperature of 313K. q_{gr} and q_{sr}, represent the gas phase radiation feedback to solid fuel and the radiation heat loss from the solid fuel to the ambient.

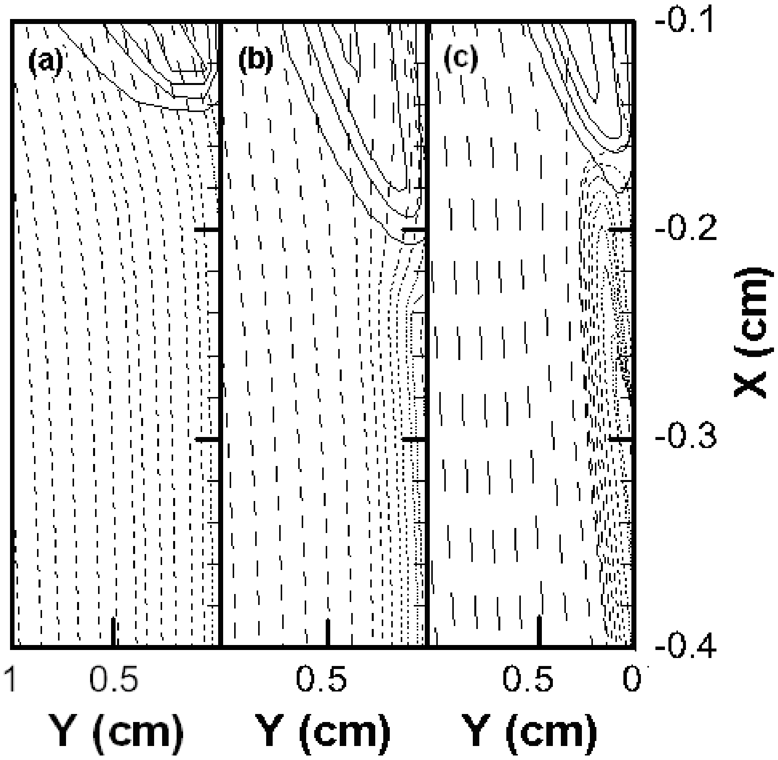

Figure 3.2.6 Temperature contour of gas phase and streamline distribution at a fixed opposed flow temperature of 313K and opposed flow velocities of 7cm/s, 32 cm/s and 100cm/s.

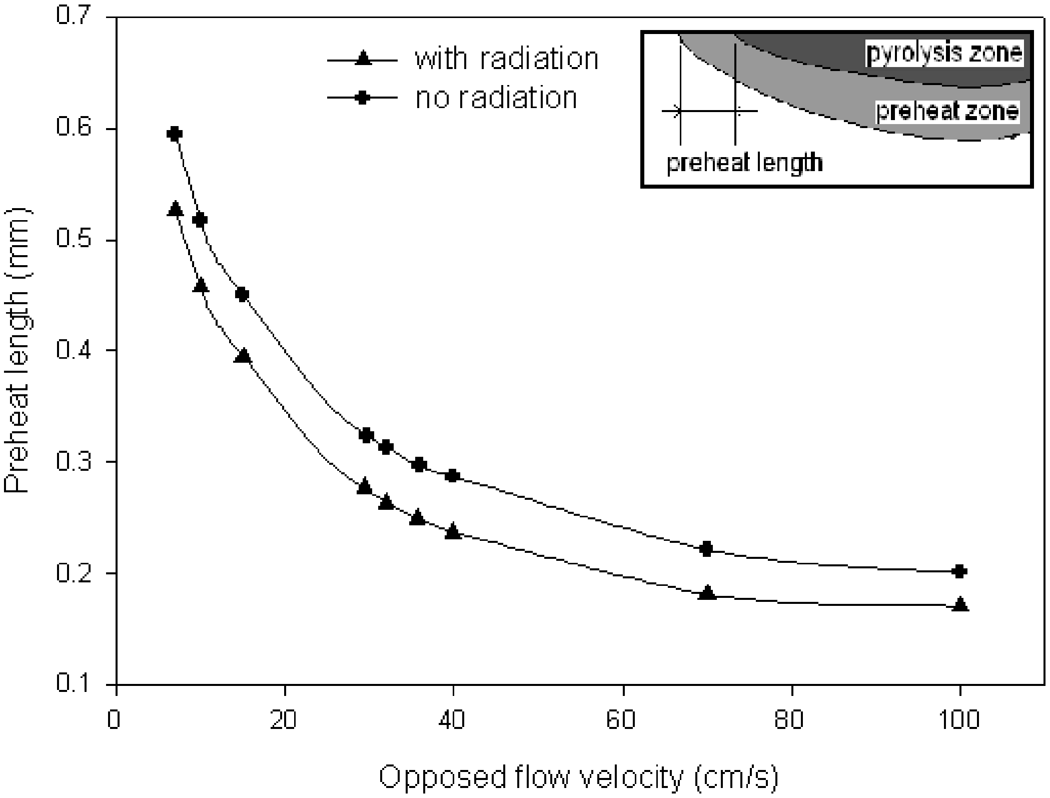

Figure 3.2.7 Preheat lengths versus opposed flow velocity at a fixed opposed flow temperature of 313K with and without radiations.

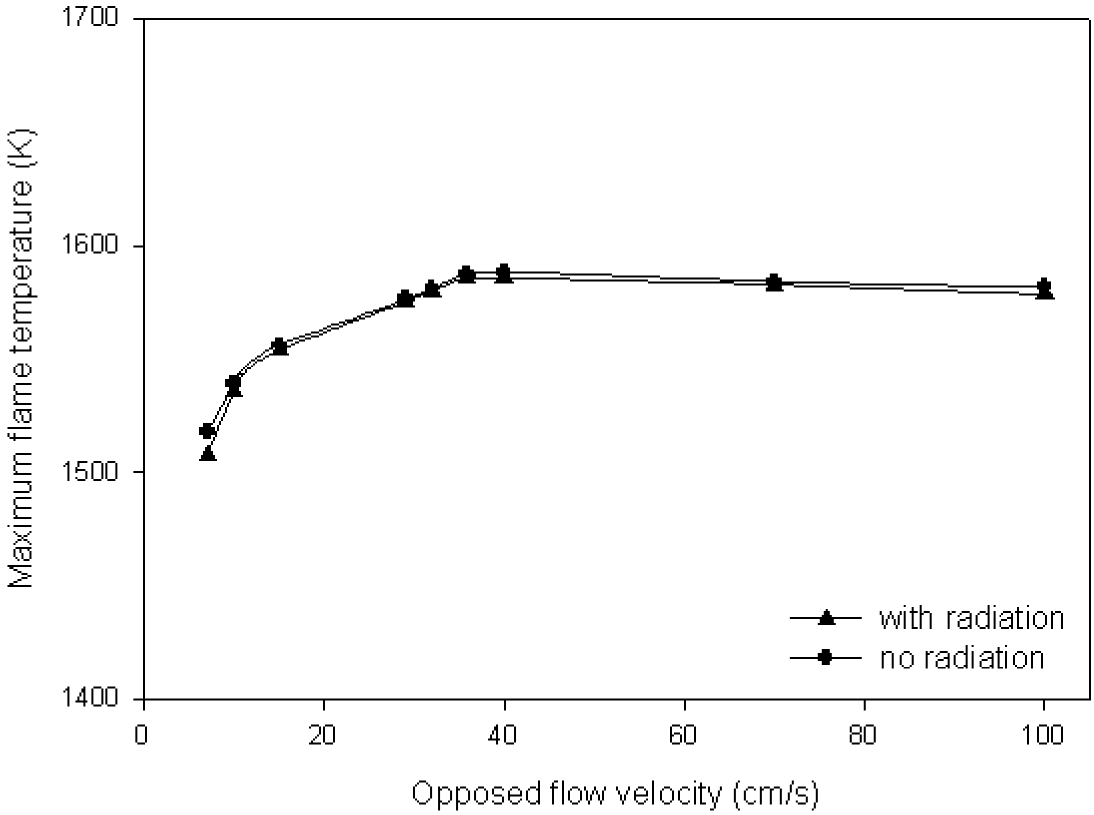

Figure 3.2.8 Maximum flame temperatures versus opposed flow velocity at a fixed opposed flow temperature of 313K with and without radiation.

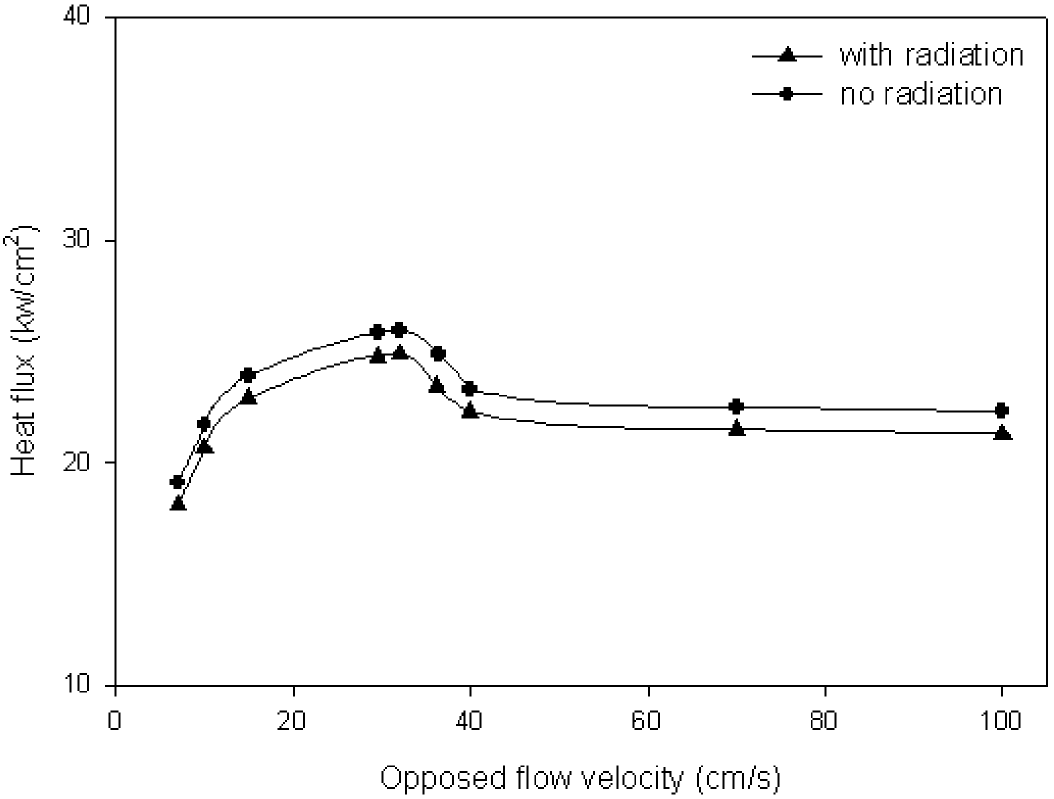

Figure 3.2.9 Total heat fluxes gained by solid fuel versus opposed flow velocity at a fixed opposed flow temperature of 313K with and without radiations, respectively.

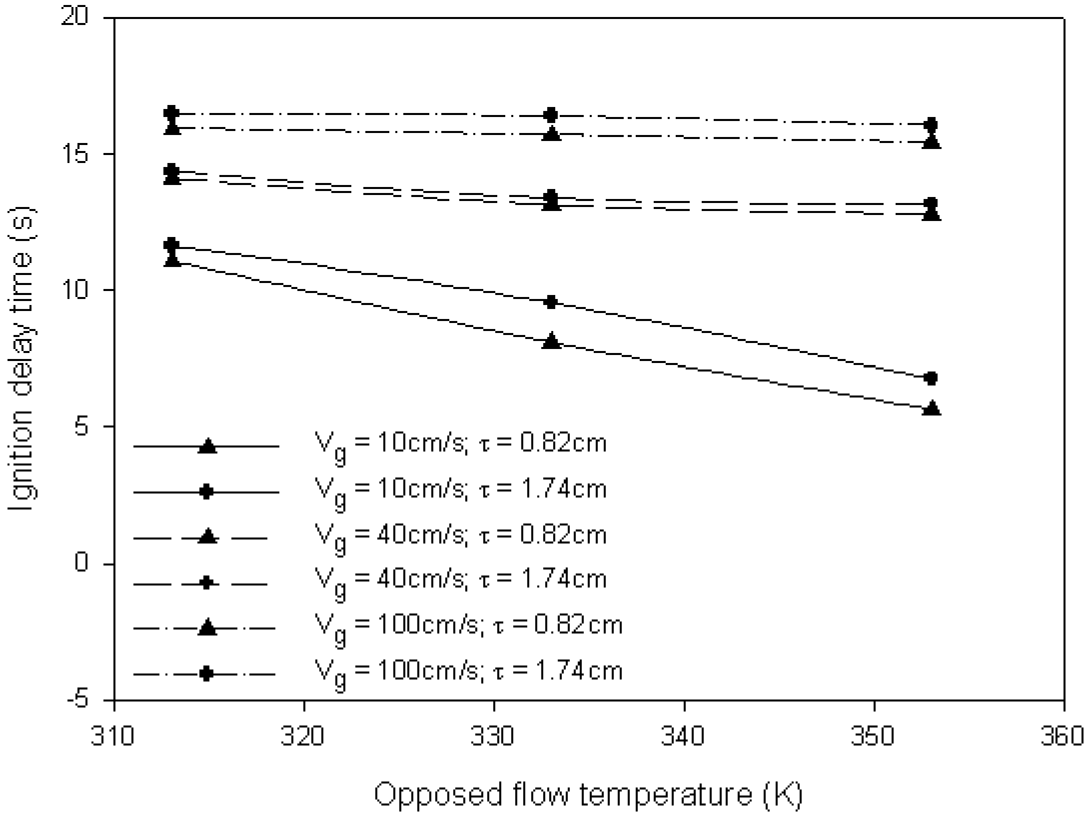

Figure 3.2.10 Ignition delay times versus opposed flow temperature under different opposed flow velocity for solid fuel thicknesses of 0.82cm and 1.74cm.

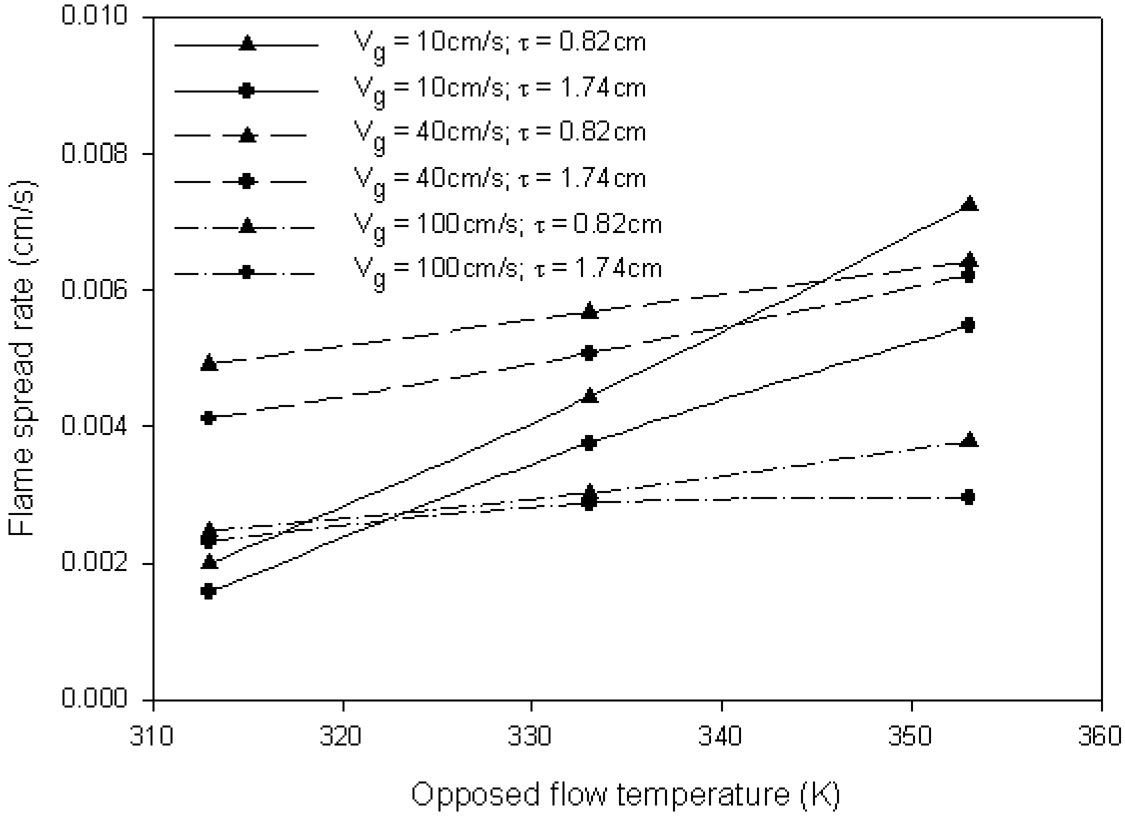

Figure 3.2.11 Flame spread rate versus opposed flow temperature under different opposed flow velocity for solid fuel thicknesses of 0.82cm and 1.74cm.

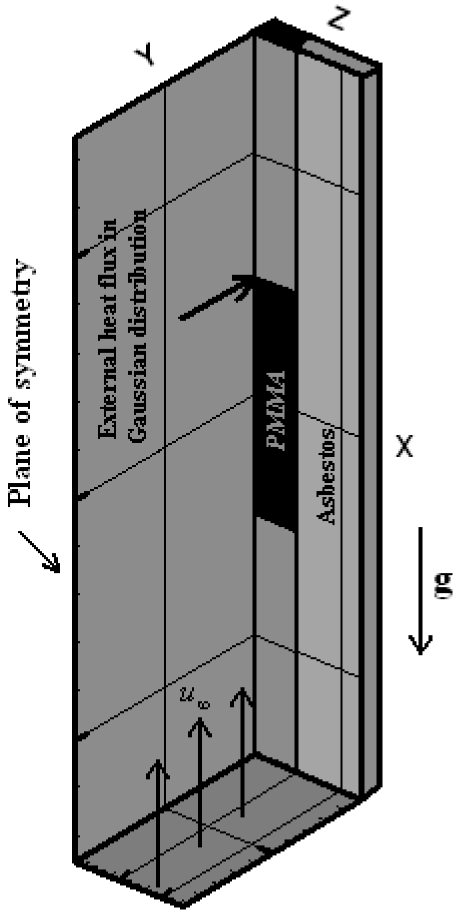

Figure 3.3.1 The schematic of downward flame spread over a finite-length PMMA slab in the mixed air flow in a wind tunnel.

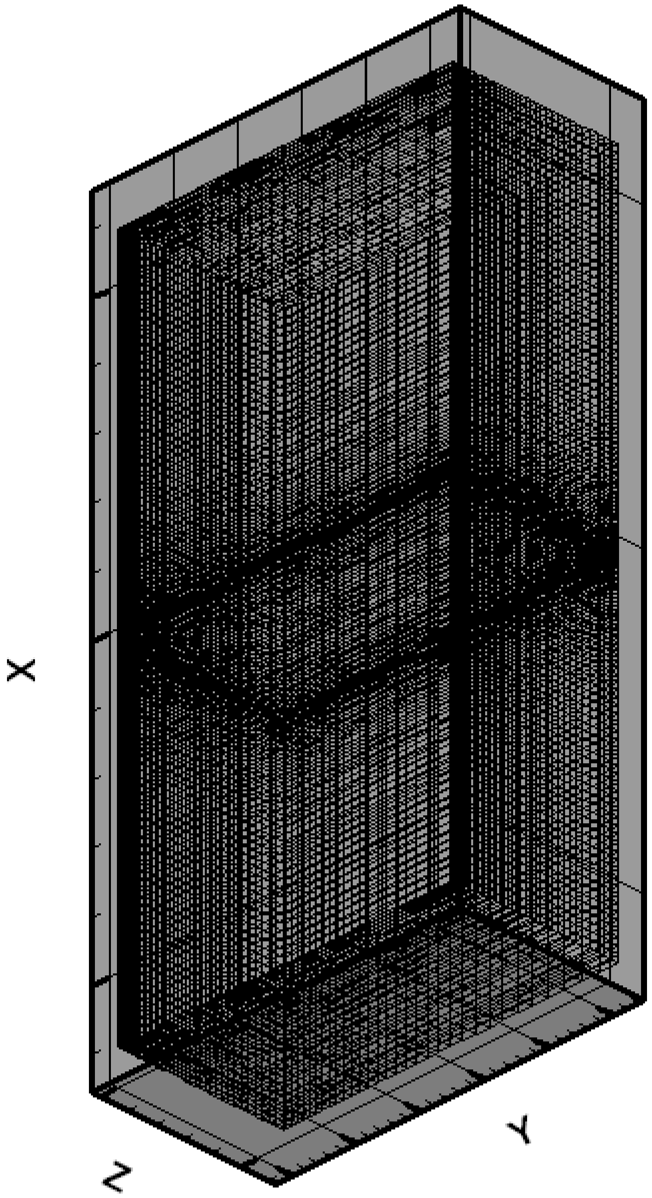

Figure 3.3.2 The non-uniform mesh distribution.

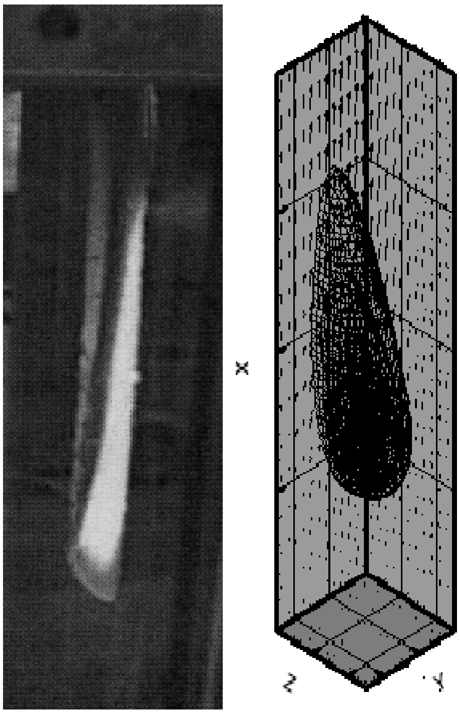

Figure 3.3.3 The flame profiles at $\bar{t} = 30s$, $\bar{u}_{\infty} = 40cm/s$, $\bar{T}_i = 313K$ and $\bar{\tau} = 0.82cm$. Right half: the simulated result of present work. Left half: the camera image obtained by Pan’s experiment.

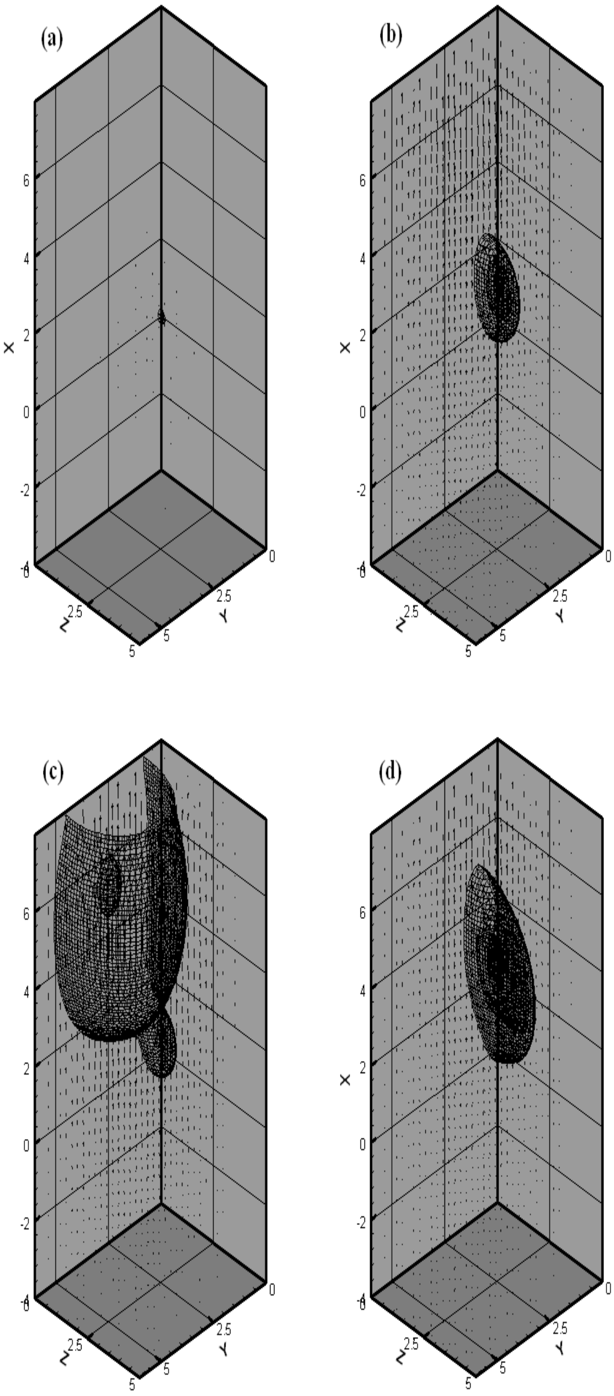

Figure 3.3.4 The three-dimensional flame profiles and flow velocity vectors for $\overline{u_{\infty}} = 40cm/s$, $\overline{T_i} = 313K$ and $\bar{\tau} = 0.82cm$ at (a) $t = 1s$ (b) $t = 14.76s$ (c) $t = 14.78s$ and (d) $t = 25s$.

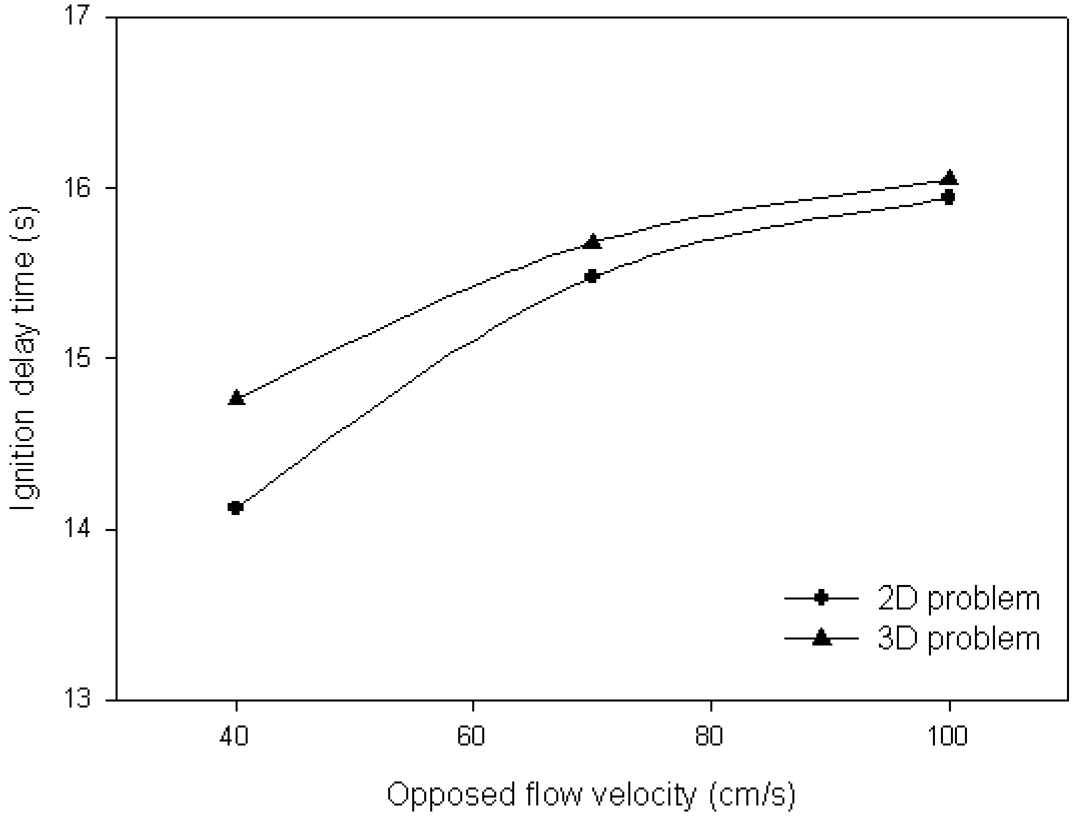

Figure 3.3.5 Ignition delay times as functions of opposed flow velocity at a fixed opposed flow temperature of 313K and solid fuel thickness of 0.82cm for 2D and 3D problems, separately.

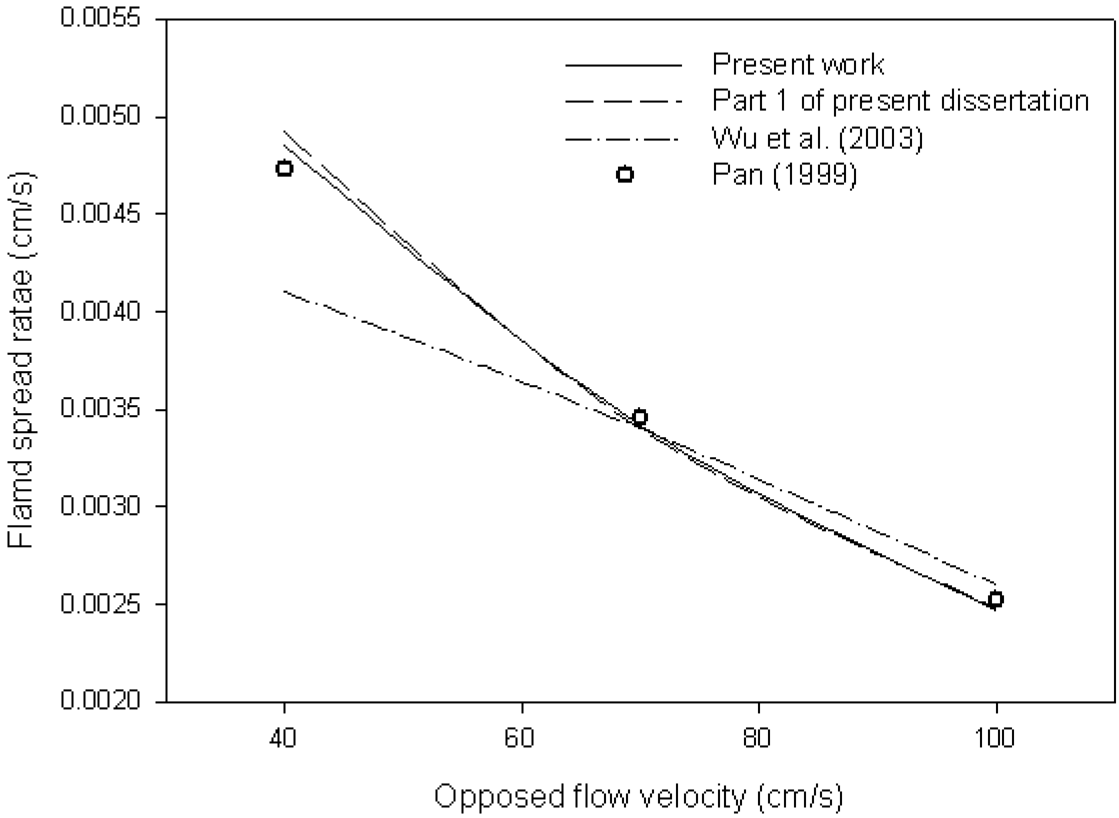

Figure 3.3.6 The flame spread rate versus the opposed flow temperature under different opposed flow velocities, 40 cm/s, 70 cm/s and 100 cm/s for opposed flow temperature of 3131K and the solid fuel thickness of 0.82 cm. Notably, there are three computed results in each solid and dash line.

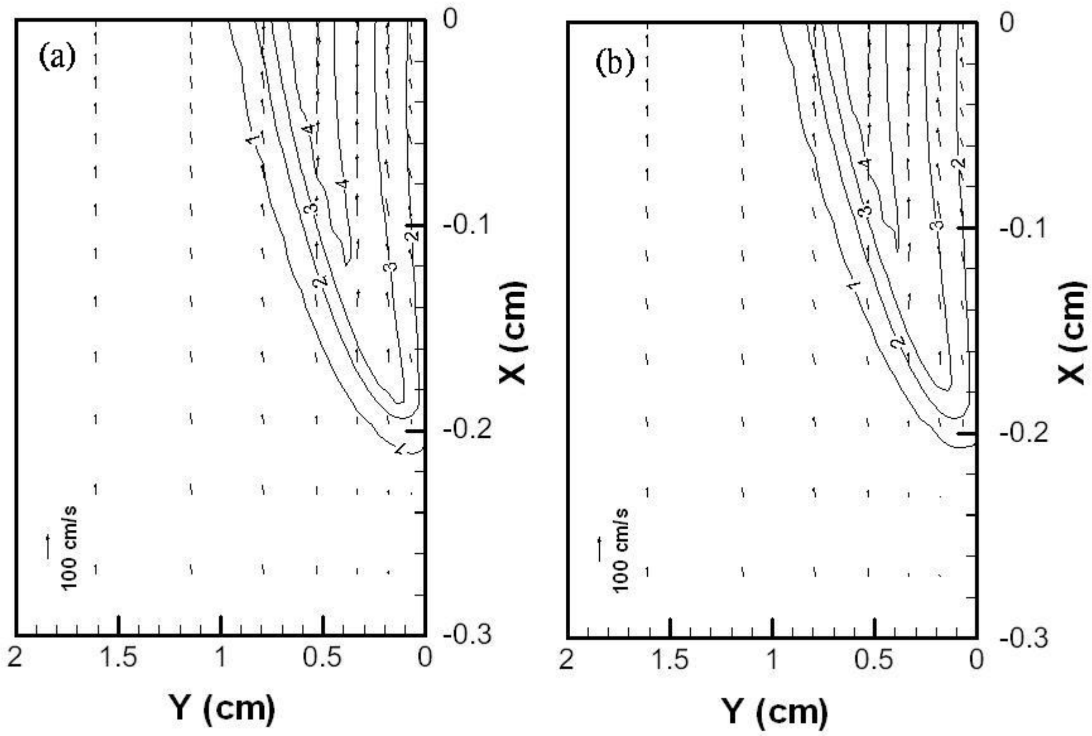

Figure 3.3.7 Flow velocity vector distributions and non-dimensional temperature contours of gas phase for (a) 2D problem and (b) 3D problem, respectively, at a fixed opposed flow velocity of 40cm/s and temperature of 313K and solid fuel thickness of 0.82cm.

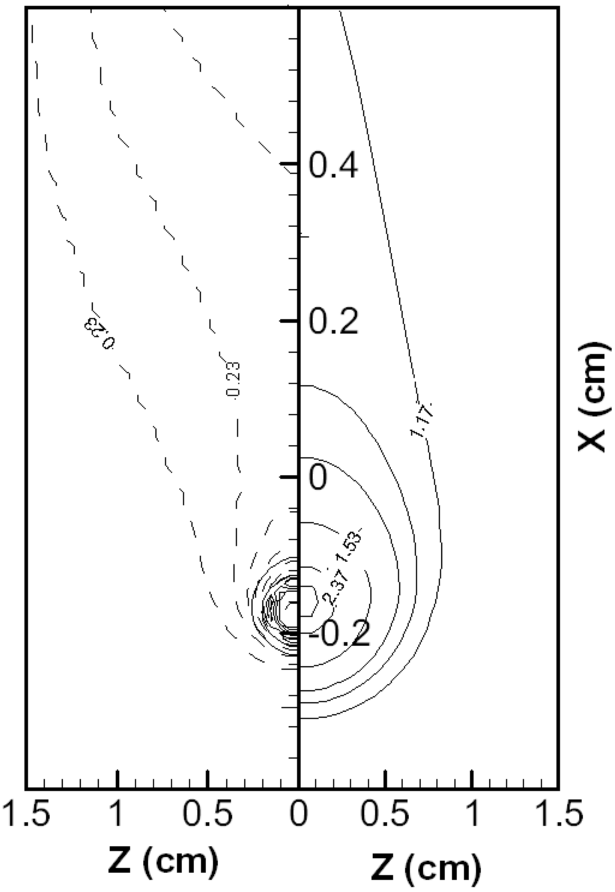

Figure 3.3.8 The flame characteristics on X-Z plane for opposed flow velocity of 40cm/s and temperature of 313K and solid fuel thickness of 0.82cm at t = 25s. The right half displays the gas phase temperature contours and flow velocity vectors; the left half presents the fuel and oxidizer mass fractions, respectively.

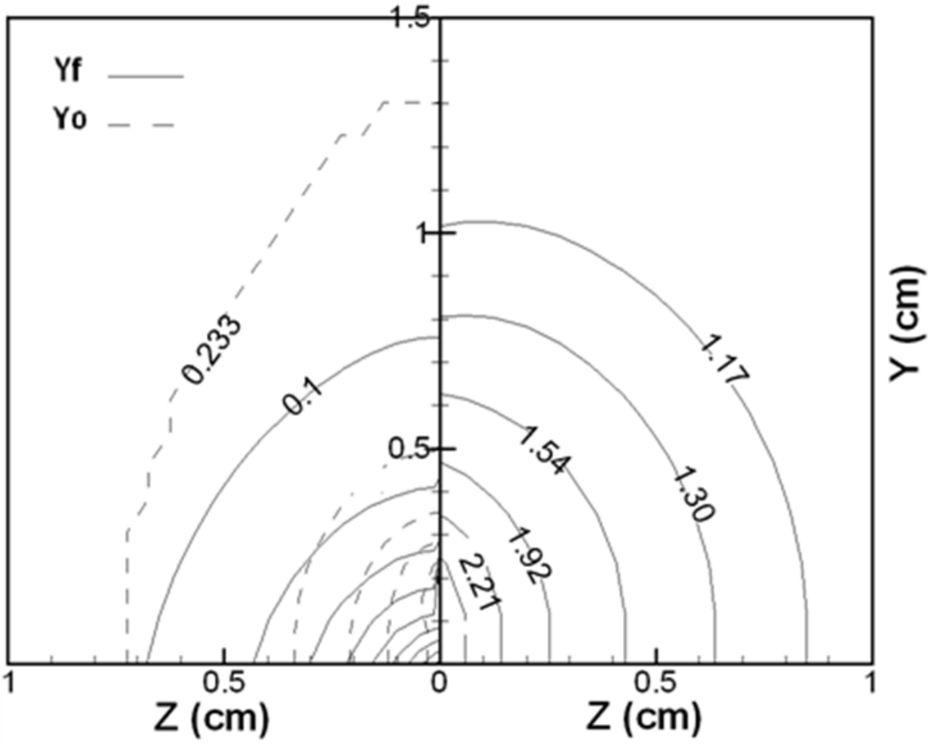

Figure 3.3.9 The flame characteristics on Y-Z plane for opposed flow velocity of 40cm/s and temperature of 313K and solid fuel thickness of 0.82cm at t = 25s. The right half displays the gas phase temperature contours and flow velocity vectors; the left half presents the fuel and oxidizer mass fractions, respectively.

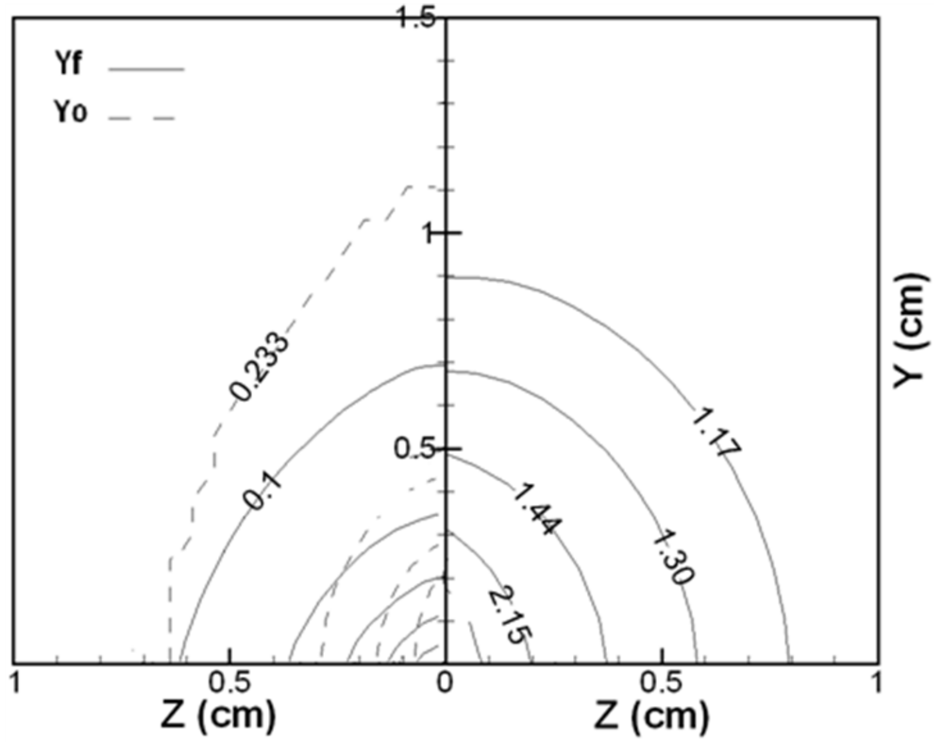

Figure 3.3.10 The flame characteristics on Y-Z plane for opposed flow velocity of 100cm/s and temperature of 313K and solid fuel thickness of 0.82cm at t = 25s. The right half displays the gas phase temperature contours and flow velocity vectors; the left half presents the fuel and oxidizer mass fractions, respectively.

Publications

1. Chang, W. K., Chen, C. H. and Liou, T. M., Experimental and Numerical Studies for Flame Spread Over A Finite-length PMMA With Radiation Effect, *16th International Symposium on Transport Phenomena*, Prague, 2005.
2. Chang, W. K., Chen, C. H. and Liou, T. M., Numerical Studies for Downward Flame Spread Over A Finite-length PMMA With Radiation Effect, accepted by *International Journal on Transport Phenomena*, in press, 2007.
3. Chang, W. K., Hsieh, Y. J., Chen, C. H. and Lin, P. H., The Numerical Simulation for Flow and Pressure Distributions of Trains Movement in Tunnels, accepted by *CSME*, in press, 2007.
4. Chang, W. K. and Chen, C. H., Effect of Opposed Flow on Flame Spread Over A Finite-length PMMA Slab in A Two-dimensional Wind Tunnel, accepted by *Combustion Science and Technology*, in press, 2007.